The Mechanical Performance of the Fusion Reactor First Wall

Part II

Behaviour under pulsed load conditions

W. Daenner, J. Raeder

IPP 4/149 March 1977

MAX-PLANCK-INSTITUT FÜR PLASMAPHYSIK

8046 GARCHING BEI MÜNCHEN

MAX-PLANCK-INSTITUT FÜR PLASMAPHYSIK

GARCHING BEI MÜNCHEN

The Mechanical Performance of the Fusion Reactor First Wall

Part II

Behaviour under pulsed load conditions

W. Daenner, J. Raeder

IPP 4/149 March 1977

Die nachstehende Arbeit wurde im Rahmen des Vertrages zwischen dem Max-Planck-Institut für Plasmaphysik und der Europäischen Atomgemeinschaft über die Zusammenarbeit auf dem Gebiete der Plasmaphysik durchgeführt.

Abstract

While the first part of this report was concerned with the steady-state mechanical analysis of the fusion reactor first wall, this part deals with the analysis based upon pulsed load conditions. In a first section we elaborate various solutions of the non-stationary heat conduction problem in plane geometry capable of describing the temperature response of the wall due to characteristic plasma pulse sequences. These solutions are input to a quasi-steady-state stress and strain analysis. Finally, the results of this analysis are set in relation to the fatique properties of the wall material.

A further section presents a description of a computer program which uses the mathematical procedure described. The results of some test runs are followed by those of detailed parameter studies. In the course of these calculations the influences of a number of design and operational quantities of a fusion reactor were investigated. It turned out that the choice of wall thickness and wall loading are of predominant importance for the first wall fatigue life.

Table of contents

1. Introduction

The first part of this report /1/ was concerned with the thermal and mechanical analysis of the fusion reactor first wall under steady-state load conditions. For a number of different basic geometries - plane, cylindrical, and spherical - the mathematical means of calculating the temperature and stress profiles across the wall had been provided. Besides pressure loads, the thermal stresses caused by internal nuclear heating and by heat conduction and radiation from the plasma have also been taken into account.

The thorough investigations on the plasma behaviour performed during the last years have confirmed the view that tokamak reactors can no longer be conceived as quasi-steady-state devices. Since the accumulation of α-particles and impurity atoms causes with a high degree of probability a strong limitation of the burn time /2/, the operational characteristics are likely to be those of a pulsed reactor. Therefore, the necessary consequence for the first wall analysis is to treat both nuclear heating and plasma radiation and heat conduction as time dependent.

This part of the report summarizes the fundamental considerations of this problem. It starts with the treatment of the non-stationary heat conduction problem in the wall resulting in a solution for the space and time dependent temperature variations. These results are input to the subsequent time dependent stress and strain analysis which yields the information necessary to estimate a lifetime based on the material's fatique behaviour. The entire mathematical procedure was again programmed for the computer, this program being, in fact, an extended version of that already described /1/. It has been tested and applied to a number of sample problems the results of which are presented in further sections of this report.

2. Theoretical basis

2.1. The basic differential equation

We start from the differential equation of non stationary heat conduction in an isotropic solid:

$$\operatorname{div}(\lambda \operatorname{grad} \vartheta) + q = \varrho c_p \frac{\partial \vartheta}{\partial t} \qquad (1)$$

(ϑ = temperature, $\lambda = \lambda(\vartheta)$ = thermal conductivity, $\varrho = \varrho(\vartheta)$ = mass density, $c_p = c_p(\vartheta)$ = specific heat per unit mass, $q = q(r,t)$ = power released per unit volume of the solid, r = position vector of the point considered, t = time coordinate).

To remove the nonlinearity in (1) caused by λ depending on ϑ, we introduce the heat flux potential

$$S(\vartheta) = \int_{\vartheta_B}^{\vartheta} \lambda(\vartheta') d\vartheta' \qquad (2)$$

(ϑ_B is an arbitrary reference temperature) into (1) and get

$$\operatorname{div} \operatorname{grad} S + q = \alpha(S) \frac{\partial S}{\partial t} \qquad (3)$$

or

$$\Delta S + q = \alpha(S) \frac{\partial S}{\partial t} \qquad (4)$$

($\alpha = \varrho c_p / \lambda$). The coefficient α is basically a function of ϑ because ϱ, c_p, and λ depend on ϑ but α can also be considered as being a function of S for (2) establishes a unique relationship between S and ϑ for a fixed ϑ_B.

2.1.1. Simplifying assumptions

Because we are treating the problem of the first wall of fusion reactors, the extent of the solid normal to the wall surface and the temperature variations across the wall thickness will be moderate. This allows two simplifications of the problem:

(a) instead of $\alpha(S)$ we shall use the constant value α_o,

(b) we shall restrict the analysis to one-dimensional plane geometry.

Assumption (a) is justified by, on the one hand, the weak dependence of α on S for the candidate materials (see Table I), such as, for example, stainless steel (see Fig. 1) and by, on the other hand, the moderate temperature variations over

Table I: Reciprocal thermal diffusivity / s/cm^2 / for various conticipated wall materials

Temp. /C/	1.4970 Stainl.Steel	Molybdenum	Niobium	Vanadium$^+$	Aluminium^{++}
0	26.70	1.833	4.384	10.320	1.007
100	26.87	1.926	4.240	9.852	1.053
200	26.04	2.046	4.167	9.470	1.096
300	24.89	2.156	4.052	8.969	1.139
400	23.90	2.261	3.959	8.606	1.181
500	23.16	2.386	3.871	8.203	-
600	22.76	2.502	3.798	7.918	-
700	22.36	2.614	3.697	7.610	-
800	-	2.727	3.627	7.289	-
900	-	2.841	3.554	-	-
1000	-	2.967	3.501	-	-

$^+$ Constant specific heat assumed

$^{++}$ Constant thermal conductivity assumed.

The data are taken from /7/ in the case of stainless steel, /8/ in the case of niobium and vanadium, and /9/ in the case of molybdenum and aluminium.

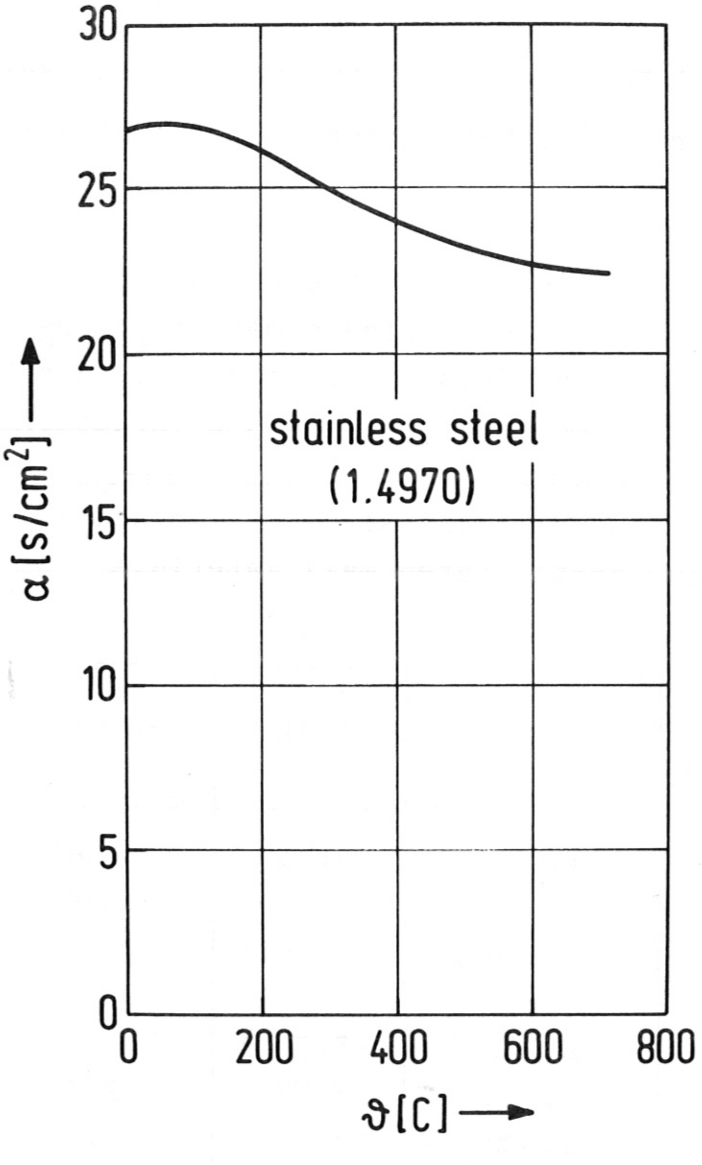

Fig. 1 The function α (= reciprocal diffusivity) vs. temperature ϑ for stainless steel

the wall thickness. The steady-state difference, for instance, between plasma and coolant side temperatures is about 100 K for a two centimetre thick stainless steel wall exposed to a neutron wall loading equivalent to 100 W/cm^2 /1/. At a mean temperature of 500 C this temperature difference corresponds to a variation of α of 2.5 %. The fact that a minor error is caused by neglecting this small variation of α is far outweighed by the fact that (4) becomes a linear partial differential equation if $\alpha = \alpha_o$ = const. This allows full use to be made of the mathematical methods developed to solve such equations analytically.

Assumption (b) is a good approximation as long as the principal radii of curvature of the wall surface are large compared to the wall thickness. The smallest values for these radii of curvature are to be expected for the case of the wall being made up by modules the surface of which protrudes to the plasma. To gain some insight into the errors involved, the steady-state temperature distribution according to /1/ were calculated for cylindrical and spherical surfaces with radii of curvature r_c. As a result Fig. 2 shows $\Delta\vartheta/(\Delta\vartheta)_{pl}$ vs. d/r_c for cylindrical and spherical geometry ($\Delta\vartheta = \vartheta(x=0) - \vartheta(x=d)$, $(\Delta\vartheta)_{pl} = \Delta\vartheta$ for plane geometry).

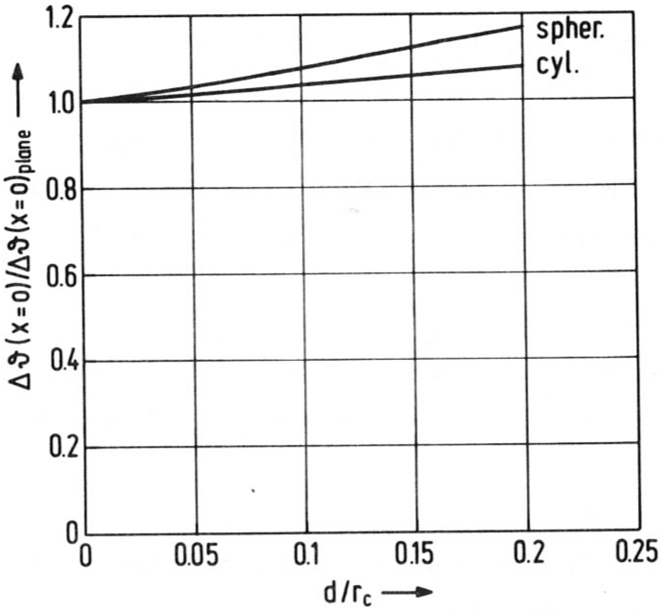

Fig. 2 Steady-state temperature differences over the wall thickness d for cylindrical and spherical geometry (radius r_c) compared with the case of plane geometry.

By using the assumptions (a) and (b) we get from (4)

$$\frac{\partial^2 s}{\partial x^2} + q(x,t) = \alpha_o \frac{\partial s}{\partial t} . \qquad (5)$$

Finally, we assume for q(x,t) the following form:

$$q(x,t) = q_x(x).q_t(t). \qquad (6)$$

This factorization is possible in our case because the nuclear heating rate in the solid is proportional to the number of incident neutrons per unit time, on the one hand, and is determined by the spatial distribution of the different blanket materials, on the other hand. Both influences are independent of each other, as long, as the flight time of the neutrons in the solid is small compared with the time scale of q(x,t). The dimension of $q_x.q_t$ is power per unit volume. The dimensions of q_x and q_t may differ from problem to problem because different choices are adequate to different cases.

2.1.2. Boundary and initial conditions

The plasma surrounded by the wall considered here releases energy to the wall in the form of fusion neutrons, radiation over a wide range of wavelengths, and heat and plasma particle fluxes.

The volume heating by neutrons and absorbed radiation is accounted for by the source term q(x,t) in (5).

The fluxes of heat and plasma particles give rise to a time dependent heat flux density $Q_w(t)$ at the wall surface facing the plasma (see Fig. 3).

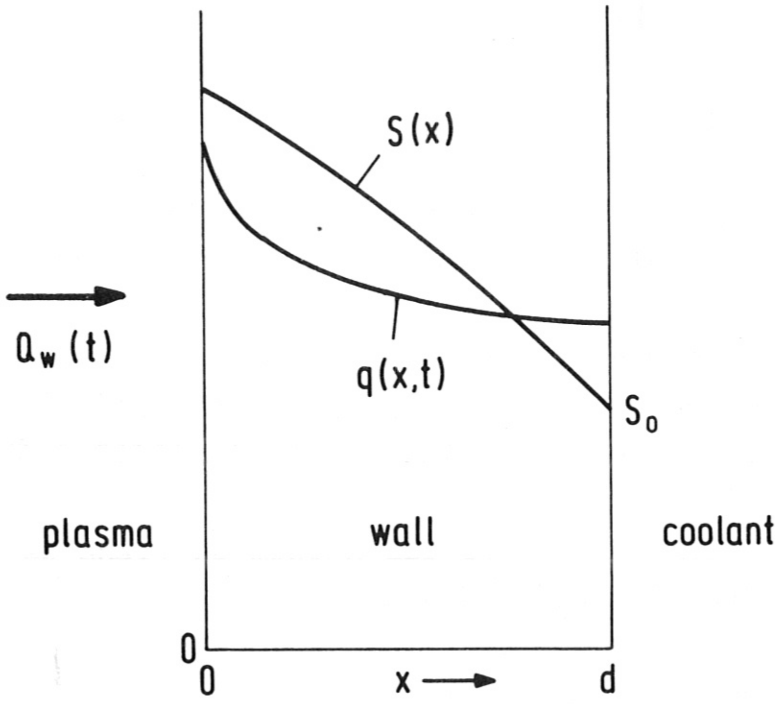

Fig. 3 Schematic view of the geometry and the q and S distributions considered.

We assume as the simplest boundary condition possible that the temperature at the coolant side of the wall is kept fixed at the value ϑ_o for all times, which corresponds to a value S_o of the heat flux potential. If we choose

$$\vartheta_B = \vartheta_o \tag{7}$$

(ϑ_B is the arbitrary reference value of ϑ used in (2)) we get

$$S_o = 0 . \tag{8}$$

In summary, the boundary conditions for S(x,t) are

$$(\partial S/\partial x)\Big|_{x=0} = -Q_W(t), \qquad (9)$$

$$S(d,t) = 0 \qquad (10)$$

(for simplicity we shall use d as symbol for the wall thickness throughout this paper instead of t_{FW} as used in /1/).

To distinguish between the contributions of the volume source q(x,t) and the heat flux density $Q_W(t)$, we split the solution S(x,t) into two parts, which is possible due to the linearity of (5):

$$S(x,t) = S_q(x,t) + S_Q(x,t) . \qquad (11)$$

As boundary conditions we use

$$(\partial S_q/\partial x)_{x=0} = 0 , \qquad (12)$$

$$(\partial S_Q/\partial x)_{x=0} = -Q_W(t), \qquad (13)$$

$$S_q(d,t) = 0 , \qquad (14)$$

$$S_Q(d,t) = 0 . \qquad (15)$$

The boundary conditions (12) to (15) obviously correspond to the boundary conditions (9), (10) for S(x,t).

To determine the solution S(x,t) completely, we have to specify S(x,t) at a given instant. We choose this instant to be the origin of the time coordinate t. We require

$$\lim_{t \to 0} S = S(x,0), \qquad (16)$$

which we can split because of (11) into

$$\lim_{t \to 0} S_q = S(x,0), \tag{17}$$

$$\lim_{t \to 0} S_Q = 0 \tag{18}$$

S(x,0) is the given distribution of S at t = 0.

2.1.3. Symmetries

Because we shall be making use of the method of separation of variables for solving (5), we have to deal with spatial Fourier expansions.

To restrict the series solutions to cos terms in space, we assume $q_x(x)$ and $S_q(x,0)$ to be even functions of x:

$$q_x(x) = q_x(-x), \tag{19}$$

$$S_q(x,0) = S_q(-x,0). \tag{20}$$

To omit terms of even order from the Fourier expansions, which would conflict with the boundary conditions (14) and (15), we further assume for $q_x(x)$ and $S_q(x,0)$ the symmetries

$$q_x(x + 2d) = -q_x(x) \tag{21}$$

$$S_q(x + 2d,0) = -S_q(x,0). \tag{22}$$

The symmetries (19) to (22) and the resulting symmetries of $S_q(x,t)$ and $S_Q(x,t)$ are visualized by Fig. 4.

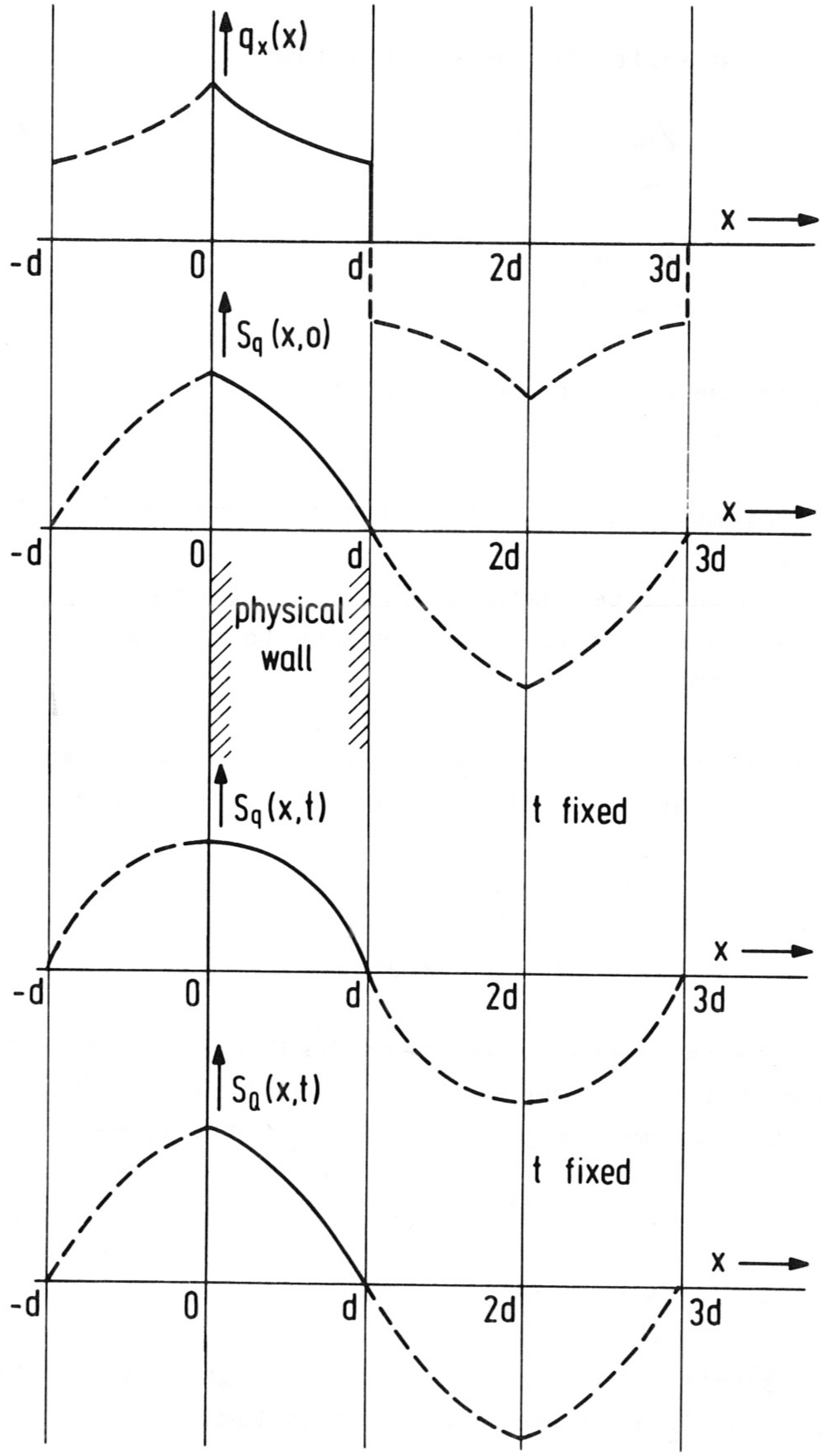

Fig. 4 Extensions of the distributions to a period length 4.d to make Fourier expansions possible.

2.2. Solutions for prescribed power density q(x,t)

Because of (6) the differential equation (5) assumes the form

$$\frac{\partial^2 S}{\partial x^2} + q_x(x) q_t(t) = \alpha_o \frac{\partial S}{\partial t}. \tag{23}$$

2.2.1. "Fourier solution" for arbitrary $q_x(x)$ and $q_t(t)$

We put

$$S_q(x,t) = \sum_\nu S_{q,\nu} = \sum_\nu A_\nu X_\nu(x) T_\nu(t). \tag{24}$$

By inserting (24) into the differential equation (23) and taking into account the boundary conditions (12) and (14) together with the symmetry (19) we get

$$X_\nu(x) = \cos\left(\nu \frac{\pi}{2} \frac{x}{d}\right), \quad \nu = 1,3,5,\ldots \tag{25}$$

and

$$\frac{dT_\nu}{dt} + \frac{1}{\alpha_o} \left(\frac{\nu\pi}{2d}\right)^2 T_\nu = \frac{C_{q,\nu}}{\alpha_o A_\nu} q_t(t). \tag{26}$$

The coefficients $C_{q,\nu}$ result from the Fourier expansion

$$q_x(x) = \sum_{\nu=1,3..}^{\infty} C_{q,\nu} \cos\left(\nu \frac{\pi}{2} \frac{x}{d}\right), \tag{27}$$

$$C_{q,\nu} = \frac{2}{d} \int_0^d q_x(x) \cos\left(\nu \frac{\pi}{2} \frac{x}{d}\right) dx, \quad \nu = 1,3,5.. \tag{28}$$

Equation (28) is valid because of the symmetry (19).

Equation (26) can be solved by integrating the homogeneous equation and adding a special solution of the inhomogeneous equation found by the method of the "variation of the constant". The result is

$$T_\nu(t) = C_{S,\nu}\, e^{-t/\tau_\nu} + \frac{1}{\alpha_0}\, C_{q,\nu}\, e^{-t/\tau_\nu} \int_0^t q_t(t')\, e^{t'/\tau_\nu} dt' \qquad (29)$$

with

$$C_{S,\nu} = \frac{2}{d} \int_0^d S(x,0) \cos\left(\nu \frac{\pi}{2} \frac{x}{d}\right) dx \qquad (30)$$

and

$$\tau_\nu = \frac{1}{\nu^2}\, \alpha_0 \left(\frac{2d}{\pi}\right)^2 \qquad (31)$$

((30) is valid because of (22)).

The coefficients $C_{S,\nu}$ according to (30) are the coefficients of the Fourier expansion of the initial distribution $S(x,0)$:

$$S(x,0) = \sum_{\nu=1,3..}^{\infty} C_{S,\nu} \cos\left(\nu \frac{\pi}{2} \frac{x}{d}\right) dx. \qquad (32)$$

The complete solution of (23) is

$$S_q(x,t) = \sum_{n=0}^{\infty} \cos\left[(2n+1) \frac{\pi}{2} \frac{x}{d}\right] e^{-t/\tau_n} \left[C_{S,n} + \frac{1}{\alpha_0} C_{q,n} \int_0^t q_t(t')\, e^{t'/\tau_n} dt'\right] , \qquad (33)$$

where we have introduced

$$2.n+1 = \nu .$$

This leads to

$$C_{S,n} = \frac{2}{d} \int_0^d S(x,0) \cos\left[(2n+1) \frac{\pi}{2} \frac{x}{d}\right] dx \qquad (34)$$

$$C_{q,n} = \frac{2}{d} \int_0^d q_x(x) \cos\left[(2n+1) \frac{\pi}{2} \frac{x}{d}\right] dx, \qquad (35)$$

$$\tau_n = \frac{1}{(2n+1)^2}\, \alpha_0 \left(\frac{2d}{\pi}\right)^2 = \frac{1}{(2n+1)^2}\, \tau_d . \qquad (36).$$

2.2.2. "Fourier solution" for arbitrary $q_x(x)$ and periodical $q_t(t)$

Because periodical operation may be the working mode of fusion reactors, we apply the general solution (33) to the case of $q_t(t)$ varying periodically with period τ. Figure 5 shows a typical example for $q_t(t)$ calculated for a tokamak reactor plasma /2/. We expand $q_t(t)$ in the following Fourier series ($\omega = 2\pi/\tau$):

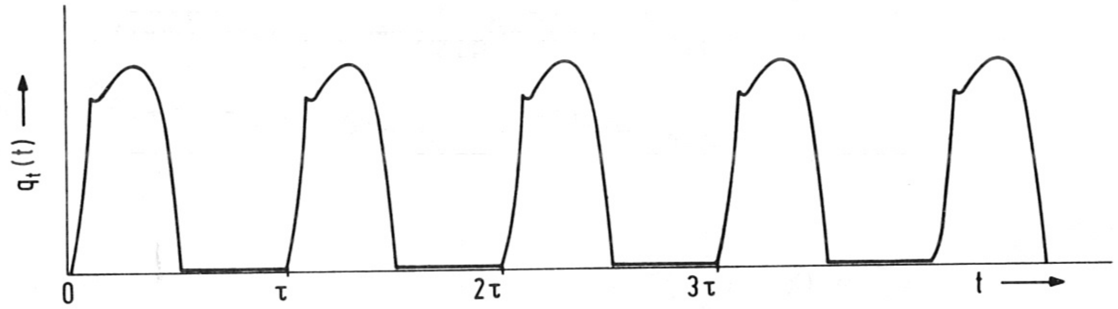

Fig. 5 Typical variation with time of the power density released within the wall as a result of nuclear reactions.

$$q_t(t) = \sum_{m=0}^{\infty} \left[C_{q,m} \cos(m\omega t) + S_{q,m} \sin(m\omega t) \right], \qquad (37)$$

$$C_{q,0} = \frac{1}{\tau} \int_0^{\tau} q_t(t)\, dt, \qquad (38)$$

$$C_{q,m} = \frac{2}{\tau} \int_0^{\tau} q_t(t) \cos(m\omega t) dt, \quad m = 1,2,3,.. \qquad (39)$$

$$S_{q,m} = \frac{2}{\tau} \int_0^{\tau} q_t(t) \sin(m\omega t) dt, \quad m = 1,2,3,.. . \qquad (40)$$

By inserting (37) (with argument t replaced by t') in (33) and performing the integrations we get

$$S_q(x,t) = \sum_{m=0}^{\infty} C_{S,n} e^{-(2n+1)^2\ t/\tau_d} \cos\left[(2n+1)\frac{\pi}{2}\frac{x}{d}\right]$$

$$+ \sum_{n=0}^{\infty} \frac{4\ d^2}{\pi^2}\ C_{q,n} \cos\left[(2n+1)\ \frac{\ }{2}\cdot\frac{x}{d}\right] \times$$

$$\times \sum_{m=0}^{\infty} \frac{1}{(2n+1)^4+(m\omega\tau_d)^2} \times$$

$$\times\left[(C_{q,m}(m\omega\tau_d)+S_{q,m}(2n+1)^2).\sin\ (m\omega t)\ +\right.$$

$$+\ (C_{q,m}(2n+1)^2-S_{q,m}(m\omega\tau_d)).\cos\ (m\omega t)$$

$$\left.-\ (C_{q,m}(2n+1)^2-S_{q,m}(m\omega\tau_d)).\,e^{-(2n+1)^2.\,t/\tau_d}\right] \qquad (41)$$

with

$$\tau_d = \alpha_o\ (\frac{2d}{\pi})^2\ . \qquad (42).$$

The solution (41) approaches a periodical behaviour in t for times large compared with $\tau_d (t/\tau_d \gtrsim 4)$. This time constant is determined by the wall thickness d and the wall material. For a stainless steel wall of 1 cm thickness τ is about 10 s (values for other wall materials are shown in Table II).

2.2.3. "Source solution" for arbitrary $q_x(x)$ and $q_t(t)$

We start with that solution of (23) which describes the case of an instantaneous plane source in an infinite medium. If we deliver per unit area the heat d^2Q at the location x_s at the time instant t_s, this solution is /3/

$$d^2S_{q,}\ (x,t\ x_s,t_s) = \frac{d^2Q(x_s,t_s)}{(4\pi\alpha_o)^{1/2}}\ \frac{1}{(t-t_s)^{1/2}}\ \exp\left[-\frac{\alpha_o(x-x_s)^2}{4\ (t-t_s)}\right]. \qquad (43)$$

Table II: Time constants τ_d s of a 1 cm thick wall for various materials and temperatures

Temp. C	1.4970 Stainl.steel	Molybdenum	Niobium	Vanadium	Aluminium
0	10.82	0.74	1.78	4.18	0.41
100	10.89	0.78	1.82	3.99	0.43
200	10.55	0.83	1.69	3.84	0.44
300	10.09	0.87	1.64	3.63	0.46
400	9.69	0.92	1.60	3.49	0.48
500	9.39	0.97	1.57	3.32	-
600	9.22	1.01	1.54	3.21	-
700	9.06	1.06	1.50	3.08	-
800	-	1.11	1.47	2.95	-
900	-	1.15	1.44	-	-
1000	-	1.20	1.42	-	-

By integrating this solution with respect to x_s and t_s we get solutions for sources extended in space and time such as $q(x_s, t_s)$. Because of

$$d^2Q(x_s,t_s) = q_x(x_s)q_t(t_s)dx_s\, dt_s \tag{44}$$

we get for $S_{q,\infty}(x,t)$

$$S_{q,\infty}(x,t) = \frac{1}{(2\pi\alpha_0)^{1/2}} \int_{t_s=0}^{t} \int_{x_s=-d}^{d} \frac{q_x(x_s)q_t(t_s)}{(t-t_s)^{1/2}} \times$$

$$\times \exp\left[-\frac{\alpha_0(x-x_s)^2}{4(t-t_s)}\right] dx_s\, dt_s. \tag{45}$$

The solution (45) meets the boundary condition (12), but it does not vanish at $x = d$ as it should according to (15). We can construct the solution which also obeys (15) by using the concept of "reflection at the boundary". This means that we add to (45) the function $- S_{q,\infty}(2d-x,t)$, which is antisymmetric to $S_{q,}(x,t)$ with respect to $x = d$. Now (15) is fulfilled but (12) is violated. To right this, we have to add $-S_{q,\infty}(-2d-x,t)$. Continuation of this procedure leads to an infinite series solution

$$S_q(x,t) = \sum_{n=-\infty}^{\infty} (-1)^{/n/} S_{q,\infty}(2nd-x,t) \qquad (46)$$

with $S_{q,\infty}$ from (45). When calculating $S_q(x,t)$ from (46), we have to keep in mind that $S_{q,\infty}(x,t)$ is an even function of x. The series solution (46) would also have resulted from a formal solution of (23), (12) and (14) by means of the Laplace transform.

Obviously, the solutions (45), (46) is especially applicable for small values of t and for functions $q_x(x)$ which are strongly localized in space such as $q_x(x) \sim e^{-/ux}$ for $/ud \ll 1$. We shall come back to this case in Section 2.5.5.

2.3. Solutions for prescribed heat flux density $Q_w(t)$ at $x = 0$

2.3.1. "Fourier solution" for arbitrary heat flux density $Q_w(t)$

We start from the solution $S_{Q,c}(x,t)$ of (23) for a heat flux density Q_c at $x = 0$ which is constant in time. With a mathematical procedure similar to that in Section 2.2.1. we find the solution /4/

$$S_{Q,c}(x,t;Q_c)=Q_c(d-x)-Q_c\frac{8d}{\pi^2}\sum_{n=0}^{\infty}\frac{1}{(2n+1)^2}\,e^{-t/\tau_n}\cos\left[(2n+1)\,\frac{\pi}{2}\,\frac{x}{d}\right] \qquad (47)$$

with τ_n according to (36). The solution meets the boundary condition (15) and the initial condition $S_{Q,c}(x,0) = 0$.

From (47) we can calculate the solution for a time dependent Q_w by using the theorem of Duhamel /5/, /6/:

$$S_Q(x,t) = S(x,0) + \int_0^t S_{Q,c}\left[x,t-t';Q\,(t')\right]dt' \ . \qquad (48)$$

$S_{Q,c}$ under the integral sign is $S_{Q,c}$ according to (47) with t replaced by (t-t') and Q_c replaced by Q (t'). According to (18) one has S(x,0) = 0 in (48). By performing the integration in (48) we get

$$S_Q(x,t)=\frac{2}{d\alpha_o}\sum_{n=0}^{\infty}\cos\left[(2n+1)\,\frac{\pi}{2}\,\frac{x}{d}\right]e^{-t/\tau_n}\int_{t_s=0}^{t}Q_w(t')e^{t'/\tau_n}dt' . \qquad (49)$$

2.3.2. "Fourier solution" for periodical Q_w (t)

We expand the periodically varying Q_w (t) in the Fourier series ($\omega = 2\pi/\tau$)

$$Q_w(t) = \sum_{m=0}^{\infty} C_{Q,m}\cos(m\omega t) + S_{Q,m}\sin\,(m\omega t) \qquad (50)$$

with

$$C_{q,0} = \frac{1}{\tau}\int_0^{\tau} Q_w(t)dt,$$

$$C_{Q,m} = \frac{2}{\tau}\int_0^{\tau} Q_w(t)\,\cos(m\omega t)dt, \ m = 1,2,3,\dots \qquad (51)$$

$$S_{Q,m} = \frac{2}{\tau}\int_0^{\tau} Q_w\,(t)\,\sin\,(m\omega t)dt, \ m = 1,2,3,\dots \ . \qquad (52)$$

From (49) and (50) we get substituting t' for t in (50)

$$S_Q(x,t) = \frac{8d}{2} \sum_{n=0}^{\infty} \Big\{ \cos \left[(2n+1) \frac{\pi}{2} \frac{x}{d} \right] \times$$

$$\times \sum_{m=0}^{\infty} \frac{1}{(2n+1)^4 + (m\omega\tau_d)^2} \times$$

$$\times \Big[(C_{Q,m}(m\omega\tau_d) + S_{Q,m}(2n+1)^2) . \sin (m\omega t) +$$

$$+ \ (C_{Q,m}(2n+1)^2 - S_{Q,m}(m\omega\tau_d)) . (\cos (m\omega t) - e^{-(2n+1)^2 \ t/\tau_d}) \Big] \Big\} .$$

(53)

2.4. Relation between solutions for strongly localized $q_x(x)$ and for given $Q_w(t)$

The solution for a heat source strongly localized at $x = 0$ is intuitively expected to couverge with increasing degree of localization towards the solution for a heat flux from outside at $x = 0$.

This can be formally confirmed by assuming that $q_x(x)$ behaves like a δ-function. To be consistent with the symmetries assumed in Section 2.1.3., we choose for q_x the periodical distribution shown schematically in Fig. 6 ($\xi = x/d$).

In the vicinity of $\xi = x/d = 0$ the spatial variation of q_x is given by

$$q_x(\xi) = c\,\delta(\xi) \qquad (54)$$

with $$\int_{-\infty}^{\infty} \delta(\xi)\, d\xi = 1$$

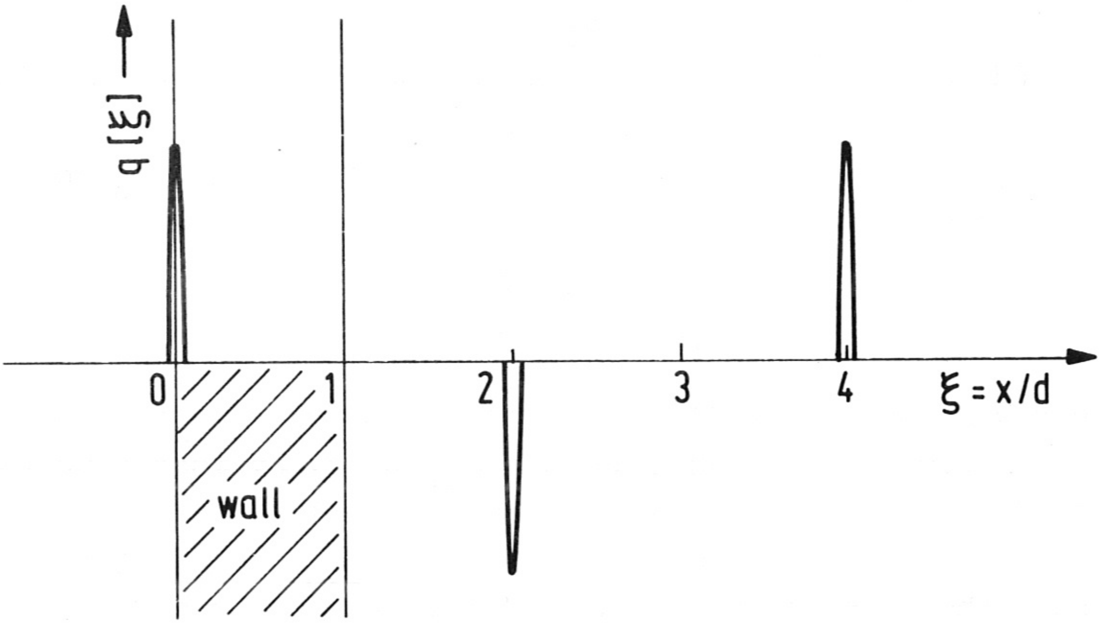

Fig. 6 Idealized distribution of localized heat sources within the wall.

Because we want to compare with the solution for given Q_w (t), we determine the constant C from the condition

$$d \int_{-1}^{1} q_x(\xi)\, q_t(t)\, d\xi = 2Q_w(t), \tag{55}$$

which means that the amount of heat delivered to the solid is the same for the two cases. The factor 2 in (55) occurs because only half of the heat from q is delivered to the region $\xi > 0$.

From (54) and (55) we get

$$q_x(\xi) = \frac{2}{d} \frac{Q_w(t)}{q_t(t)} \sum_{p=0}^{\infty} \delta(\xi - p). \tag{56}$$

The Fourier expansion of the distribution shown in Fig. 6 is given by

$$q_x(\xi)=q_x(\tfrac{x}{d})=\frac{2}{d}\,\frac{Q_w(t)}{q_t(t)}\sum_{n=0}^{\infty}\cos\left[(2n+1)\,\frac{\pi}{2}\,\frac{x}{d}\right]. \qquad (57)$$

From (57) we read that the Fourier coefficients $C_{q,n}$ according to (35) are

$$C_{q,n}=\frac{2}{d}\,\frac{Q_w\,(t)}{q_t(t)}\,. \qquad (58)$$

We now go back to (33), the solution for given $q_x(x)$ for the case $S(x,0) = 0$ (which leads to $C_{s,n} = 0$). By inserting (58) in (33) we exactly reproduce (49), the solution for given $Q_w\,(t)$ at $x = 0$. In doing this we put $C_{q,n}$ according to (58) under the integral in (33). This can be done because $Q_w\,(t)/q_t(t)$ does not depend on t as is expressed by (56).

We shall come back to the case of strongly localized heat sources in connection with practical examples (Section 2.5.5.).

2.5. Practical examples

2.5.1 "Fourier solution" for $q_x(x)$ = const, $q_t(t) = 1$

We assume

$$q_x(x) = q_{xo} = \text{const for } 0 \leqslant x < d, \qquad (59)$$

$$q_t(t) = 1. \qquad (60)$$

The conditions (59), (60) lead to the stationary solution of (23) given by

$$S_q(x) = \frac{1}{2}\,q_{xo}\,(d^2 - x^2),\ 0 \leqslant x \leqslant d. \qquad (61)$$

By inserting (59), (60) into (41) we get for the stationary case ($t/\tau_d \rightarrow \infty$)

$$S_q(x) = \frac{16\, d^2}{\pi^3} q_{xo} \sum_{n=0}^{\infty} \frac{(-1)^2}{(2n+1)^3} \cos\left[(2n+1)\,\frac{\pi}{2}\,\frac{x}{d}\right] \qquad (62)$$

if we take into account $\omega = 0$, $S_{q,m} = 0$, $C_{q,m} = 0$ for $m \neq 0$, $C_{q,0} = 1$, and the Fourier coefficients

$$C_{q,n} = \frac{4}{\pi}\, q_{xo}\, \frac{(-1)^n}{2.n+1} \qquad (63)$$

Equation (63) follows from (59) and the symmetry (19) described in Section 2.1.3.

The solutions (61) (with the symmetry from Section 2.1.3.) and (62) are mathematically equivalent; (62) is the Fourier expansion of (61).

The rapid convergence of the sum in (62) ($\sim 1/(2n+1)^3$) is visualized by the example shown in Fig. 7 [N = maximum value of n used in the summation of (62)] .

2.5.2. "Fourier solution" for $q_x \sim \delta(x/d)$, $q_t(t) = 1$

To model a heat source strongly localized in space, we choose

$$q_x(x/d) = \frac{2}{d}\, Q_o\, \delta(x/d), \quad 0 \leq x < d \qquad (64)$$

(Q_o = heat per unit area delivered to the solid at $x = 0$).

The Fourier expansion of (64) is again (see Fig. 6 and (57))

$$q(x/d) = \frac{2}{d}\, Q_o \sum_{n=0}^{\infty} \cos\left[(2n+1)\,\frac{\pi}{2}\,\frac{x}{d}\right]. \qquad (65)$$

From (65) we get

$$C_{q,n} = \frac{2}{d}\, Q_o. \qquad (66)$$

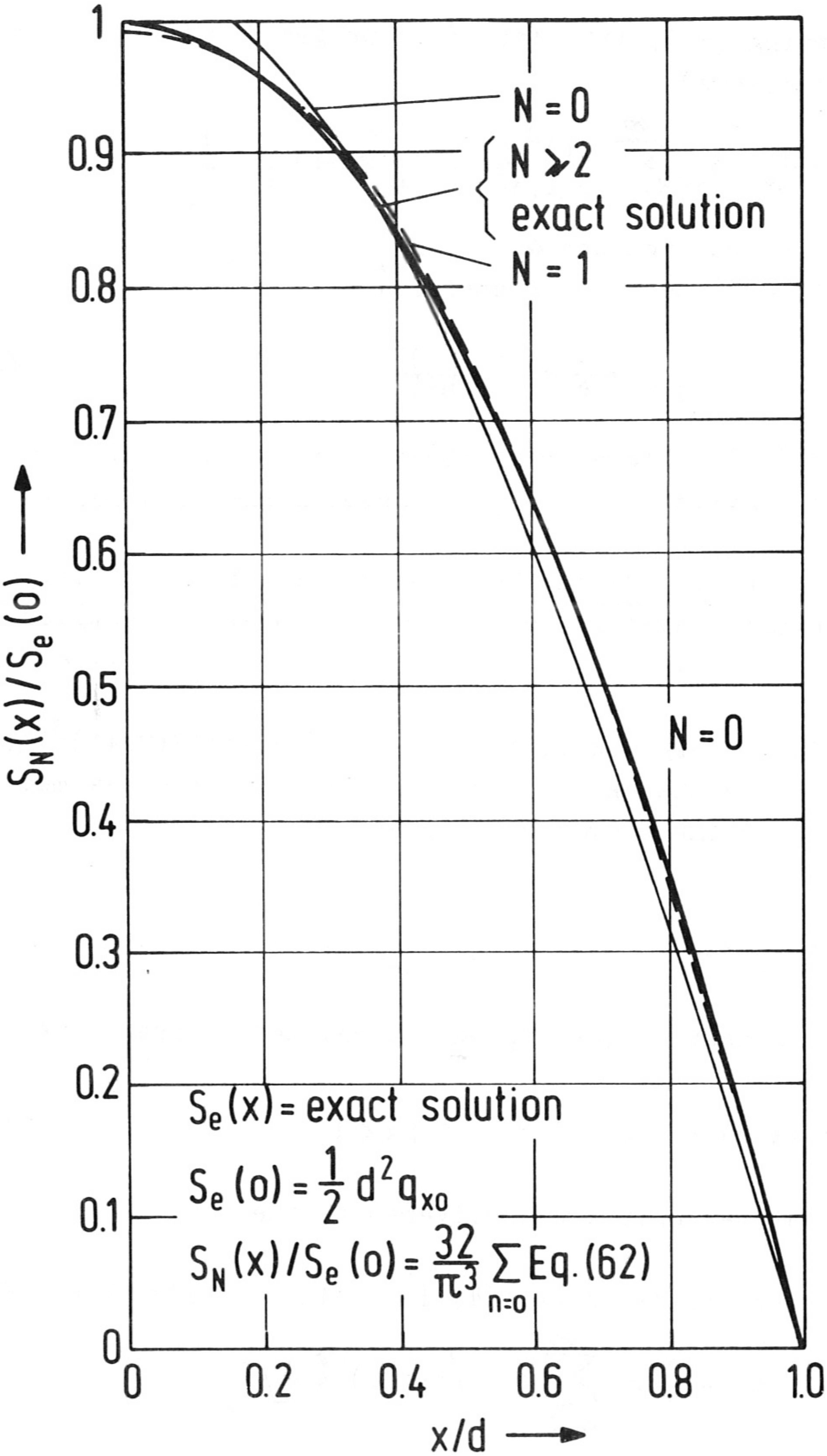

Fig. 7 Comparison of truncated Fourier solutions with the exact result for a heat source constant in space and time.

With (66) we get for the stationary case $q_t(t) = 1$ from (41):

$$S_q(x) = \frac{8d}{\pi^2} Q_o \sum_{n=0}^{\infty} \frac{1}{(2n+1)^2} \cos\left[(2n+1)\frac{\pi}{2}\frac{x}{d}\right]. \tag{67}$$

To get (67), we had to take into account $\omega = 0$, $S_{q,m} = 0$, $C_{q,m} = 0$ for $m \neq 0$, $C_{q,0} = 1$.

The direct stationary solution of (23) for q_x given by (64) is

$$S_q(x) = Q_o(d-x). \tag{68}$$

Equation (67) is the Fourier expansion of (68) for the symmetry assumed in Section 2.1.3.

Figure 8 shows the convergence of (67) towards (68) (N = maximum value of n used in the summation of (67)).

The convergence $\left(\sim 1/(2n+1)^2\right)$ is one order less than in the case q_x = const and can be considered as the worst case of all spatial distributions $q_x(x)$ with respect to convergence.

2.5.3. "Fourier solution" for $q_x(x) = q_{xo} \cos(\frac{\pi}{2}\frac{x}{d})$, $q_t(t) = \frac{1}{2}[1 + \cos(\omega t)]$

With the assumptions

$$q_x(x) = q_{xo} \cos\left(\frac{\pi}{2}\frac{x}{d}\right), \tag{69}$$

$$q_t(t) = \frac{1}{2}\left[1 + \cos(\omega t)\right] \tag{70}$$

we model the case of an extended spatial distribution $q_x(x)$ which varies in time in a pulsed manner, the effective pulse duration being of the same order as the down time.

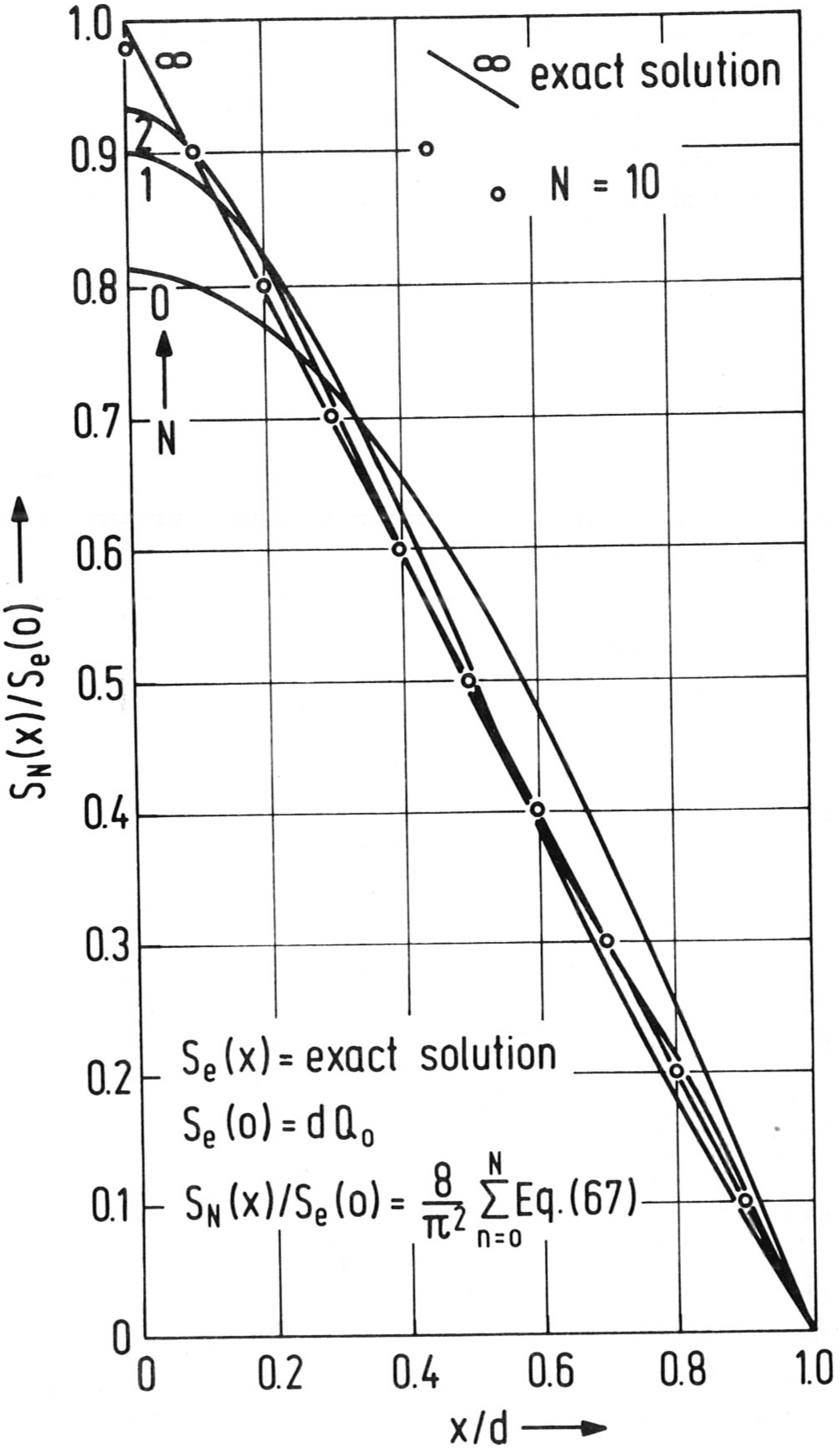

Fig. 8 Comparison of truncated Fourier solutions with the exact result for an external heat flux constant in space and time.

From (69) and (70) we read

$$C_{q,n} = q_{x_o} \text{ for } n = 1,$$

$$C_{q,n} = 0 \text{ for } n > 0,$$

$$S_{q,m} = 0,$$

$$C_{q,m} = \frac{1}{2} \text{ for } m = 0 \text{ and } 1,$$

$$C_{q,m} = 0 \text{ for } m > 1.$$

By using these values we get from (41) for $t \gg \tau_d$ the periodically varying S-distribution

$$S_q(x,t) = \frac{2d^2}{\pi^2} q_{x_o} \cos\left(\frac{\pi}{2}\frac{x}{d}\right)\left[1 + \frac{d}{1+(\omega\tau_d)^2}\sin\omega t + \frac{1}{1+(\omega\tau_d)^2}\cos\omega t\right]$$

$$= \frac{2d^2}{\pi^2} q_{x_o} \cos\left(\frac{\pi}{2}\frac{x}{d}\right)\left[1 + \frac{1}{\sqrt{1+(\omega\tau_d)^2}}\sin(\omega t + \varphi)\right. \tag{71}$$

with

$$\varphi = \text{arc tg}\left(\frac{1}{\omega\tau_d}\right).$$

To get an idea of the magnitude of the fluctuations of $S_q(x,t)$ in time produced by the periodically fluctuating $q_t(t)$, we calculate the ratio

$$r_t = \frac{S_{q,max} - S_{q,min}}{S_{q,max} + S_{q,min}} \tag{72}$$

with

$$S_{q,max} = \text{Max}\left[S_q(x,t)\right], \tag{73}$$

$$S_{q,min} = \text{Min}\left[S_q(x,t)\right]. \tag{74}$$

These values occur at

$$(\omega t)_{max} = \text{arc tg}\,(\omega \tau_d) + r \cdot 2\pi \qquad (75)$$

and

$$(\omega t)_{min} = \text{arc tg}\,(\omega \tau_d) + (r + 1/2) \cdot 2\pi \qquad (76)$$

respectively.

By using elementary relations between trigonometric functions we get

$$r_f = \frac{1}{\left[1+(\omega\tau_d)^2\right]^{1/2}} = \frac{1}{\left[1+(2\pi)^2(\tau_d/\tau)^2\right]^{1/2}} \; .(77)$$

Figure 9 shows r_f vs. τ_d/τ. We see that for small values of τ_d/τ which correspond to the practically interesting

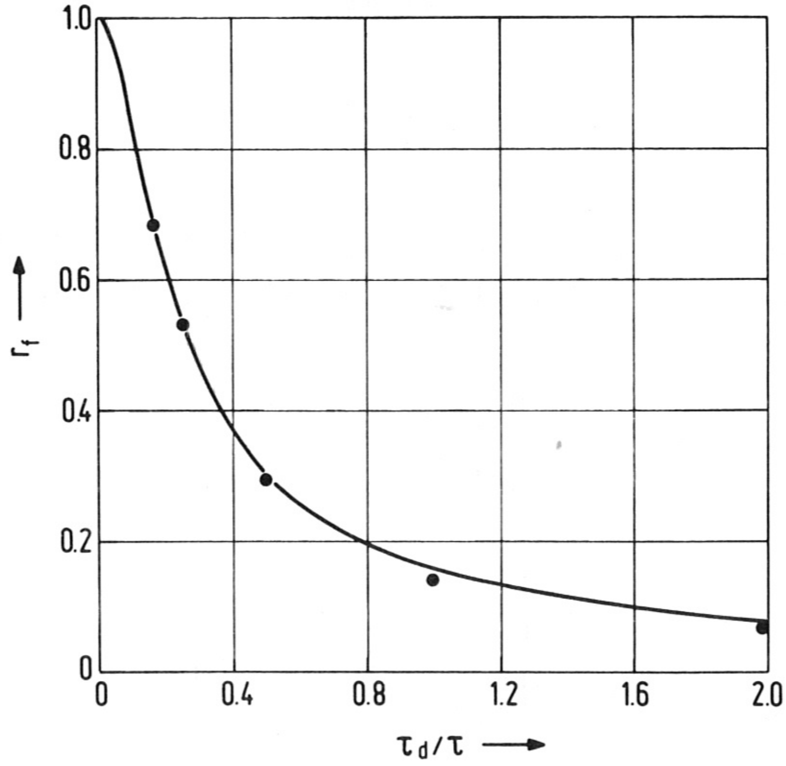

Fig. 9 Degree of modulation r_f produced by periodically varying heat sources as a function of τ_d/τ (= wall time constant/period length).

case of long pulse duration the values of r_f are close to unity. This means that the wall temperature at any point fluctuates with a high degree of modulation. This demonstrates that the thermal inertia of the wall for practical wall thicknesses has little damping effect if the pulse duration and down time are of the same order.

2.5.4. "Fourier solution" for $q_t(t)$ as a periodical sequence of δ-functions

We assume the following distributions $q_x(x)$ and $q_t(t)$:

$$q_x(x) = \frac{h_{x_o}}{\tau} \cos\left(\frac{\pi}{2}\frac{x}{d}\right), \tag{78}$$

$$q_t(t) = \tau \sum_{p=0}^{\infty} \delta(t-p\tau) \tag{79}$$

(h_{x_o} = heat delivered per unit volume at x = 0, τ = period length, $\int_{-\infty}^{\infty}\delta(t)\,dt = 1$).

By means of (78) and (79) we model the case of an extended spatial distribution $q_x(x)$ which varies with t in a pulsed manner, the pulse length being very short compared with the period .

The distribution (79) is shown schematically in Fig. 10.

The Fourier expansion of (79) is given by

$$q_t(t) = 1+2\sum_{m=1}^{\infty} \cos(m\omega t). \tag{80}$$

From (80) we read

$$C_{q,0} = 1$$
$$C_{q,m} = 2 \text{ for } m > 0, \tag{81}$$
$$S_{q,m} = 0.$$

For $t \gg \tau_d$ we get with (81) from (41)

$$S_q(x,t = \frac{4d^2}{\pi^2} \frac{h_{xo}}{\tau} \cos\left[(2n+1)\frac{\pi}{2}\frac{x}{d}\right] \ast$$
$$\left\{1 + \sum_{m=1}^{\infty} \frac{2}{1+(m\omega\tau_d)^2}\left[(m\omega\tau_d)\sin(m\omega t)+\cos(m\omega t)\right]\right\}. \qquad (82)$$

The convergence of the summation in (82) is very poor ($\sim 1/m$ for the sine term). Therefore, the Fourier formalism is not adequate for solving the problem of a periodical sequence of "heat spikes".

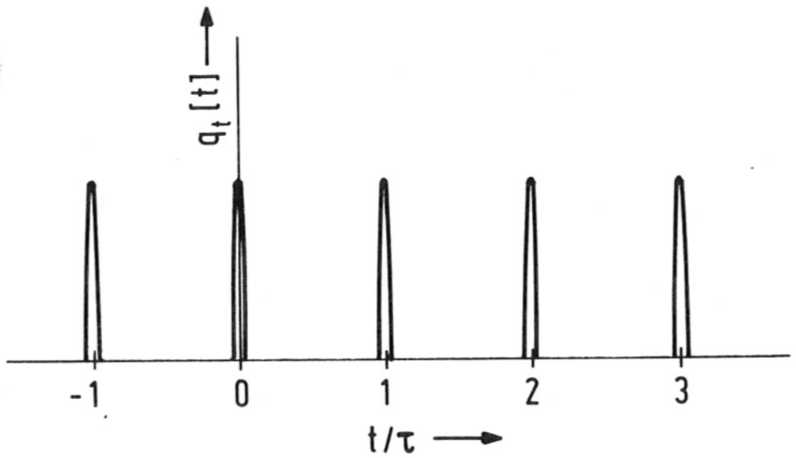

Fig. 10 Idealized sequence of pulsed heat sources.

For such problems one should use (33) to calculate the time behaviour during one period and start a new calculation with the beginning of a new spike. At this point in time one has to use the distribution of S_q as initial values $S_a(x,0)$ for the next step. For $\tau \gg \tau_d$ these values are virtually zero. In this case we get from (33) for $0 \leq t < \tau$ (with $C_{S,n} = 0$)

$$S_q(x,t) = \frac{4}{\pi}\,\frac{h_{xo}}{\alpha_o}\,\cos\left[(2n+1)\,\frac{\pi}{2}\,\frac{x}{d}\right] e^{-t/\tau_d}. \qquad (83)$$

$S_q(x,t)$ according to (83) repeats periodically in time with period τ.

2.5.5. "Source solution" for $q_x(x) = q_{x_o}\, e^{-\mu x}$ and arbitrary $q_t(t)$

We assume for $q_x(x)$ the distribution

$$q_x(x) = q_{x_o}\, e^{-\mu x} = q_{x_o}\, e^{-x/\delta} \qquad (84)$$

with the additional condition

$$e^{-\mu d} = e^{-d/\delta} \ll 1 \qquad (85)$$

(we use the "1/e length" δ instead of the "half-length" $h = \ln 2/\mu$ used in /1/).

Condition (85) means that the heat input is strongly peaked at $x = 0$. Physically, (84) describes the heat produced by the absorption of plasma radiation. This heat is expected to be absorbed in a very thin layer which leads to the condition (85).

The investigations of this section are intended to clarify the possibility of replacing the exact solution for $q_x \sim e^{-\mu x}$ by a solution for an equivalent heat flux entering the solid from outside. The complete equivalence of such solutions has been shown in Section 2.4. for the extreme case of q_x behaving like a δ-function.

We introduce (84) in the source solution (45). By using the condition (85) we can replace the limits of integration d and -d by ∞ and $-\infty$ respectively. Then the integration with respect to t_s can be performed analytically. The result is

$$S_{q,}(x,t)=\frac{q_{x_0}}{2\alpha_0}e^{t/\tau_\delta}\Big\{2\cos h(x/\delta)\int_0^t q_t(t_s)e^{-t_s/\tau_\delta}\,dt_s$$

$$-\int_0^t q_t(t_s)e^{-t_s/\delta}\Big[e^{-x/\delta}\operatorname{erf}\Big[\Big(\frac{t-t_s}{\tau_\delta}\Big)^{1/2}-\frac{\tau_\delta^{1/2}x/\delta}{2(t-t_s)^{1/2}}$$

$$+e^{x/\delta}\operatorname{erf}\Big[\Big(\frac{t-t_s}{\tau_\delta}\Big)^{1/2}+\frac{\tau_\delta^{1/2}x/\delta}{2(t-t_s)^{1/2}}\Big]\Big]\,dt_s\Big\} \qquad (86)$$

with

$$\tau_\delta=\alpha_0\,\delta^2. \qquad (87)$$

By (87) we introduce a second thermal time scale τ_δ in addition to τ_d according to (36). Between τ_δ and τ_d the following relationship holds:

$$\frac{\tau}{\tau_d}=\Big(\frac{\pi}{2}\Big)^2\Big(\frac{\delta}{d}\Big)^2. \qquad (88)$$

Equation (88) shows that τ is much smaller than τ_d because of condition (85). τ_δ gives the order of magnitude of the time during which the layer near $x = 0$ is heated up adiabatically by the absorption of radiation. For $t > \tau_\delta$ heat conduction comes into play and the temperature increase with t becomes increasingly smaller (see Fig. 12: curves t/τ_d and $S_{q,\infty}(0,t)$).

If we take the boundary condition (14) ($S_q(d,t) = 0$) into account by using (46) the time constant τ_d also becomes important. Equations (86) and (46) do not show this fact explicitly, but it is clear from dimensional reasoning and also from the Fourier solutions discussed earlier.

As an example we show the development of $S_q(x,t)$ according to (86), (46) from the initial values $S_q(x,0) = 0$ to the steady state for the case $q_t(t) = 1$. The stationary solution of (23) for this case is given by

$$S_q(x,t\rightarrow\infty) = q_{x_o}\delta^2\left(\frac{d}{\delta} - \frac{x}{\delta} - e^{-x/\delta} + e^{-d/\delta}\right). \qquad (89)$$

Figure 11 shows $S_q(x,t)$ (solid curves) calculated from (86) and (46) as a function of x/d with t/τ_d as parameter. The values of the parameters involved are: $\alpha_o = 25$ s/cm^2, $d = 1$ cm, $\delta = 0.1$ cm, $\tau_d = 10.13$ s, $\tau_\delta = 0.25$ s.

For comparison we show the solution calculated on the assumption that the same amount of heat is delivered to the solid by an external heat flux. This problem has been solved in Section 2.3.1. This solution according to (49) is also shown in Fig. 11 (dashed curves). Obviously, the use of the time scale τ_δ is now formal. It is only used to make the comparison possible. The steady state solution for this case is

$$S_Q(x,t\rightarrow\infty) = Q_o(d-x). \qquad (90)$$

The assumption of equal input in both cases leads to

$$Q_o = q_{x_o}\delta \text{ for } e^{-d/\delta} \ll 1. \qquad (91)$$

From (90) and (91) we get

$$S_Q(x,t\rightarrow\infty) = q_{x_o}\delta(d-x). \qquad (92)$$

Figure 11 shows that the maximum differences between the two cases occur at $x = 0$. To get an idea of the error perpetrated by using S_Q instead of S_q, we calculate the ratio

$$\left(\frac{S_Q - S_q}{S_q}\right)_{x=0,t\rightarrow\infty} = \frac{\delta(1-e^{-d/\delta})}{d-\delta} \approx \frac{\delta}{d}. \qquad (93)$$

The ratio $\delta/d = 0.1$ used in Fig. 11 was choosen for demonstration. In practice, we expect δ/d values of 10^{-2} or less, so that

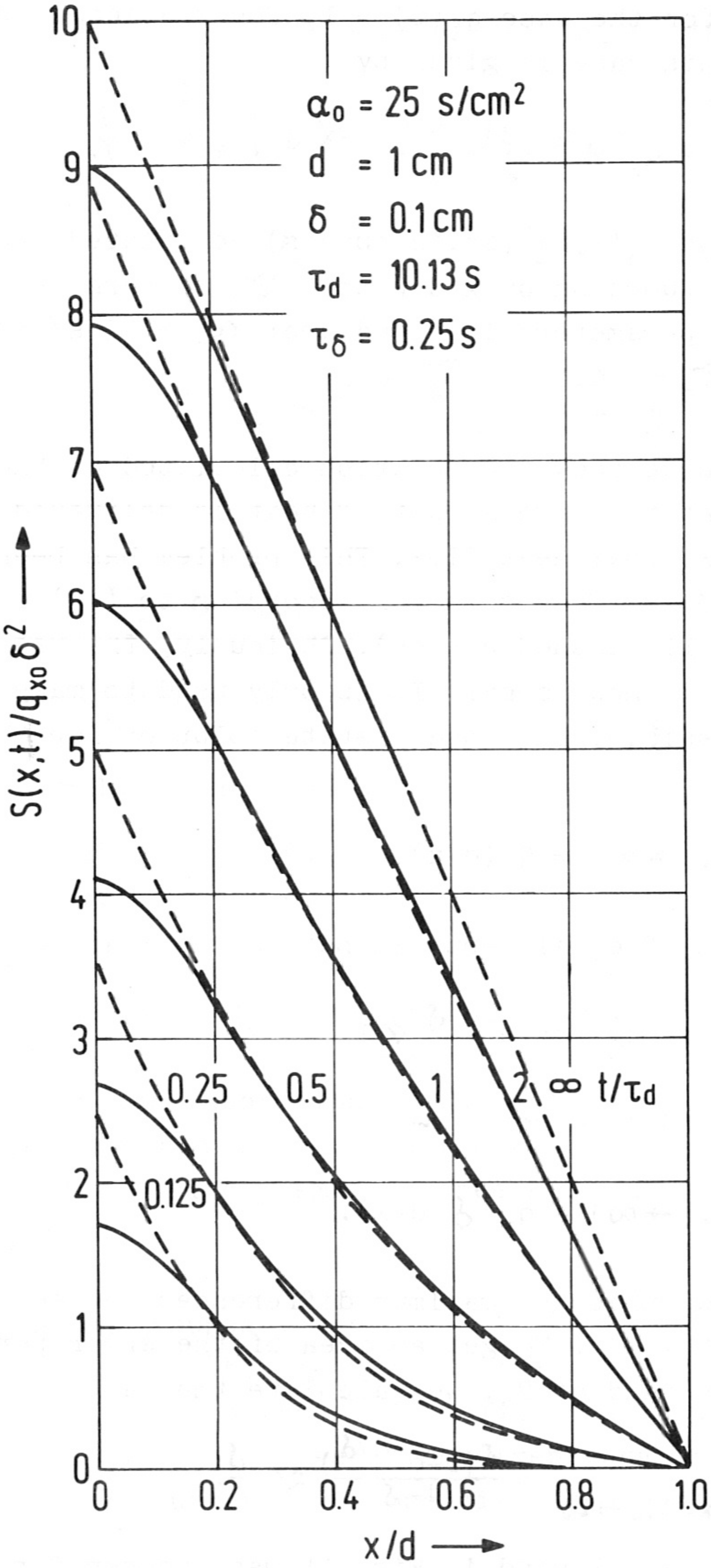

Fig.11 Comparison of S distributions for a heat source strongly peaked at x = 0 (solid curves) with those for an external heat flux (dashed curves).

we conclude from (93) that S_Q can be used instead of S_q for most practical cases. This is true only if we are interested in S-distributions and do not need the derivative $\partial S/\partial x$.

The use of S_Q instead of S_q offers distinct calculational advantages:

- the use of the source solution (45) can be avoided, which is advantageous because (45) and (46) mostly lead to the cumbersome necessity of numerically manipulating error function type solutions of large arguments (see, for instance, the example given by (86)). The source solutions are, on the other hand, well suited to investigating S_q-distributions of very small times t (see end of this section).

- it is true that using the Fourier solutions (33) or (41) for S_q instead of the source solution (45) makes the numerical situation better, but one has to take quite a high number of sum terms into account.

This is due to the $1/(2n+1)^2$ convergence in the case of strongly localized sources as shown in Section 2.5.2.

It is obvious that the boundary condition $S(d,t) = 0$ affects the solution only for times comparable to or larger than the time constant τ_d. Figure 12 demonstrates this fact: $S_q(0,t)$ and $S_{q,\infty}(0,t)$, the first term of the series (46), are close together for $0 \lesssim t/\tau_d \lesssim 1$ and increasingly diverge for $t/\tau_d > 1$.

S_q is also shown vs. time at the position $x/d = 0.5$. The small time lag near $t=0$ is that time the bulk of released heat needs to diffuse to $x/d = 0.5$.

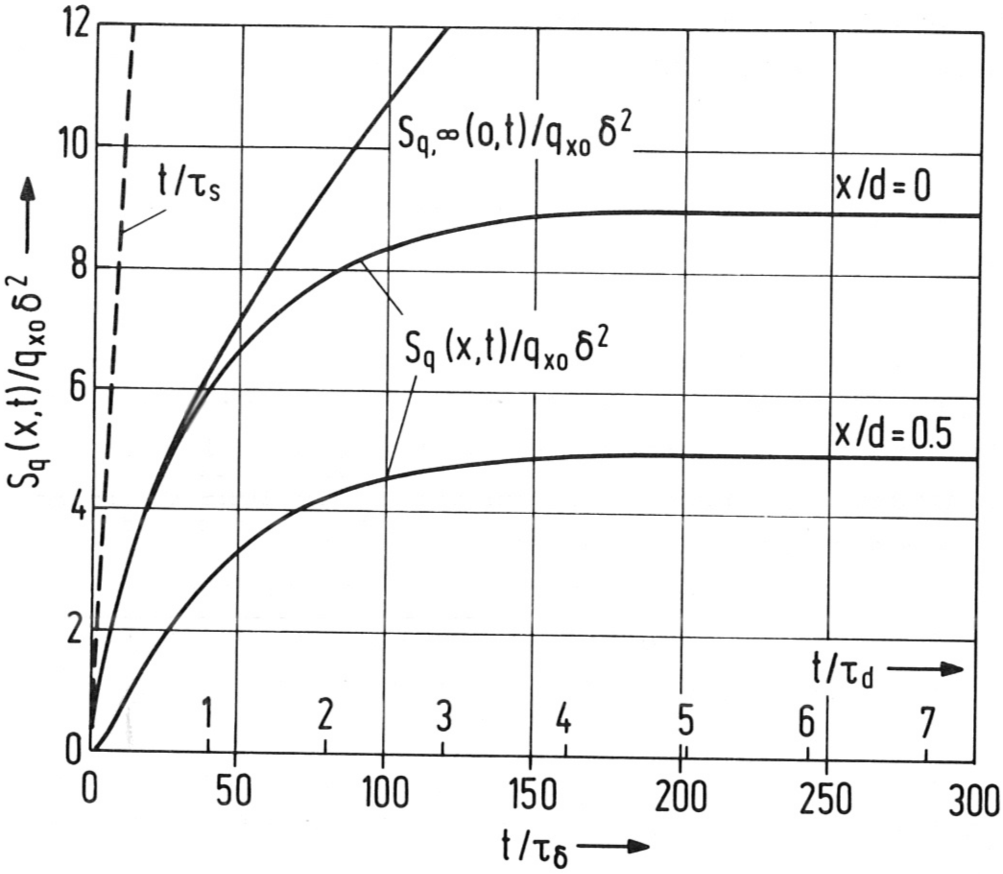

Fig. 12 Comparison of S distributions corresponding to $S(x=d,t) = 0$ at finite d with the case $d \rightarrow \infty$.

For very small times ($t/\tau_\delta \lesssim 1$) the solid is heated adiabatically, as already stated. The expansion of (86) for $q_t(t) = 1$ in the vicinity of $t = 0$ and $x = 0$ is given by

$$S_q(0,t) \approx S_{q,\infty}(0,t) \approx q_{x_0}\delta^2 (t/\tau_\delta) = \frac{q_{x_0}}{\alpha_0} t, \; (t \lesssim \tau_\delta). \quad (94)$$

Relation (94) formally derived from (86) also follows from simple physical reasoning. The dashed line in Fig. 12 represents the relation (94). It is obvious that (94) is not a useful approximation on time scales larger than τ_δ such as, for example, τ_d or the period length τ of most pulsed reactor concepts. An important exception is the case of fusion by inertial confinement.

3. Stress-strain analysis

In practical cases of first wall thermomechanical analysis, we are concerned with a periodic sequence of pulses. Therefore, the solutions presented in Sections 2.2.2. and 2.3.2. are those on which the further considerations will be based. Using equations (41) and (53) the space and time dependence of the heat flux potential S is determined by

$$S(x,t) = S_o + S_q(x,t) + S_Q(x,t). \qquad (95)$$

This equation has to be applied if, deviating from (7), the wall temperature ϑ_o at the coolant side of the wall is not identical with the reference temperature ϑ_B used to define the heat flux potential. By inverting equation (2) we obtain the temperature $\vartheta(x,t)$ from S(x,t).

The remainder of the stress-strain analysis is straightforward. Since there is negligible time delay between the temperature and stress fluctuations, we can consider the problem to be quasi-stationary. This means applying the equations of the steady-state analysis described in /1/ for every time instant desired.

In doing this, we apply equation (95), which was derived for plane geometry only, to cylindrically and spherically shaped first wall contours as well. As was outlined in Section 2.1.1., this approximation is not too bad for realistic ratios of wall thickness and wall radius. Since, however, the mechanical stresses depend very strongly on the geometry, we have to use the equivalent equations for the stress and strain evaluations specified in /1/.

The mechanical performance of a material under pulsed load conditions is generally assessed by means of its fatigue properties. The number of cycles permitted until failure has to be expected depends upon the strain range $\Delta\varepsilon$ between the maximum and minimum values ε_{max} and ε_{min}. Therefore, the evaluation of strains has been introduced as an extension to /1/. The calculated strain range is finally correlated with the fatigue behaviour to arrive again at an estimated lifetime.

4. Computer program

Since the non-stationary analysis relies to a great extent on the solutions and hence on the programs developed for the steady-state case, the program described in /1/ has now been extended to cover both types of analysis. At the same time some modifications and extensions in the former part have also been introduced. These, however, refer essentially to the now existing possibility of calculating the nuclear heating rates internally from blanket parameters.

The new program structure is shown in Fig. 13. For a better understanding of this flow diagram and the explanations belonging to it (see Section 4.2) the reader should first be familiarized with the input quantities needed.

4.1. Input specifications

Card No. 1 (12I6)

MTRL material identification number (see: a))

MOD geometry option
= - 2 spherical, convex curvature
= - 1 cylindrical, convex curvature
= 0 plane
= 1 cylindrical, concave curvature
= 2 spherical, concave curvature
= 3 toroidal

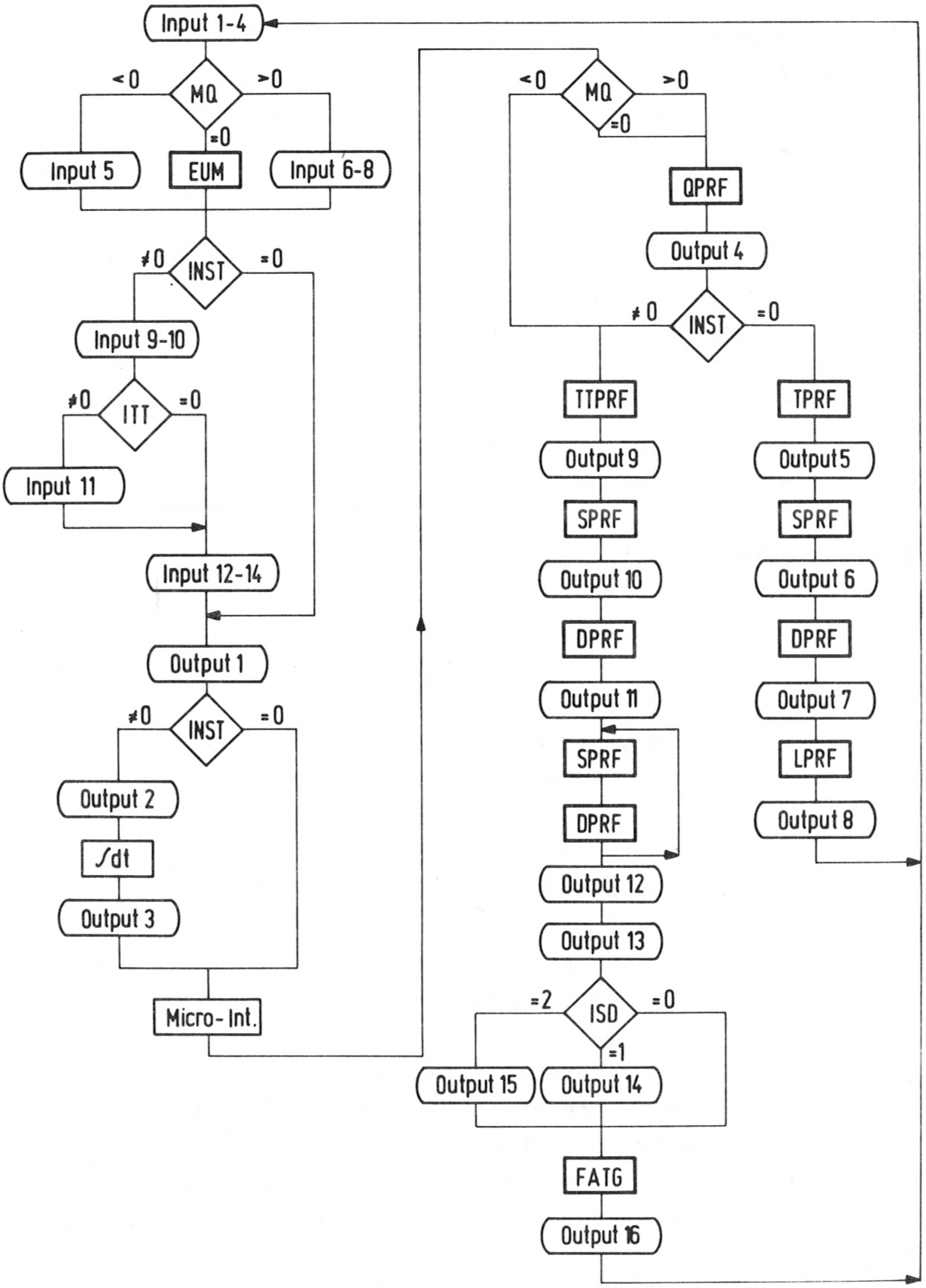

Fig. 13 Flow diagram of the computer program

MQ number of available intervals (see b))
> 0 number of macro-intervals
$= 0$ power density profile is internally generated
< 0 number of data points for power density profile. /MQ/ values are needed. Use only if INST = 1.

NP number of micro-intervals desired (see b)).
If $MQ < 0 \rightarrow NP = \lvert MQ \rvert - 1$

ISO Option for stress evaluation
= 0 axial or lateral elongation prevented
= 1 axial or lateral elongation permitted

IS1 option for thermal stress evaluation
= 0 no stresses at low temperature TO
= 1 no stresses at average wall temperature TM

IS2 option for thermal stress evaluation
= 0 E, ν, and α temperature independent
= 1 E, ν, and α temperature dependent

IS3 option for reference stress evaluation strength hypothesis to be applied is:
= 0 normal stress
= 1 maximum shear stress
= 2 octahedral shear stress

ID1 option for reference strain evaluation
= 0 reference strain is evaluated from reference stress
= 1 reference strain is evaluated using strength hypothesis defined by IS3.

INST option for calculation type
= 0 steady-state calculation
= 1 non-stationary calculation.

Card No. 2 (6E12.5)

RT	torus radius [cm]
RW	wall radius [cm]
TFW	wall thickness [cm]
TB	thickness of breeding zone [cm]
EPS	structure material volume fraction in breeding zone [-]
HD	half-thickness for radiation absorption [cm] (see c))

Card No. 3 (5E12.5)

PWN	neutron wall loading $[W/cm^2]$ (dummy, if INST = 1)
PWS	radiation wall loading $[W/cm^2]$ (dummy, if INST = 1)
TO	wall temperature at the cool side [C]
PIN	wall inside pressure [bar]
PAU	wall outside pressure [bar]

Card No. 4 (5E12.5)

RA	outer radius of cylinder or sphere in the case MOD $>$ 0 [cm] radius of circular plate for MOD = 0 [cm] (see d))
AA BB	edge lengths of rectangular plate [cm] for MOD = 0; BB $<$ AA (see d))

Card No. 5 (5E12.5)

Q	values of power density by space point $[W/cm^3]$. ($\lvert MQ \rvert$ values). Only needed if MQ $<$ 0.

Card No. 6 (5E12.5)

QN	power density by interval due to neutron reactions $[W/cm^3]$ (MQ values) only needed if MQ $>$ 0.

Card No. 7 (5E12.5)

QG	power density by interval due to gamma reactions $[W/cm^3]$ (MQ values). Only needed if MQ $>$ 0.

Card No. 8 (5E12.5)

DX	widths of intervals [cm] (MQ values). Only needed if MQ $>$ 0.

The following cards are only needed if INST = 1.

Card No. 9 (12I6)

ITT	option for the initial temperature profile = 0 constant temperature TO is used = 1 arbitrary profile specified by input
ISD	output option for time dependent stress and strain profiles = 0 only reference stress/strain is printed = 1 additionally thermal stress/strain is printed = 2 total stress/strain is printed
KT	number of time intervals per cycle
KT2	number of time instants per burn period (KT2 $\leq$ KT $+$ 1)
NFXM	maximum order of spatial Fourier expansion
NFZM	maximum order of temporal Fourier expansion
MX	number of space intervals to be printed (MX $\leq$ 10, NP = N $*$ MX with N being an integer)

Card No. 10 (5E12.5)

TC	duration of one cycle [s]
FQT	conversion factor for the QT array (see e))
FPT	conversion factor for the PT array (see e))

Card No. 11 (5E12.5)

TAN	values for initial temperature profile [C] (NP+1 values).Only needed if ITT = 1

Card No. 12 (5E12.5)

QT	time function of nuclear power density ($\leq$ KT+1 values) (see e)).

Card No. 13 (5E12.5)

PT	time function of radiation and conduction wall loading ($\leq$ KT+1 values) (see e))

Card No. 14 (5E12.5)

ZZ1	initial value of interesting time domain [s]
ZZ2	final value of interesting time domain [s]
ZZ3	time increment [s].

Comments:

a) MTRL: material identification number

According to /1/ the following numbers have been assigned:

MTRL	material specification
2601	1.4970 stainless steel = Sandvik 12R72HV
2602	1.4988 stainless steel
2603	1.4961 stainless steel
2604	1.4981 stainless steel
2605	1.4436 stainless steel
2606	1.4919 stainless steel
2607	316 SS stainless steel
2801	Incolloy 800
2802	Inconel 625
2803	Hastelloy X
2804	Inconel 718

Assignment of a material identification number does not, however, automatically mean complete availability of data. For the materials mentioned above the thermal properties (thermal conductivity, thermal expansion coefficient, density, and specific heat) as well as the principal elastic constants (Young's modulus, Poisson ratio) were compiled on the basis of the data given by K.D. Cloß /10/ and K. Ehrlich /7/. The time rupture strength, however, is at present only available for material No. 2601 /8/, data on the fatigue behaviour for material No. 2607 /11/.

b) MQ, NP: number of intervals

Because of the need for numerical integration procedures throughout the program a sufficient number of NP micro-intervals has to be defined. For each interval a certain value has to be specified for the power density. This can be done in three different ways controlled by the integer MQ. If MQ $>$ 0, the program expects to receive values for the average power density due to neutron reactions, QN(M), and that due to gamma reactions, QG(M), in a limited number, MQ, of arbitrarily sized, DX(M), macro-intervals (cards 6 to 8). If MQ = 0, the power density profile is internally generated using the information stored in the subroutine EUM for a special blanket type. Only these two possibilities can be used in the case of steady-state analysis. For non-stationary calculations a third possibility is provided, MQ $<$ 0; in this case the program expects to receive $|MQ|$ values for the power density defined at each interval boundary (card 5).

c) HD: half-thickness for radiation absorption

For non-stationary calculations (INST = 1) the definition of HD is meaningless because the solutions used always assume the radiation to be a heat flux entering the wall from outside.

d) RA, AA, BB: additional quantities describing the geometry

If MOD $>$ 0, TFW and RW and, in the case MOD = 3, additionally RT are capable of describing the geometry completely. In this case, RA, AA, and BB do not have any meaning.

If MOD $<$ 0, however, additional information is necessary to describe the relation between the entire toroid and a single module. Of the two possibilities of doing this - either the number or the sizes of modules can be fixed - the latter was chosen. RA therefore defines the outer radius of the cylinder or sphere limiting the module at the side exposed to the plasma. AA and BB do not have any meaning.

If MOD = 0, there is a possibility of deciding between the assumption of a circular or a rectangular plate of thickness TFW. If a circular plate is chosen, RA has to be set equal to the outer radius of the plate; AA and BB have to be zero. In the case of a rectangular plate AA and BB have to be set equal to the side lengths of the plate; RA has to be set equal to zero.

e) QT, PT: time functions of nuclear power density and radiation and heat conduction wall loading

These quantities specify the time variation of the nuclear power density QT(K) and the external heat load to the wall PT(K) for one complete cycle, assuming that there will be a periodic sequence of such cycles. In the present version the time intervals have to be chosen equally spaced.

Since in the case of non-stationary calculations the space dependent nuclear power density profile is generated on the basis of a neutron wall loading of 1 MW/m^2 the time function QT has to be normalized to this value. For this purpose the conversion factor FQT can be used. In the present version a value of $FQT = 2.2524 \cdot 10^{-14} \frac{MW/m^2}{n/cm^2 s}$ is used to adjust the output of the plasma model /2/ to this program.

For the same reason the conversion factor FPT is currently set at $FPT = 1.0 \cdot 10^{-7} \frac{W/cm^2}{erg/cm^2 s}$.

4.2. Program structure and operating sequence

The present version of the program consists of the main program and 20 subprograms, the names of which together with a rough characterization of their purpose are listed below.

MAIN	Input, output, control
QPRF	evaluation of power density profile
TPRF	evaluation of steady-state temperatur profile
FY FS	auxiliary programs for TPRF
SPRF	evaluation of stress profile
CY CZ	auxiliary programs for SPRF to evaluate stress coefficients for rectangular plates
DPRF	evaluation of strain profile
LPRF	evaluation of life profile based upon time rupture strength data
TTPRF	evaluation of non-stationary temperature profile
EUM	evaluation of energy multiplication factors for special blanket type
CONDIT	evaluation of heat flux potential
COND	evaluation of thermal conductivity
DENS	evaluation of density
CAP	evaluation of specific heat

ALFA	evaluation of thermal expansion coefficient
E	evaluation of Young's modulus
NUE	evaluation of Poisson's ratio
LMP	evaluation of Larsen-Miller parameter
FATG	evaluation of fatigue rupture time (cycles to failure).

4.2.1. Main program

A flow diagram of the main program is shown in Fig. 13.

The program starts by reading the input information (cards 1 to 4) which is needed for both steady-state and non-stationary calculations. Depending on the specification of MQ, if requests the values for the nuclear power density either by micro-interval (card 5) or by macro-interval (cards 6 to 8); if MQ = 0, no input is needed, the necessary information being internally generated by calling the subroutine EUM. In the case of non-stationary calculations additional input information has to be provided (cards 9 to 10 and 12 to 14). Only if ITT $\neq$ 0 has card 11 to be supplied.

After completion of the input operations, the first output list (output 1) is produced by presenting a first set of input quantities which is extended by "output 2" in the case of non-stationary program runs. Only in this case is a program step added in which time-averaged quantities of interest are evaluated. They are printed by "output 3".

The next program step is to establish the micro-interval structure. If the nuclear power density profile is not defined by micro-interval (MQ $\geqq$ 0), the subroutine QPRF is called to do this job on the basis of the macro-interval information specified by the input or based on the results of the subroutine EUM. The power density profiles are printed by "output 4". At this stage the calculation procedure is branched, depending on the type of calculation requested (INST).

In the case of steady-state calculations (INST = 0) successively the subroutines TPRF, SPRF, DPRF, and LPRF are called to evaluate the profiles of the temperature, stress, strain, and lifetime, respectively. Each calculation step is followed by a print-out (output 5 to 8).

In the case of non-stationary calculations (INST = 1) first the time and space-dependent temperature distribution is evaluated by subroutine TTPRF. To save computer time and storage, this evaluation is done for a limited number (MX+1) of space points.

The results of this evaluation are printed by "output 9". On the assumption that the pressure loads do not vary with time, the stresses and strains for this constant load are calculated next by calling the subroutines SPRF and DPRF. These steps are followed by equivalent output operations ("output 10" and "output 11"). The program now enters a DO loop inside which the stress-strain analysis is performed for every time instant specified before. The constant mechanical stresses calculated before are input to this procedure. For numerical reasons the original fine spatial subdivision is again used. In practice, this means that the coarse mesh subdivision used in TTPRF is extended to a fine mesh structure by an interpolation procedure. When the loop is completed, "output 12" and "output 13" list the time-dependent reference stresses and strains again at the coarse mesh interval boundaries. With an option (ISD) it is additionally possible to print the time variation of the three components of thermal stresses and strains ("output 14") or total stresses and strains ("output 15").

In the course of the non-stationary calculation the program checks at each space point for the maximum and minimum stresses and strains and calculates the strain ranges $\Delta\varepsilon$ at each space point. The maximum $\Delta\varepsilon$ is finally fed to the subroutine FATG, which calculates the number of "cycles to failure". Using the cycle duration TC and the time-averaged wall loading, the main program provides information about the useful life and the integrated wall loading to be expected with regard to the fatigue properties of the material considered ("output 16").

4.2.2. Some special subroutines

Most of the main subroutines used have already been briefly described in /1/. We therefore comment here only on those subprograms that are new to the system.

DPRF calculates the strain profiles. The elastic strain is evaluated from the total stress using Hooke's law, and the thermal strain from the temperatures resulting from either TPRF or TTPRF. Subsequently, the total and the reference strains are provided. As is the case for the stresses, the material properties can be treated as temperature dependent or independent. The reference strain is evaluated either from the reference stress or from the three components of the total strain using the same strength hypothesis as is used for calculating the reference stress.

TTPRF evaluates the space and time dependent temperature distribution for a periodic sequence of pulses. Both internal heat sources and heat conduction from outside are taken into account. The time function of both contributions may be arbitrary as may be the space distribution of the internal power density. The program starts with the evaluation of an average temperature by means of the subroutine TPRF. This temperature is used to calculate the thermal diffusivity and the time constant for the wall from the materials properties. Afterwards the space function of the power density and that of the initial temperature distribution are Fourier-analized.

The same is done for the time functions of internal and external heat loads. The Fourier coefficients resulting from these procedures are used to construct the solution for the heat flux potential which is finally converted to terms of temperature.

EUM is a multi-purpose subroutine providing a set of energy multiplication factors for special blanket types. In the present version the data for a blanket composed of liquid lithium in its natural isotopic composition and stainless steel are stored. Depending on the main blanket parameters (first wall radius, first wall thickness, thickness of breeding zone and structure material volume fraction in the breeding zone), a total of eight multiplication factors are calculated, which, multiplied by the energy or power of the 14 MeV neutron current incident on the wall, yield the energy or power delivered in the following regions: first wall, breeding zone, last wall, magnet shield, and magnet coil. The latter three are assumed to be invariable in thickness and material composition. The multiplication factors of the first wall, breeding zone, and last wall are added to define an equivalent factor for determining the "useful power", those of the magnet shield and coil for determining the "loss power". All factors are added to determine the "total power". The information stored in this routine is based upon systematic neutronics/photonics-calculations /12/ performed with the INDRA program system /13/.

FATG calculates the number of cycles to failure from the strain range under pulsed load conditions. At present only data for MTRL = 2607 (Type 316 SS) are available which were taken from /11/.

5. Program testing

In order to check the reliability of the program and to gain some experience of the sensitivity of the results with respect to the order of Fourier approximation some test runs were performed.

5.1. Verification of steady-state results

Already in an early stage of program development it was tested whether the results of the subroutine TTPRF are consistent with those of a steady-state calculation. Assuming a neutron wall loading of 1 MW/m^2 and no external heat load, the build-up of the temperature profile in a 1 cm stainless steel wall was investigated. The time function QT was set constant in this case. The results of this calculation are shown in Fig. 14. It can be seen from this picture that the heat flux potential S at the hot surface

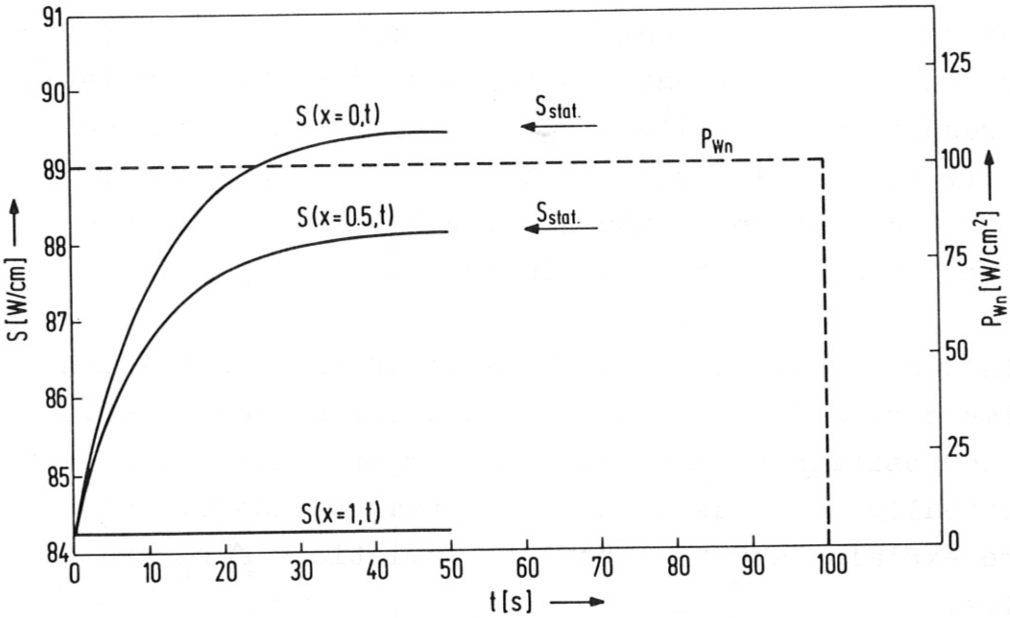

Fig. 14 Time variation of the heat flux potential S at various wall depths x for a very long burn pulse.

and in the middle of the wall approaches the values of the steady-state calculation with increasing time. After about 40 to 50 seconds, which corresponds to about 4 to 5 times the time constant of the wall, there is nearly no difference in the results (see Section 2.2.2.).

5.2. Verification of the analytical solution for $q_x(x) = q_{xo} \cos\left(\frac{\pi}{2}\frac{x}{d}\right)$; $q_t(t) = \frac{1}{2}\left[1 + \cos(\omega t)\right]$

Excluding again external heat sources to the wall, the example described in Section 2.5.3. was recalculated with the computer program. The space function $q_x(x)$ was represented by 46 power density data points defined in the micro-interval structure (MQ = - 46), and the time function $q_t(t)$ by KT2 = 61 data points for one cycle. The cycle duration τ was varied between 5 and 60 seconds. In this way the entire range of the quantity τ_d/τ is covered, the analytical results for which were presented in Fig. 9.

From the results of the subroutine TTPRF the maximum and minimum values of the heat flux potential S were extracted and the ratios r_f evaluated using equation (72). In Table III these results are compiled together with those obtained on the analytical basis using equation (77). The comparison shows that deviation of the numerical results from the analytical ones cannot be excluded.

This is due to the fact that because of the subdivision of the time domain into a number of equally spaced time intervals the position of the real maximum or minimum does not automatically coincide with an interval boundary. This feature explains why the absolute deviations Δr_f are always negative.

Table III: Comparison of analytical and numerical results for the case $q_x(x) = q_{xo} \cdot \cos\left(\frac{\pi}{2} \cdot \frac{x}{d}\right)$; $q_t(t) = \frac{1}{2}\left[1 + \cos(\omega t)\right]$.
(Time constant $\tau_d = 9.896$ s)

τ [s]	ω [s^{-1}]	τ_d/τ	r_f(anal.)	r_f(num.)	$\Delta r_f =$ r_f(num.)-r_f(anal.)	$\Delta r_f / r_f$(anal.) [%]
60	0.1047	0.1649	0.69445	0.68834	- 0.00611	- 0.88
40	0.1571	0.2474	0.54097	0.53349	- 0.00748	- 1.38
20	0.3142	0.4948	0.30616	0.29566	- 0.01050	- 3.43
10	0.6283	0.9896	0.15879	0.14444	- 0.01435	- 9.04
5	1.2566	1.9792	0.08015	0.06685	- 0.01330	- 16.60

As can be seen from Table III, the absolute deviations Δr_f are of similar magnitude. Since, however, the value of r_f decreases with increasing τ_d/τ the relative error $\Delta r_f/r_f$ increases. In the range of cycle durations τ of interest for fusion reactor operation, which should be in the range of $\gtrsim 60$ seconds, the relative error of about 1 % should be acceptable. In the case of higher time constants than assumed for this special calculation the choice of smaller time intervals can maintain the accuracy at similar values.

5.3. Influence of the order of Fourier expansion

The application of the Fourier solution to the problem of non-stationary heat conduction makes it necessary to investigate which order of Fourier expansion will be reasonable to arrive at satisfactory results. We have studied this problem using constant time functions for the internal power density $q_t(t)$ and for the external heat flux $Q_w(t)$ and looking at the transient behaviour of the temperature in the first few seconds of operation.

Figure 15 shows the development of the temperature profiles with time, assuming only internal heat sources (Fig. 15a) and only an external heat flux (Fig. 15b). In both cases five terms in the spatial and ten terms in the time expansion were taken into account. The picture reveals re-

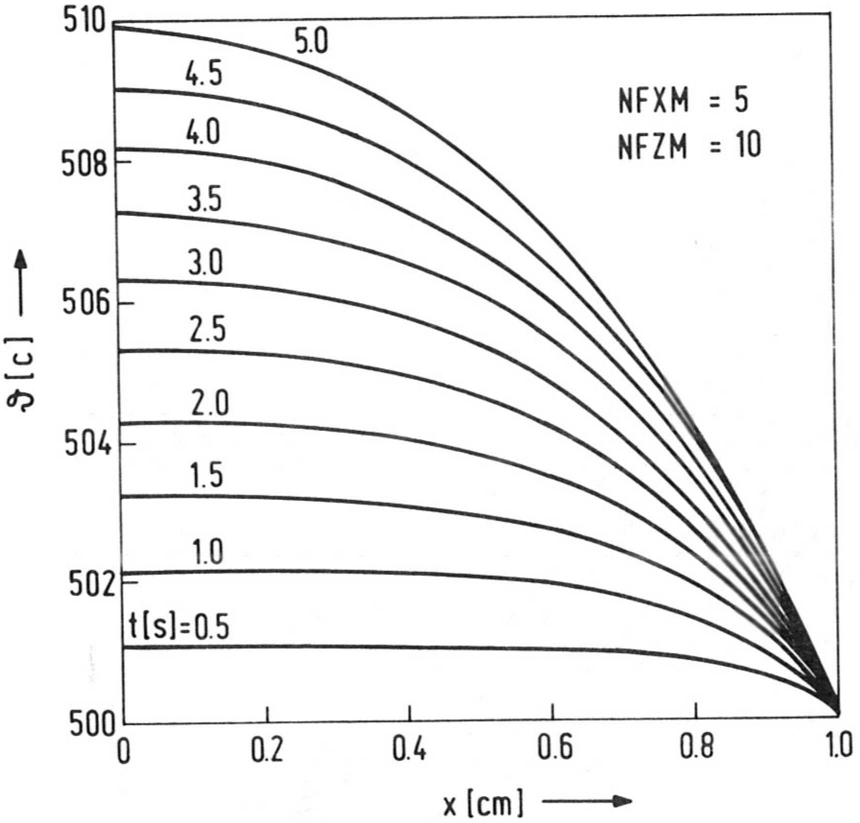

Fig. 15a) Development of temperature profiles across the wall with time due to internal heat sources

markable differences. While the temperature profiles due to internal heat sources (15a) look very smooth, rapidly approaching the parabolic shape expected, the profiles due to an external heat flux (15b), which should approach a linear shape with increasing time, still show significant spatial fluctuations. The explanation for this different behaviour must be sought in the different convergence behaviour. Since the spatial power density profile, $q_x(x)$, which is approximately a step function according to Fig. 4, is - in contrast to the external heat flux - expanded in a Fourier series, improved convergence is the consequence.

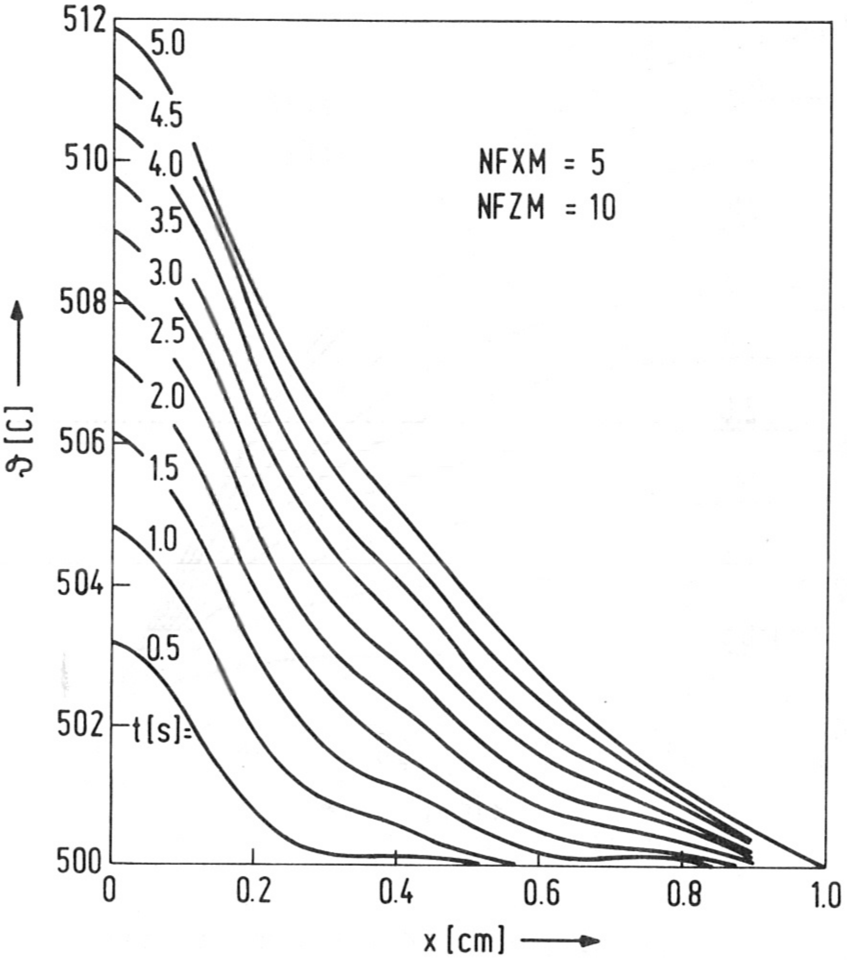

Fig. 15b) Development of temperature profiles across the wall with time due to external heat flux.

This can also be concluded by comparing equations (41) and (53).

To improve the accuracy of the temperature response to an external heat flux, we increased the order of spatial expansion to ten, while reducing the order of time expansion to five. The result is shown in Fig. 16. The temperature profiles calculated on this assumption come much closer to the behaviour expected.

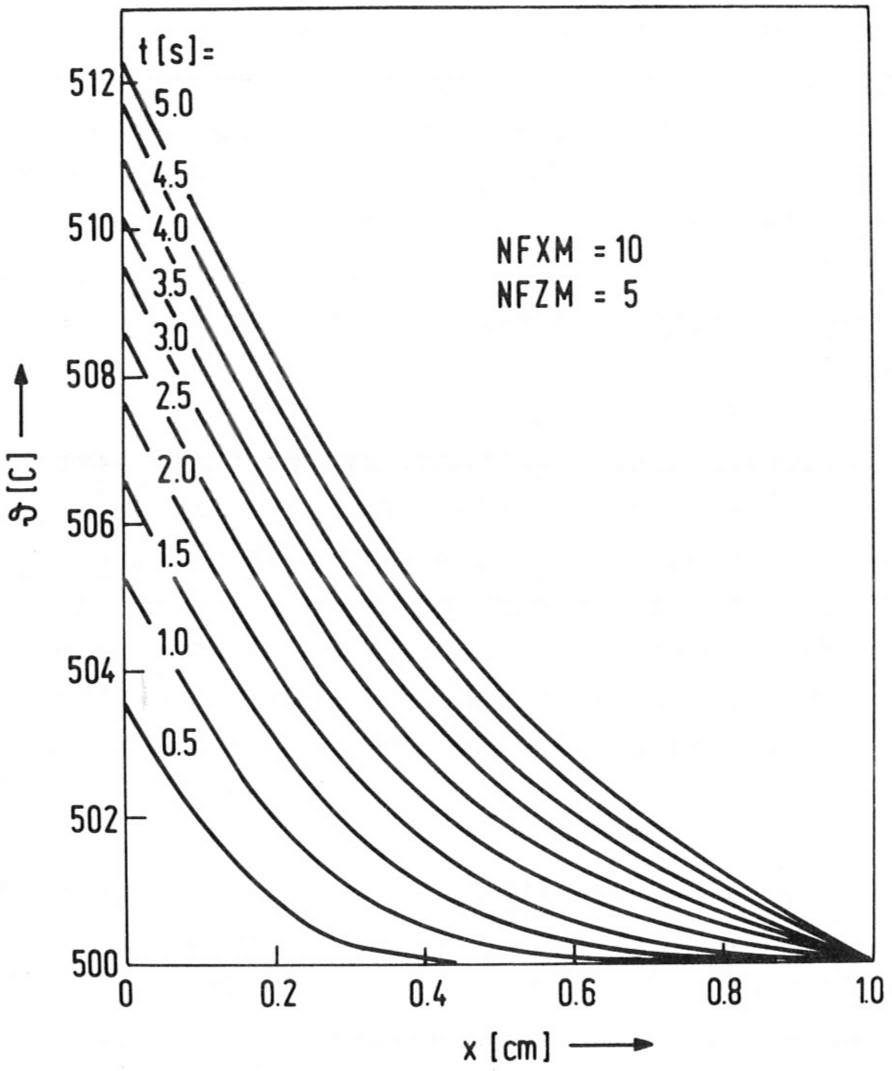

Fig. 16 Development of temperature profile across the wall with time due to external heat flux using increased order of spatial Fourier expansion.

To exclude similar difficulties in further calculations we decided to use in the subsequent program runs 10 terms for the time expansion and 20 terms for the spatial expansion.

6. Parameter studies

Having checked the program for reliability and accuracy, we applied it to a number of scoping and parameter studies, the results of which are reported in the following sections. The main purpose of these studies was to find out in what way the first wall reacts to real plasma pulses and which are the significant parameters affecting the fatigue life. No judgement is to be made concerning the absolute size of the results.

Each of the following investigations, except those performed to search for the worst combination of program options (see Section 6.2.), is based on the same real plasma pulse. It results from the zero-dimensional time-dependent model for a tokamak plasma elaborated in our laboratory /2/ which calculates inter alia the 14 MeV neutron current and the plasma radiation striking the first wall as a function of time.

In doing this, it was assumed that the plasma is contained in a toroidal vessel of 18.2 m major and 7.5 m minor radius with a magnetic field of 3.57 T on the axis. Using a safety margin of $q(a) = 3$ at the plasma boundary ($a = 7$ m), a value of $\beta_{pol} = 2$ follows from the stability criterion. In order to obtain an optimum power density in the plasma these conditions were to be maintained during the entire burn period. This was achieved by an appropriate choice of ion density and plasma heating conditions. The ion density was fixed to $n_i = 4.3 \cdot 10^{13}$ cm^{-3} and assumed to be maintained at this value by cold refuelling. At an ion temperature of $T_i = 4$ keV neutral injection is started by means of 300 keV deuterons, which deliver a total power of 200 MW to the plasma ions within the first 12 seconds of the pulse. Based on these assumptions the time behaviour of the plasma was evaluated using the boundary conditions that no divertor is present, and that both α-particles and impurity atoms emerging from a stainless steel first wall will be infinitely well confined.

The resulting 14 MeV neutron wall loading and the radiation load at the first wall are represented in Fig. 17 by solid and dashed lines, respectively. The neutron wall loading essentially follows the behaviour of the ion temperature and hence the reaction rate. The first steep increase during the heating period is followed by a slower rise, which is in keeping with the further temperature rise due to α-particle heating. With increasing impurity content of the

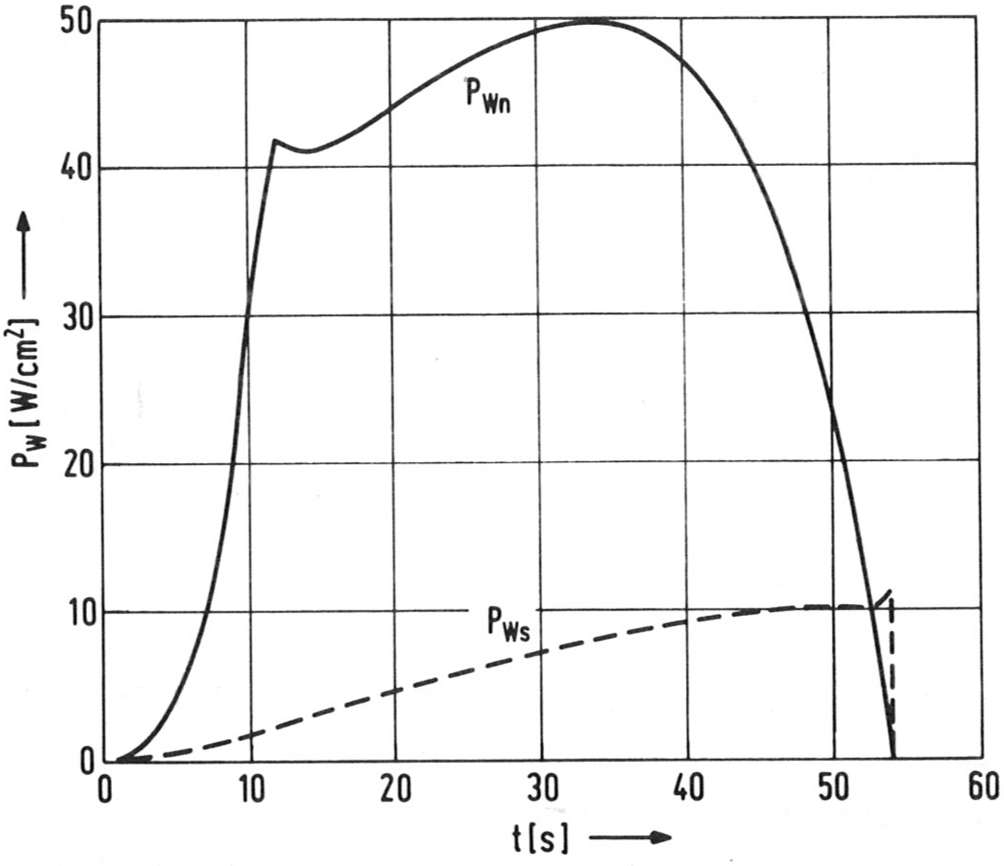

Fig. 17 Time variation of neutron wall loading P_{Wn} and radiation wall loading P_{Ws} due to a characteristic plasma burn pulse.

plasma the radiation losses increase until they finally cool the plasma to temperatures where the fusion reactions are quenched. The dashed line representing the continuous increase of the radiation losses characterizes the sum of all contributions to the plasma radiation, i.e. bremsstrahlung, cyclotron, line, and recombination radiation.

As can be concluded from Fig. 17 a total burn time of τ_B = 54 s follows for this special case. The total energy gained from the plasma during a single pulse amounts to about 120 GJ. Averaged over the burn phase, this corresponds to a total power of about 2200 MW. The average neutron wall loading is approximately 0.35 MW/m^2, and the radiation wall loading about 0.07 MW/m^2. For our further considerations that thermal power is of interest which has to pass the first wall to its cooling side. Averaged over the burning phase, this is a total of 530 MW, 335 MW being radiation power and only 195 MW being nuclear heating inside the 1 cm thick first wall.

6.1. Influence of the pulse shape on temperature variations

In a first series of calculations we wanted to find an answer to the question to what extent the temperature variations of the first wall are affected by simplifying assumptions about the pulse shape. The time dependence of the real radiation load shown in Fig. 17, for instance, suggests using a linear increase with time. The neutron wall loading, on the other hand, can be approximated by a linear increase during the heating phase up to a maximum value which is subsequently maintained up to the end of the burn phase.

We have evaluated the temperature variations for these two possibilities separately and together, assuming that the total power delivered during a single pulse equals that of the real pulse. The results for the hot surface of the wall are presented in Figs. 18 to 20.

Figure 18 shows at the top the temperature variations due to the real pulse, and at the bottom those due to the simplified pulse, both for just the nuclear heating contribution. Although small in size, the temperature fluctuations show notable differences. The real pulse produces a more sinusoidal temperature variation than the modified one. This is obviously due to the fact that, in the case of the simplified pulse, power at the "maximum" level is produced over a longer period of time and especially in the last few seconds of the pulse. Since in the case of the real pulse the maximum power is absolutely higher than in the case of the simplified one, the amplitude of the temperature variation is also larger. The difference is a factor of about 2.

Figure 19 **shows** the results for the case that only radiation power has to pass the wall. Because of the closer approximation of the real pulse shape by the simplifying assumption than was the case for the nuclear heating the deviations in the temperature response are smaller. In fact, a slightly steeper slope towards the end of the burn phase can be detected in the case of the simplified pulse.

Figure 20, finally, shows the results for simultaneous impact of both contributions. The characteristic difference is here the slower approach to the maximum temperature in the case of the real pulses as compared with the steep gradient in the case of the simplified ones.

In summary, it can be concluded that the assumption of simplified pulse shapes in the sense outlined above leads to slightly more unfavourable results.

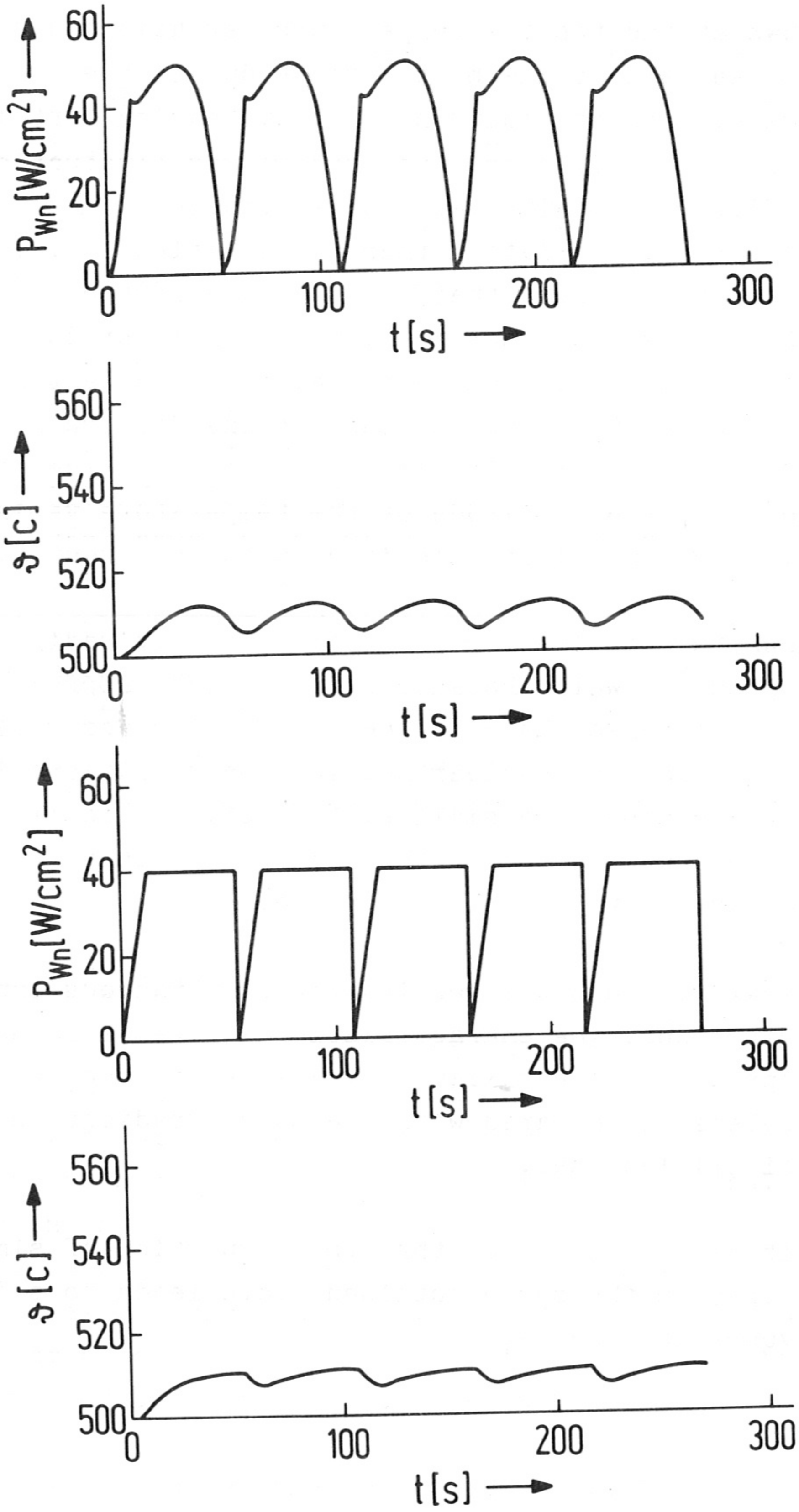

Fig. 18 Time variation of the plasma side wall temperature due to a real (upper half) and modified (lower half) pulse sequence for the neutron wall loading.

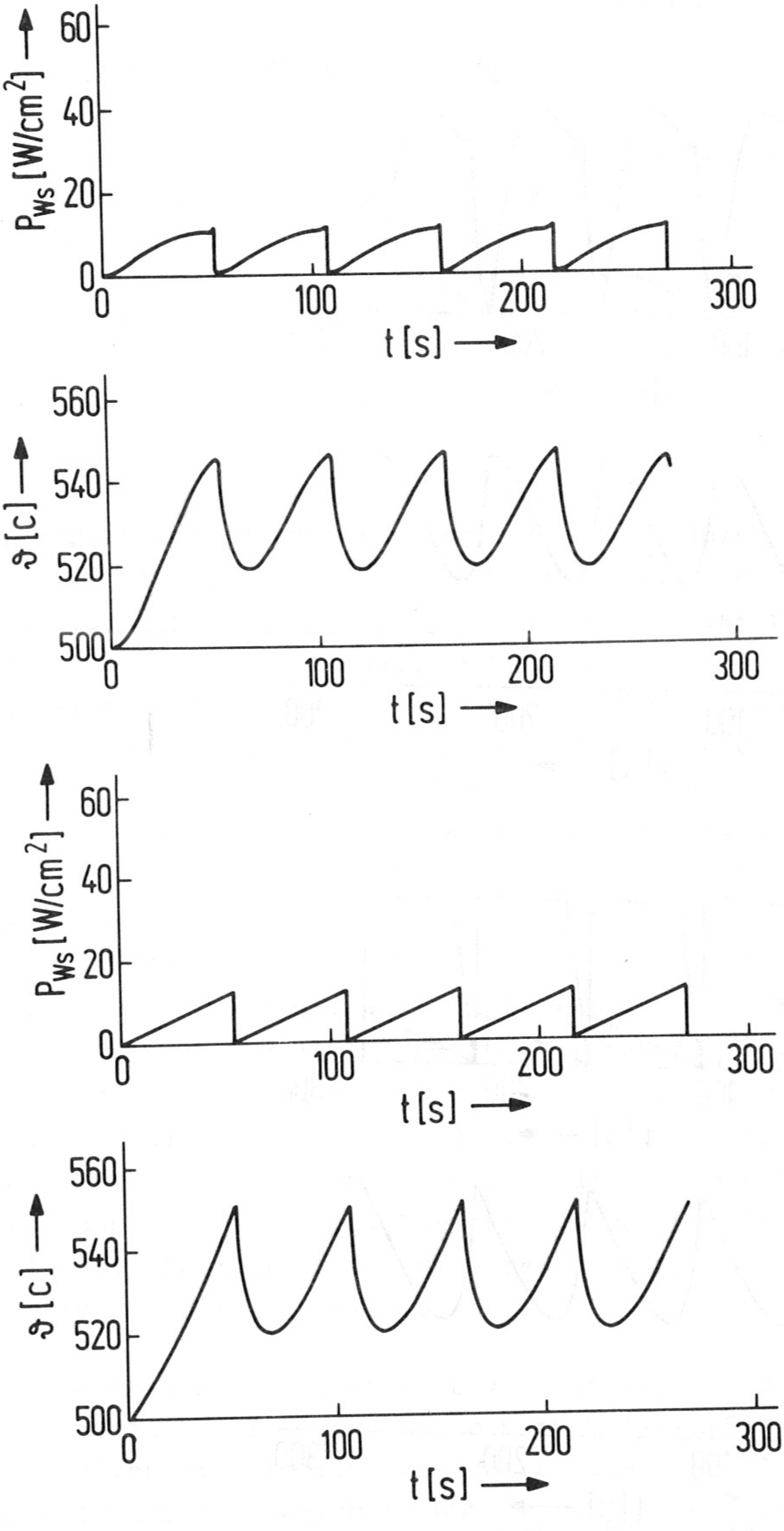

Fig. 19 Temperature variation of the plasma side wall temperature due to a real (upper half) and modified (lower half) pulse sequence for the radiation wall loading.

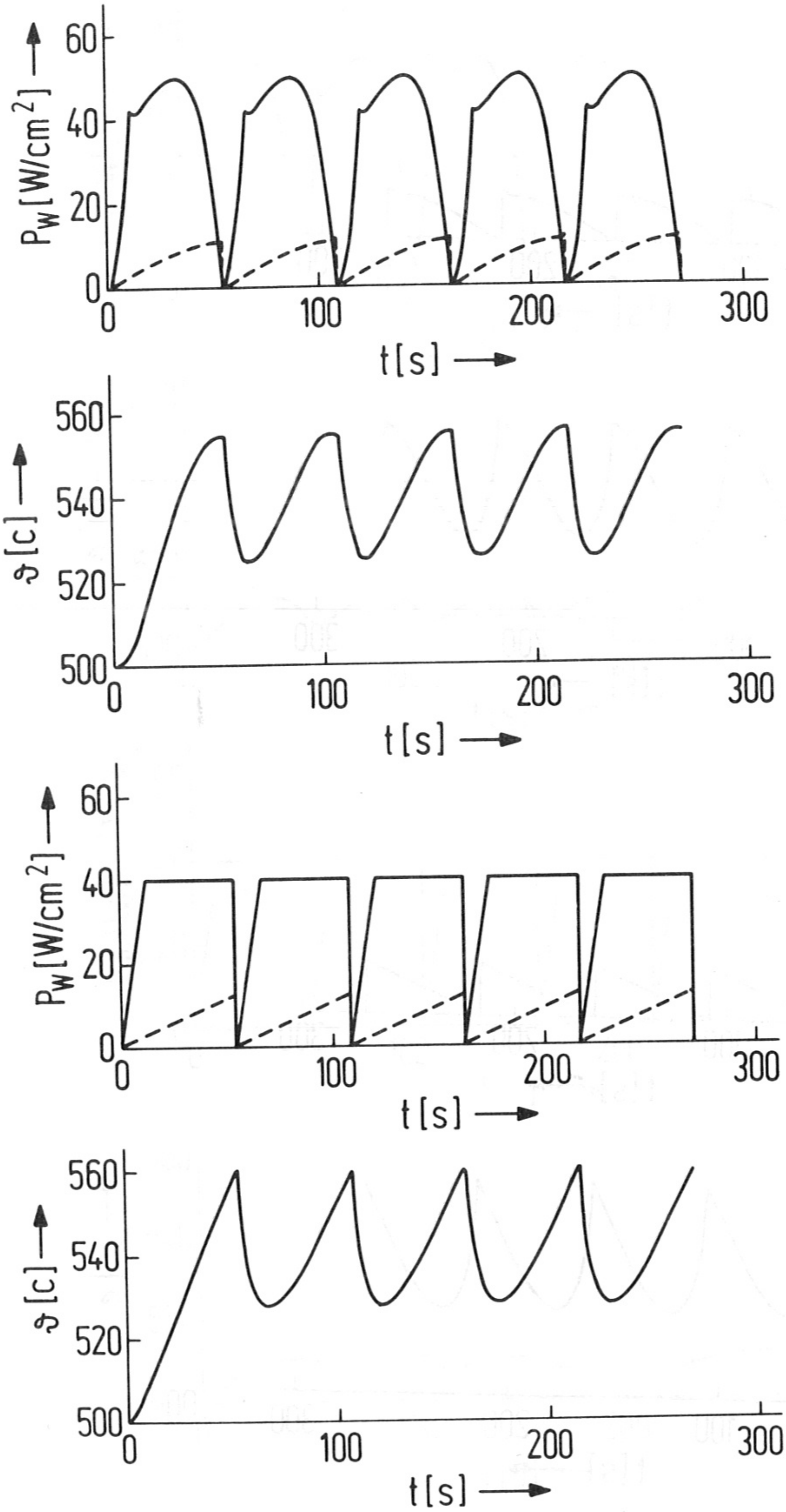

Fig. 20 Temperature variation of the plasma side wall temperature due to a real (upper half) and modified (lower half) pulse sequence for both neutron and radiation wall loading.

6.2. Choice of program options

For the determination of stresses and strains the program provides a number of options (see Section 4.1.). To arrive at a reasonable combination of the different possibilities for the subsequent parameter studies, we have systematically used the different options and assessed their usefulness with regard to those results significant for the fatigue behaviour.

As the reference case we have assumed that the first wall is constructed of a number of cylindrical modules having an outer radius of RA = 30 cm and a wall thickness of d = 1 cm. The cylinders are loaded by an internal pressure of PIN = 30 bar, and the wall temperature at the cool side is maintained by the coolant at TO = 500 C. The nuclear heating inside the wall corresponds to a case where the lithium breeding zone is TB = 100 cm thick and incorporates 10 % by volume (EPS = 0.1) structure material. An inconsistency of minor significance is that the nuclear heating rates were derived from calculations assuming the German type 1.4970 stainless steel, the results of the stress-strain evaluations, however, were correlated to the fatigue life properties of the AISI type 316 SS. For all calculations the modified plasma pulses defined in Fig. 20 (lower half) were used on the assumption of equality of burn time τ_B and cycle duration τ_c, this meaning that no down time exists between two consecutive pulses. The results were evaluated for a time range far from start-up, thus restricting the problem to the purely periodic behaviour.

On the assumptions stated above, the temperature at the hot side of the wall turns out to vary between 527.34 and 559.05 C. This gives rise to fluctuations of the thermal strain, $\Delta \varepsilon_{th}$ at this location which amount to $3.85 \cdot 10^{-4}$ in the case that the wall is assumed to be free of stress at the average wall temperature. If the stress-free state is assumed to occur at the temperature of the cold side, the thermal strain range increases to about $5.50 \cdot 10^{-4}$.

Assuming the elastic constants to be temperature dependent (IS2 = 1), we varied the restrain condition (IS0), the temperature at which absence of thermal stresses is assumed (IS1), the kind of strength hypothesis applied (IS3), and the procedure for deriving the reference strain (ID1). From the results of these calculations summarized in Tables IV to VI some interesting conclusions can be made:

If the "normal stress hypothesis" (IS3 = 0) is applied (see Table IV), the reference stresses σ_v at the hot surface of the wall turn out to be strikingly small. This is due to the fact that compressive stresses which occur at this location are not taken into account by this hypothesis. As a consequence the reference strains ϵ_v and the strain range $\Delta\epsilon_v$ also prove to be very small if they are derived from the reference stress (ID1 = 0). This combination of options, therefore, leads to wrong conclusions for both stresses and strains. As far as the strains are concerned, values closer to reality are evaluated if we follow the recommendation of H. Neuber /14/ (see Part I of this report) in that we identify the maximum strain component as the reference value (ID1 = 1). This procedure, however, does not touch the reference stress calculation. Because of this inconsistency in the latter case we conclude that this combination of options is not suitable either to be applied to this kind of problem.

Table V shows the equivalent numbers for the case where the "simple shear stress hypothesis" (IS3 = 1) is applied. More realistic numbers for the reference stresses σ_v are evaluated which in either procedure for deriving the reference strains lead to more representative numbers for both strains and strain ranges. The more unfavourable results are achieved by calculating the strains by means of a hypothesis similar to that valid for the stresses. They

Table IV: Results of scoping studies with regard to different program options. Case 1: Application of the normal stress hypothesis (IS3 = 0)

	ID1	0				1			
	IS1	0		1		0		1	
	ISO	0	1	0	1	0	1	0	1
Hot surface	$\sigma_{v\ max}$	212.	212.	226.	226.	212.	212.	226.	226.
	$\sigma_{v\ min}$	16.	16.	-0.08	-0.08	16.	16.	-0.08	-0.08
	$\varepsilon_{v\ max}$	1.32	1.32	1.40	1.40	15.39	13.89	10.46	10.09
	$\varepsilon_{v\ min}$	0.1	0.1	≈ 0.	≈ 0.	7.33	6.38	4.95	4.59
	$\Delta\varepsilon_v$	1.22	1.22	1.41	1.41	8.06	7.50	5.51	5.50
Cold surface	$\sigma_{v\ max}$	1764.	1764.	1736.	1736.	1764.	1764.	1736.	1736.
	$\sigma_{v\ min}$	1359.	1359.	1344.	1344.	1359.	1359.	1344.	1344.
	$\varepsilon_{v\ max}$	10.82	10.82	10.65	10.65	10.01	8.60	5.14	4.79
	$\varepsilon_{v\ min}$	8.34	8.34	8.24	8.24	7.73	6.81	5.13	4.78
	$\Delta\varepsilon_v$	2.49	2.49	2.40	2.40	2.29	1.79	0.01	0.01
	$\Delta\varepsilon_{v\ max}$	2.66	2.66	2.64	2.64	8.06	7.50	5.51	5.50
	CTF	1.23 (11)*	1.23 (11)	1.32 (11)	1.32 (11)	5.90 (6)	9.33 (6)	1.55 (8)	1.57 (8)
	t_L	210000	210000	226500	226500	10	16	266	269
	Q_W	74200	74200	80000	80000	3.57	5.65	93.9	95.2

σ_v in $[\mathrm{kp/cm^2}]$

ε_v, $\Delta\varepsilon_v$ in 10^4 $[-]$

CTF = number of cycles to failure

t_L = lifetime $[a]$

Q_W = integrated wall load $[\mathrm{MWa/m^2}]$

* (n) means 10^n

Table V: Results of scoping studies with regard to different program options. Case 2: Application of the shear stress hypothesis (IS3 = 1)

	ID1	0				1			
	IS1	0		1		0		1	
	ISO	0	1	0	1	0	1	0	1
Hot surface	$\sigma_{v\,max}$	1881.	1117.	1282.	1094.	1881.	1117.	1282.	1094.
	$\sigma_{v\,min}$	920.	416.	626.	436.	920.	416.	626.	436.
	$\varepsilon_{v\,max}$	11.89	7.06	8.10	6.91	15.54	10.36	10.59	9.31
	$\varepsilon_{v\,min}$	5.73	2.59	3.90	2.71	7.44	4.12	5.06	3.79
	$\Delta\varepsilon_v$	6.16	4.46	4.20	4.20	8.10	6.24	5.53	5.52
Cold surface	$\sigma_{v\,max}$	1824.	1824.	1766.	1766.	1824.	1824.	1766.	1766.
	$\sigma_{v\,min}$	1405.	1405.	1374.	1374.	1405.	1405.	1374.	1374.
	$\varepsilon_{v\,max}$	11.19	11.19	10.84	10.84	13.50	13.17	12.02	11.94
	$\varepsilon_{v\,min}$	8.62	8.62	8.43	8.43	10.40	10.19	9.62	9.54
	$\Delta\varepsilon_v$	2.57	2.57	2.40	2.40	3.10	2.98	2.40	2.40
	$\Delta\varepsilon_{v\,max}$	6.16	4.46	4.20	4.20	8.10	6.24	5.53	5.52
	CTF	5.55 (7)*	1.07 (9)	1.87 (9)	1.87 (9)	5.71 (6)	4.91 (7)	1.50 (8)	1.51 (8)
	t_L	95	1833	3200	3200	9.77	84.	257.	259.
	Q_W	33.6	648	1132	1132	3.45	29.7	90.8	91.6

σ_v in $[kp/cm^2]$

$\varepsilon_v, \Delta\varepsilon_v$ in 10^4 [-]

CTF = number of cycles to failure

t_L = lifetime [a]

Q_W = integrated wall load $[MWa/m^2]$

* (n) means 10^n

Table VI: Results of scoping studies with regard to different program options. Case 3: Application of the octahedral shear stress hypothesis (IS3 = 2)

	ID1	0				1			
	IS1	0		1		0		1	
	IS0	0	1	0	1	0	1	0	1
Hot surface	σ_v max	1646.	979.	1110.	954.	1646.	979.	1110.	954.
	σ_v min	843.	365.	550.	378.	843.	365.	550.	378.
	ε_v max	10.40	6.19	7.02	6.03	10.40	6.19	7.02	6.03
	ε_v min	5.24	2.27	3.42	2.35	5.24	2.27	3.42	2.35
	$\Delta\varepsilon_v$	5.15	3.91	3.60	3.68	5.15	3.91	3.60	3.68
Cold surface	σ_v max	1618.	1633.	1547.	1585.	1618.	1633.	1547.	1585.
	σ_v min	1248.	1237.	1191.	1210.	1248.	1237.	1191.	1210.
	ε_v max	9.93	10.02	9.49	9.73	9.93	10.02	9.49	9.73
	ε_v min	7.66	7.59	7.30	7.43	7.66	7.59	7.30	7.43
	$\Delta\varepsilon_v$	2.27	2.43	2.18	2.30	2.27	2.43	2.18	2.30
	$\Delta\varepsilon_v$ max	5.15	3.91	3.60	3.68	5.15	3.91	3.60	3.68
	CTF	2.85 (8)*	3.58 (9)	7.82 (9)	6.36 (9)	2.85 (8)	3.58 (9)	7.82 (9)	6.36 (9)
	t_L	489	6126	13400	10890	489	6126	13400	10890
	Q_W	173	2165	4735	3850	173	2165	4735	3850

σ_v in $[\mathrm{kp/cm^2}]$

$\varepsilon_v, \Delta\varepsilon_v$ in 10^4 [-]

CTF = number of cycles to failure

t_L = lifetime [a]

Q_W = integrated wall load $[\mathrm{MWa/m^2}]$

* (n) means 10^n

are rather close to those derived by the same procedure (ID1 = 1), but based on the "normal stress hypothesis", as long as the cylinder is assumed to be axially clamped. In comparing the maximum strain ranges $\Delta\varepsilon_{v\ max}$ occurring in the wall with the results obtained by applying the octahedral shear stress hypothesis we see that the "simple shear stress hypothesis", in general, yields the less favourable results. Its application would therefore mean being on the safe side.

In spite of this fact, however, we prefer using the octahedral shear stress hypothesis (IS3 = 2) because it is agreed in the literature that it yields the more representative values for the reference stress than does the simple one. Furthermore, no differences become obvious in the results for the reference strains depending on the procedure of evaluating them (see Table VI). The two methods provided are completely equivalent, which can be shown analytically, too. This is, in general, not true of the "simple shear stress hypothesis".

Of the four cases considered in each series of calculations the most unfavourable one with respect to fatigue life proves to be that in which the cylinder is not permitted to expand axially, and in which the temperature of the cold surface is assumed to be that at which the cylinder is free of thermal stress. In each case the maximum strain range $\Delta\varepsilon_{v\ max_4}$ occurs at the hot side of the wall and amounts to $5.15 \cdot 10^{-4}$ in the special case considered. Based on this result the fatigue life properties of the type 316 SS indicate a number of $2.85 \cdot 10^{8}$ cycles allowed to the point where failure has to be expected. With an assumed cycle duration for these calculations of 54 seconds, the wall life due to fatigue would be about 500 years. Together with the time averaged neutron wall loading of $\overline{P}_{w_n} \approx 0.35\ \mathrm{MW/m^2}$ this corresponds to an integrated wall loading of $Q_w \approx 170\ \mathrm{MWa/m^2}$.

All calculations reported so far have assumed the elastic constants to be temperature dependent as is in fact the case. In a further series we allowed the program to use mean values averaged over the momentary temperature profile. The results are shown in Table VII. The remaining options chosen are the same as those used to obtain the results in Table VI. The comparison shows that using averaged values leads to a slight underestimation of those strain ranges which determine the useful life.

From the variety of calculations performed in this series of parameter studies we decided to use the following options for all subsequent calculations:

ISO = 0 : axial expansion of the cylinder is prevented

IS1 = 0 : no thermal stresses are present at the minimum wall temperature TO

IS2 = 1 : the elastic constants are assumed to be temperature dependent

IS3 = 2 : the octahedral shear stress hypothesis is applied to evaluate the reference stress

ID1 = 0 : the reference strain is calculated from the reference stress

Using these options and recalculating the sample problem specified above on the assumption of the real plasma pulses defined by Fig. 17 instead of the modified ones, we arrive at the results summarized in Table VIII. As already became obvious from Fig. 20, the temperature fluctuations prove to be slightly lower. As a consequence all reference stresses, thermal and reference strains, as well as the strain fluctuations decrease in magnitude, too. This finally leads to an increase in the fatigue life by a factor of about 2.

Table VII: Results of scoping studies with regard to different program options. Application of the octahedral shear stress hypothesis, neglecting the temperature dependence of elastic constants (IS2 = 0; IS3 = 2)

	ID1	0 or 1			
	IS1	0		1	
	ISO	0	1	0	1
Hot surface	$\sigma_{v\,max}$	1657.	986.	1116.	957.
	$\sigma_{v\,min}$	844.	365.	551.	378.
	$\varepsilon_{v\,max}$	10.26	6.11	6.92	5.93
	$\varepsilon_{v\,min}$	5.21	2.25	3.40	2.33
	$\Delta\varepsilon_{v}$	5.05	3.86	3.52	3.60
Cold surface	$\sigma_{v\,max}$	1621.	1635.	1547.	1586.
	$\sigma_{v\,min}$	1249.	1237.	1191.	1211.
	$\varepsilon_{v\,max}$	10.05	10.14	9.59	9.83
	$\varepsilon_{v\,min}$	7.70	7.63	7.35	7.47
	$\Delta\varepsilon_{v}$	2.34	2.51	2.24	2.36
	$\Delta\varepsilon_{v\,max}$	5.05	3.86	3.52	3.60
	CTF	3.47(8)	4.12(9)	9.49(9)	7.73(9)
	t_L	595	7050	16 250	13 250
	Q_W	210	2500	5 750	4 680

For notation see Table IV.

Table VIII: Results of scoping studies with regard to different program options. Application of the octahedral shear stress hypothesis. Calculations based on real plasma pulses

	ID1	0			
	IS1	0		1	
	ISO	0	1	0	1
Hot surface	σ_v max	1530.	875.	1015.	853.
	σ_v min	797.	364.	543.	378.
	ε_v max	9.65	5.52	6.40	5.38
	ε_v min	4.95	2.26	3.37	2.35
	$\Delta\varepsilon_v$	4.70	3.25	3.03	3.03
Cold surface	σ_v max	1569.	1580.	1498.	1535.
	σ_v min	1210.	1196.	1155.	1172.
	ε_v max	9.63	9.69	9.19	9.42
	ε_v min	7.42	7.34	7.09	7.19
	$\Delta\varepsilon_v$	2.20	2.36	2.10	2.23
	$\Delta\varepsilon_v$ max	4.70	3.25	3.03	3.03
	CTF	6.69(8)	1.95(10)	3.80(10)	3.77(10)
	t_L	1150	33 450	65 000	65 000
	Q_W	400	12 000	23 000	23 000

For notation see Table IV

6.3. The influence of down time

All calculations done so far did not assume a down time between successive burn pulses. In practice, however, fusion reactor operation will necessitate a certain time period to remove the reaction products, the impurities, and the unburnt fuel, to clean the discharge chamber and to refill it with fresh fuel before the next burn phase can be started. The time which is needed to perform all these procedures depends mainly on the performance of the vacuum system.

For the sample problem specified in the last section we varied the down time $\Delta\tau$ from zero up to 60 seconds, covering a range of numbers which seem to be reasonable as regards the vacuum system, on the one hand, and which also seems to be justifiable with regard to the decrease of the average power level, on the other hand. The results are shown in Figs. 21 to 24.

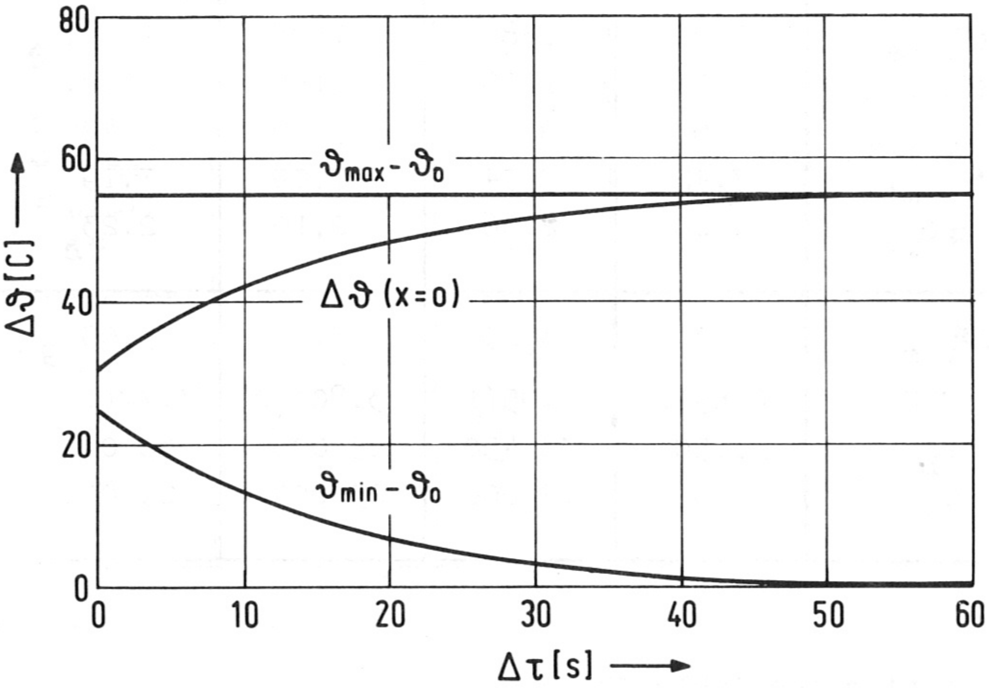

Fig. 21 Maximum and minimum temperature difference across the wall and amplitude $\Delta\vartheta$ of the plasma side wall temperature as a function of the down time $\Delta\tau$ between successive pulses.

Figure 21 shows the maximum and the minimum temperature differences across the wall ($\vartheta_{max} - \vartheta_o$ and $\vartheta_{min} - \vartheta_o$, respectively) and the amplitude $\Delta\vartheta = \vartheta_{max} - \vartheta_{min}$ of the temperature fluctuations at the hot surface as a function of the down time $\Delta\tau$. It can be seen that only the minimum temperature is affected while the maximum temperature remains unchanged. As is to be expected, the amplitude of the temperature variations increases with increasing down time, approaching the maximum temperature differences at values of $\Delta\tau$ which are equivalent to about 4 to 5 time constants of the wall.

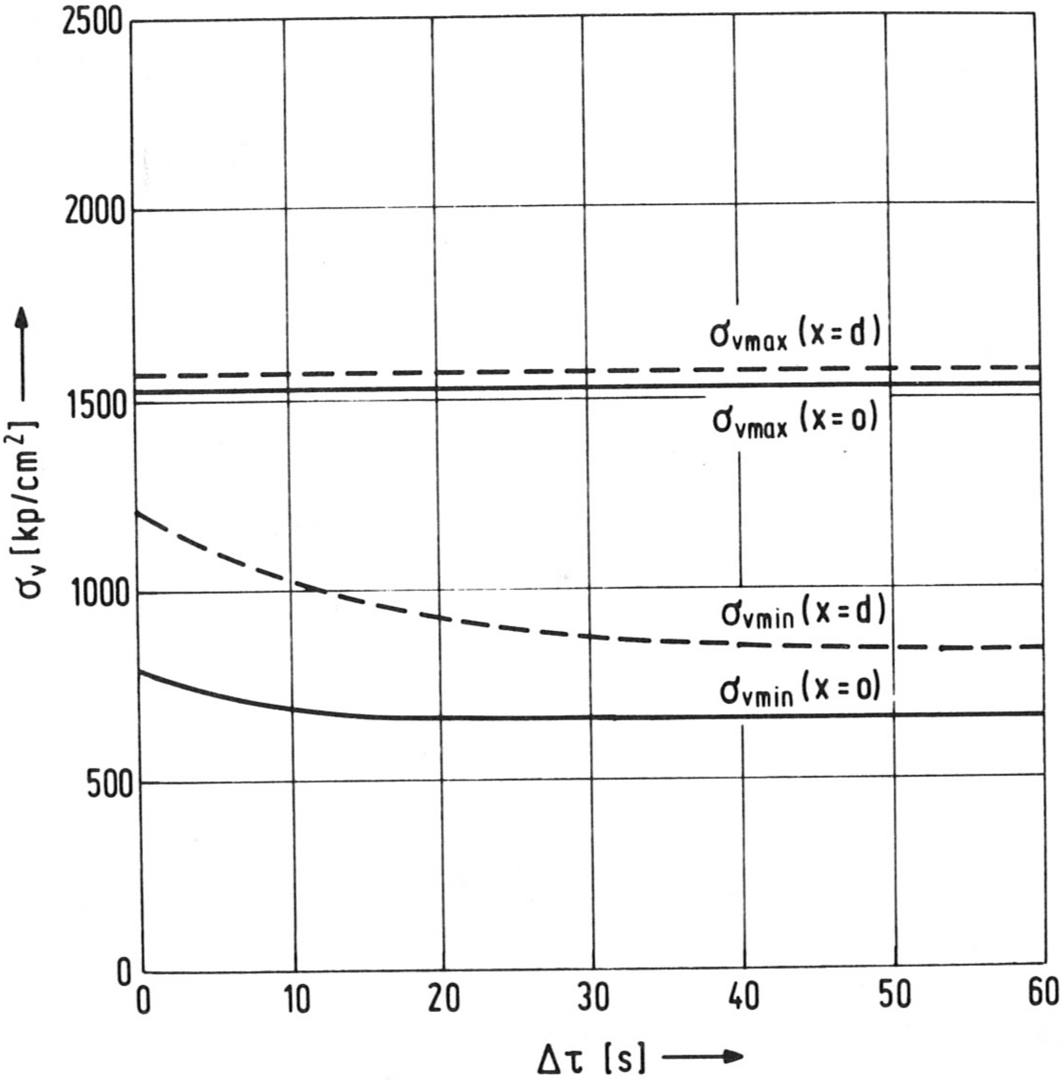

Fig. 22 Maximum and minimum reference stress σ_v at the hot (x = 0) and cold (x = d) surface of the wall as a function of the down time $\Delta\tau$ between successive pulses.

The response of the reference stresses is shown in Fig. 22. Again the maximum stresses remain unchanged, while the minimum stresses decrease slightly with increasing down time.

The more relevant quantities with respect to the fatigue life are the strain fluctuations shown in Fig. 23. Because of the feedback via the elastic response of the wall the

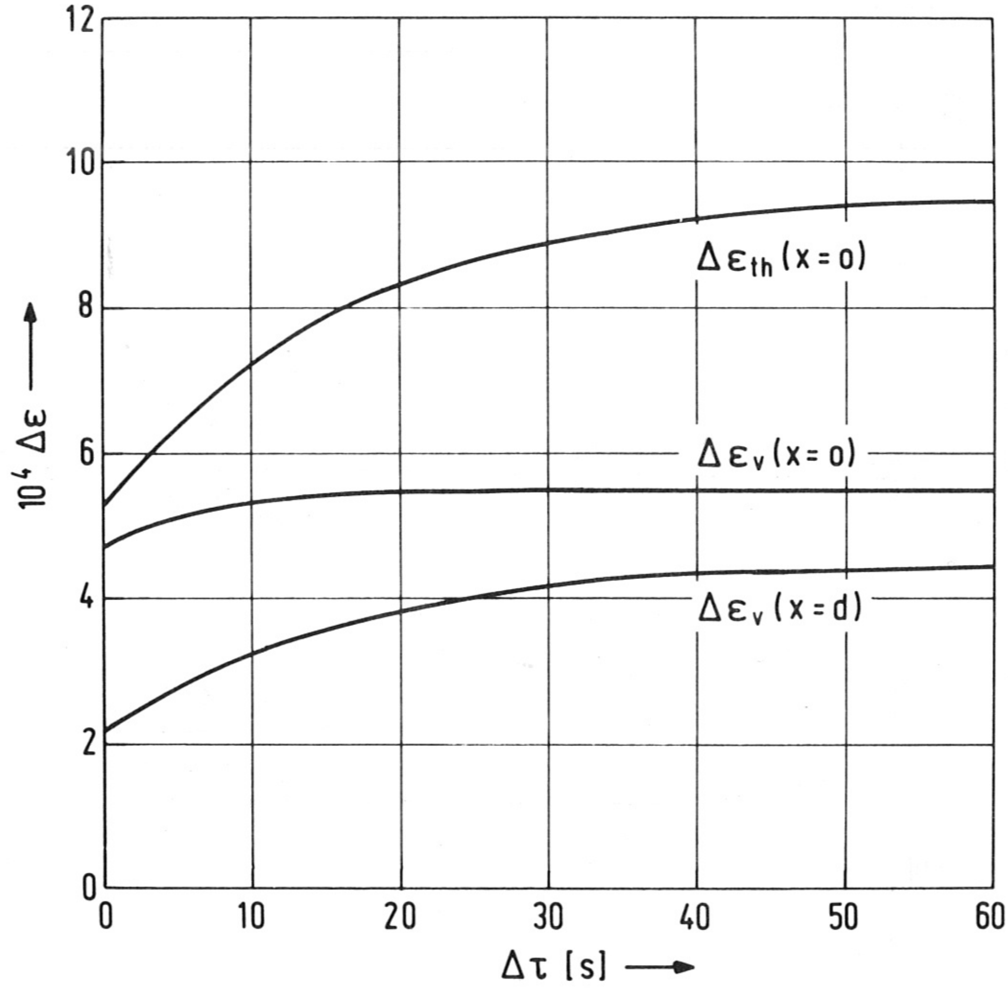

Fig. 23 Thermal strain variations $\Delta\varepsilon_{th}$ at the hot surface and reference strain variations $\Delta\varepsilon_V$ at the hot (x = 0) and cold (x = d) surface of the wall as functions of the down time $\Delta\tau$ between successive pulses.

variations of the reference strains $\Delta\varepsilon_v$ are smaller than is the variation of the thermal strain $\Delta\varepsilon_{th}(x=0)$. The reference strain variations at the hot surface, $\Delta\varepsilon_v(x=0)$, are always larger in size than those at the cold surface. Therefore, they have to be regarded as the life limiting ones.

If we correlate the strain ranges $\Delta\varepsilon_v(x=0)$ with the fatigue properties we end up with the behaviour of the lifetime t_L shown in Fig. 24. Here the logarithm of t_L (t$_L$ in units of years) is plotted versus the down time $\Delta\tau$. As can be seen from this figure, a minimum appears which is located at down times of about 10 to 20 seconds. The

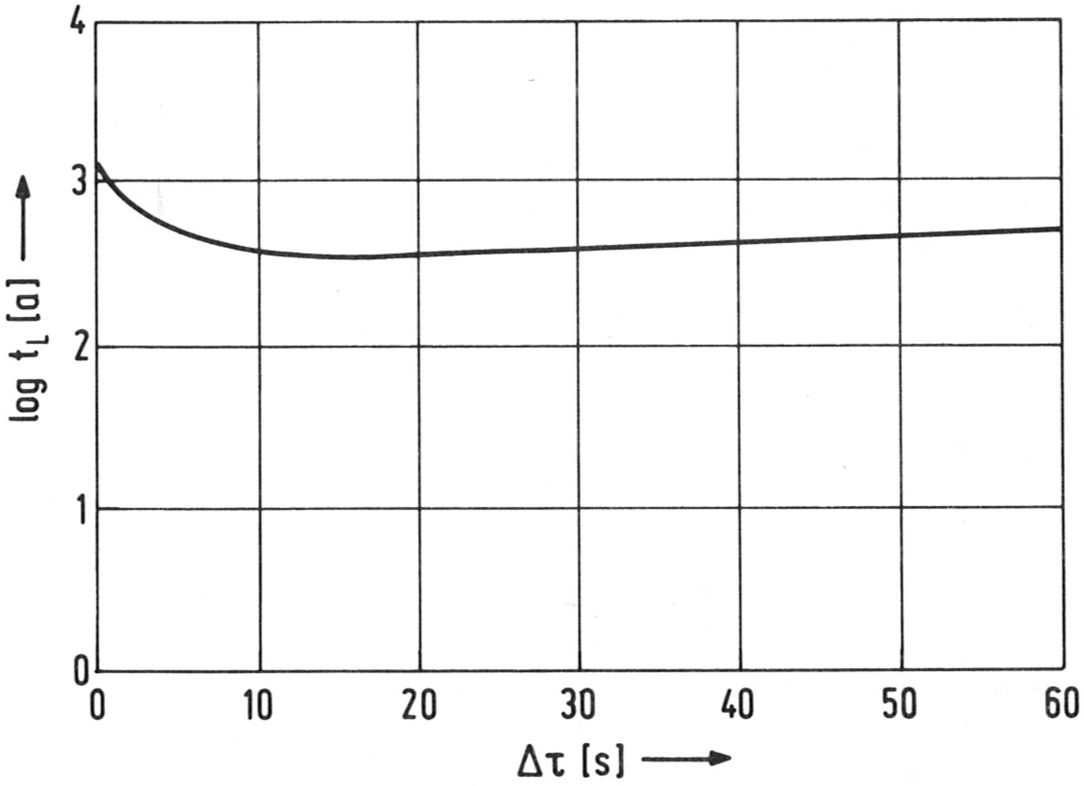

Fig. 24 Calculated fatigue life t_L [a] as a function of the down time $\Delta\tau$ between successive pulses.

slight increase at higher values of $\Delta\tau$ is due to the fact that the decrease in the absolute number of cycles to failure is more than balanced by the increase in the cycle duration τ_c if $\Delta\tau$ increases, too.

In summary, we conclude from this series of calculations that the influence of the down time upon the fatigue life of the wall is of rather moderate size. A minimum lifetime has to be expected which occurs - at least in the example considered - at down times low compared with the values assumed to be probable today. An increase in the down time, however, means at the same time a decrease in the average power output N_{th}. This decrease, in turn, means that the slight increase of lifetime observed at higher values for $\Delta\tau$ is again balanced if we look at the integrated wall loading Q_W to be achieved. As can be seen from Fig. 25, this quantity very rapidly approaches a minimum value.

6.4. The influence of temperature level

In our sample problem defined in Section 6.2. the temperature at the cold surface of the wall was specified as TO = 500 C. In this section we want to investigate to what extent the results are affected by changes in this quantity and hence in the entire temperature level. For this purpose we varied TO in the range 300 to 650 C. For the down time in this and all subsequent calculations $\Delta\tau = 30$ s was assumed. The results are summarized in Figs. 26 to 29.

From Fig. 26 we see that both the maximum and to a lesser extent also the minimum temperature differences across the wall decrease with increasing temperature. This behaviour reflects the characteristic temperature dependence of the

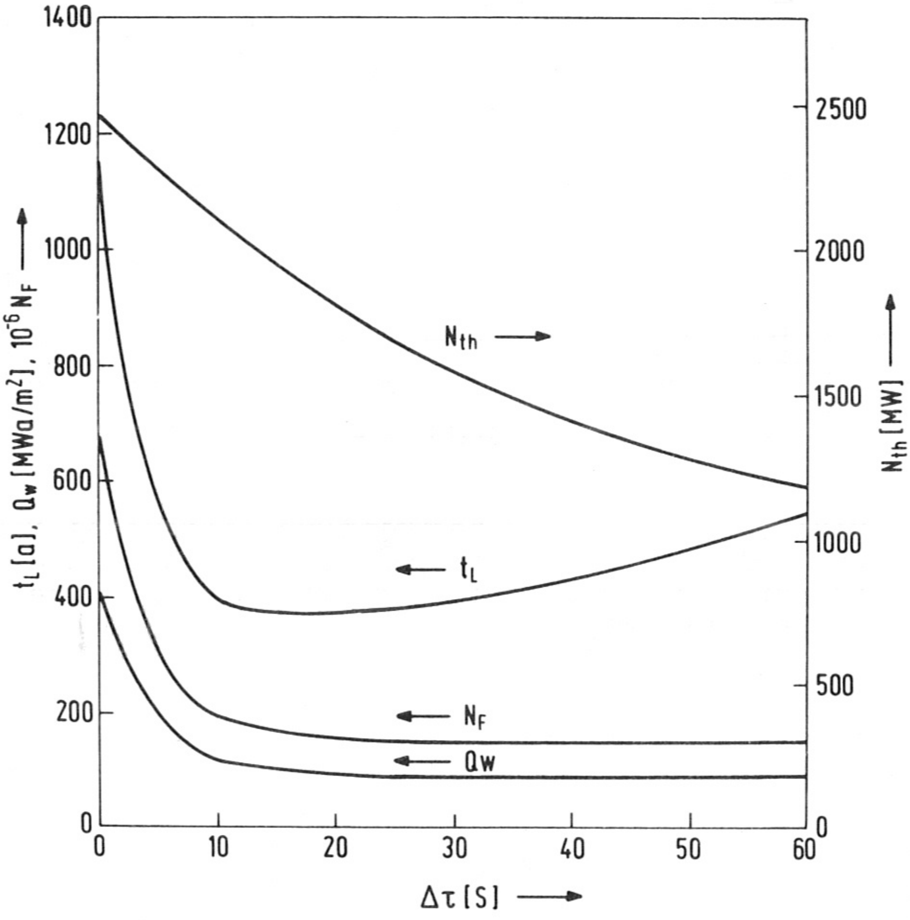

Fig. 25 Average thermal power N_{th}, number of cycles to failure N_F, fatigue life t_L, and integrated neutron wall loading Q_W as functions of the down time $\Delta\tau$ between successive pulses.

thermal conductivity, which for stainless steels like most other metals increases with increasing temperature. As a consequence the amplitude $\Delta\vartheta$ of the temperature fluctuations also decreases as do the maximum reference stresses $\sigma_{v\ max}$ (see Fig. 27) and the amplitudes of the thermal and reference strain variations $\Delta\varepsilon$ (see Fig. 28). If we apply the design curve for the fatigue life prediction

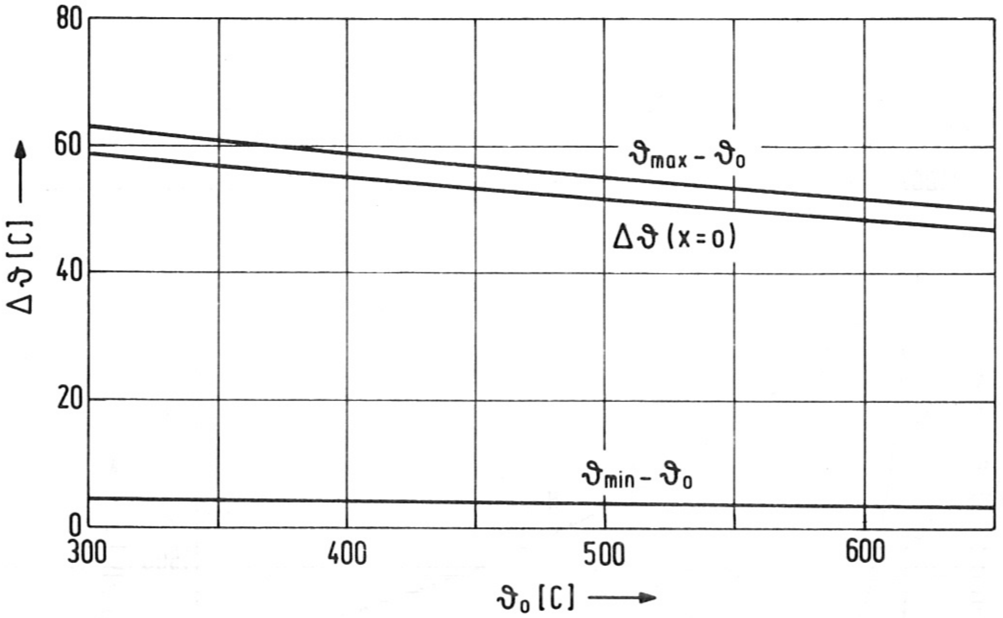

Fig. 26 Maximum and minimum temperature difference across the wall and amplitude $\Delta\vartheta$ of the plasma side wall temperature as functions of the coolant side wall temperature ϑ_o.

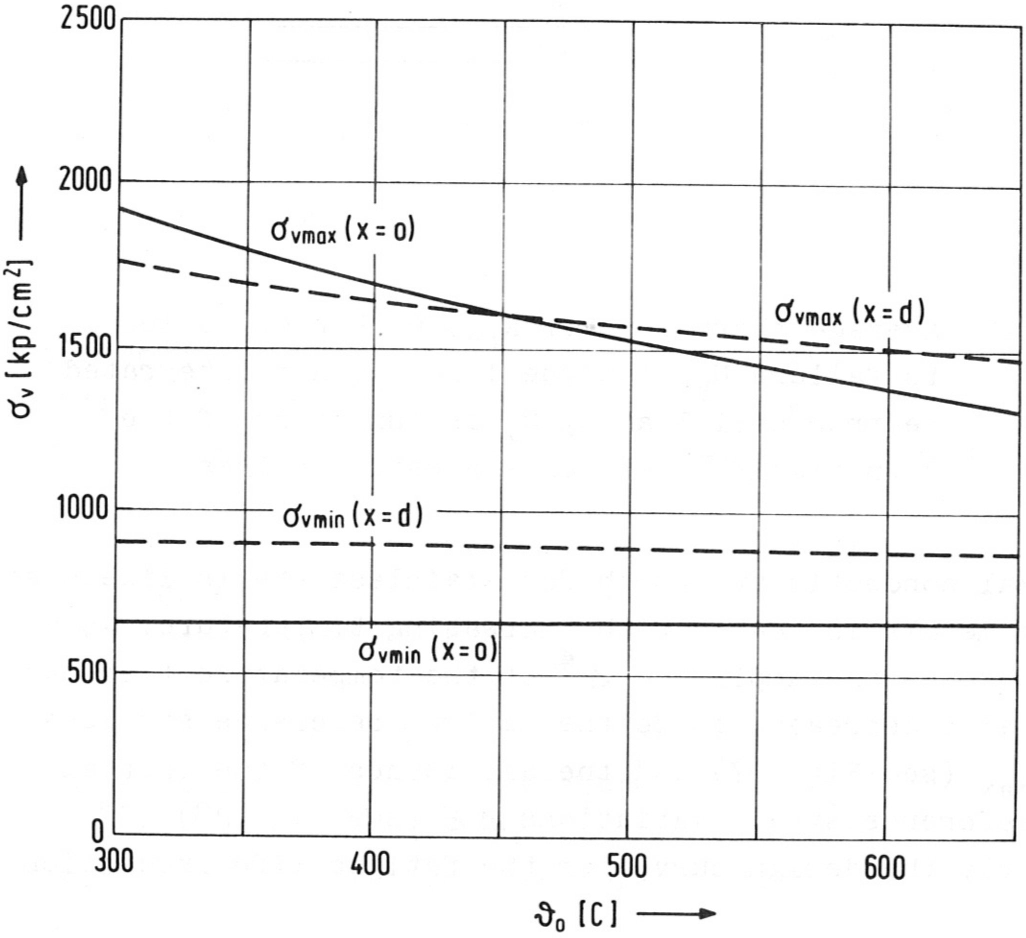

Fig. 27 Maximum and minimum reference stress σ_v at the hot (x=d)and cold (x=d) surface of the wall as a function of the coolant side wall temperature ϑ_o.

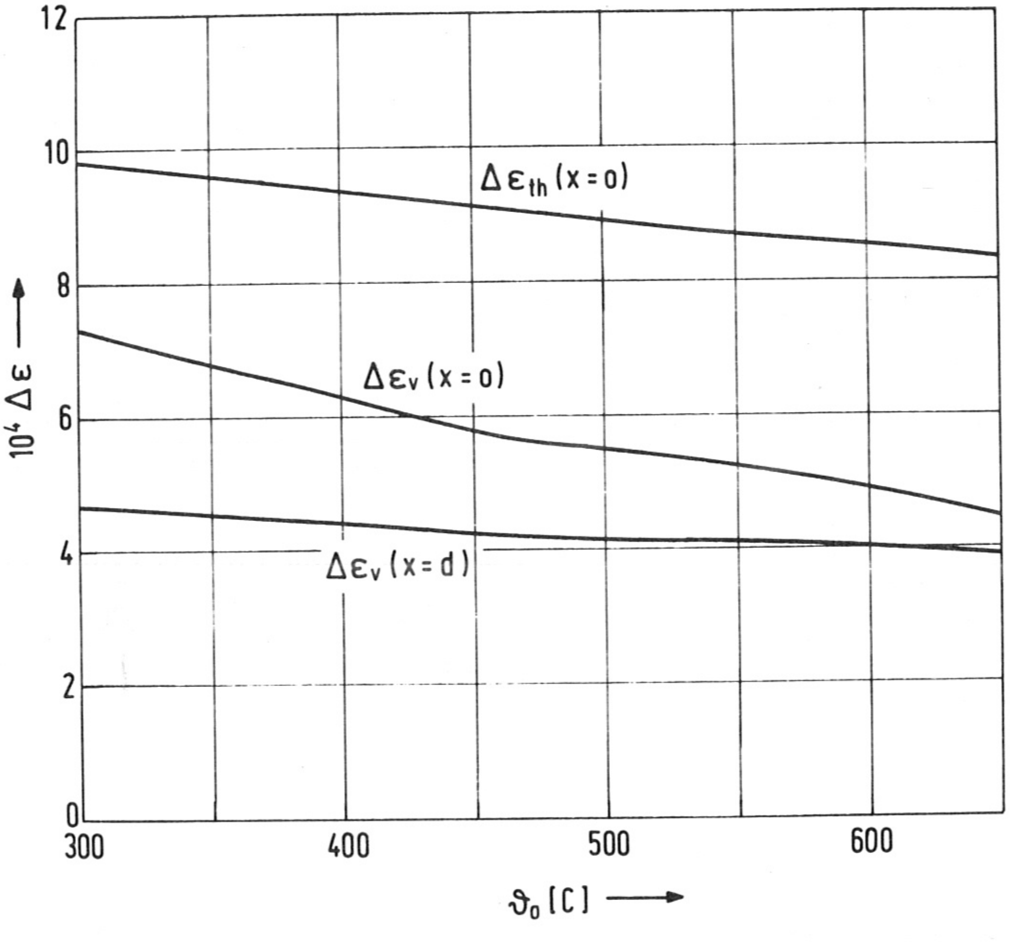

Fig. 28 Thermal strain variations $\Delta\varepsilon_{th}$ at the hot surface and reference strain variations $\Delta\varepsilon_v$ at the hot (x=0) and cold x=d) surface of the wall as functions of the coolant side wall temperature ϑ_o.

to the maximum reference strain variations, the calculations yield an increasing fatigue life with increasing temperature level (see Fig. 29).

It is, however, not correct to take this result as a conclusion. In fact, the design curve is a recommendation for application in the temperature range between 538 and

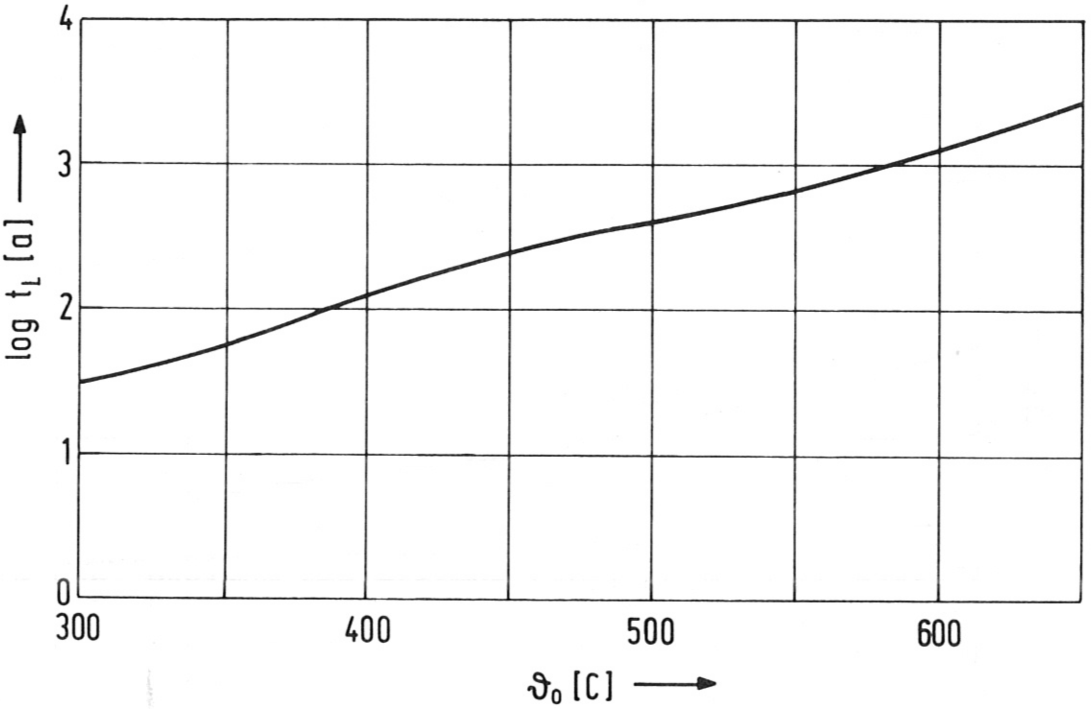

Fig. 29 Calculated fatigue life t_L [a] as a function of the coolant side wall temperature ϑ_o.

650 C, incorporating a safety factor of 2 with respect to experimental results at the higher temperature /11/. Actually, the fatigue life should increase with decreasing temperature. There is, however, at present not enough information available to take this temperature dependence into account. It seems likely that the tendency indicated by the calculational results (Fig. 29) will be just reversed if the actual temperature dependence is introduced. As another interpretation of Fig. 29 we can conclude that in the same way the predicted fatigue life is increased with increasing temperature, while the safety factor is reduced.

With regard to this inconsistency the meaning of Fig. 29 is doubtful. This is not true, however, of the other results, especially for the maximum strain variations.

6.5. The influence of wall radius

While for the reference case we fixed the wall element radius RA arbitrarily at 30 cm, we now varied it in the range between 10 and 60 cm to see the influence upon the fatigue life.

Since the time dependence of the temperature profile in the wall is calculated by means of a plane geometry model, as is done throughout this report, a different wall radius RA does not affect the results for the temperature differences and the amplitudes of the fluctuations of temperatures and thermal strains. The absolute size of these quantities therefore agrees with those of the reference case. A deviating behaviour, however, is to be expected for the reference stresses and strains because, with respect to the mechanical stresses, we use the cylindrical model for the stress evaluation.

Figure 30 shows the variation of the reference stresses with the wall radius RA. As far as the cold surface (x=d) is concerned, both maximum and minimum reference stresses essentially follow the increase of the mechanical stress which is due to the decreasing ratio of wall thickness and radius. Being tensile at this location, the thermal stresses do not significantly contribute to the total stress. The same is true of the minimum reference stress at the hot surface $\sigma_{v\ min}$ (x=0), of which low, but compressive thermal stresses are characteristic. In contrast to this behaviour, the maximum reference stress at the hot surface $\sigma_{v\ max}$ (x=0) exhibits a rather flat variation with RA, which is due to the interaction between the increasing mechanical tensile stress and the large compressive thermal stress.

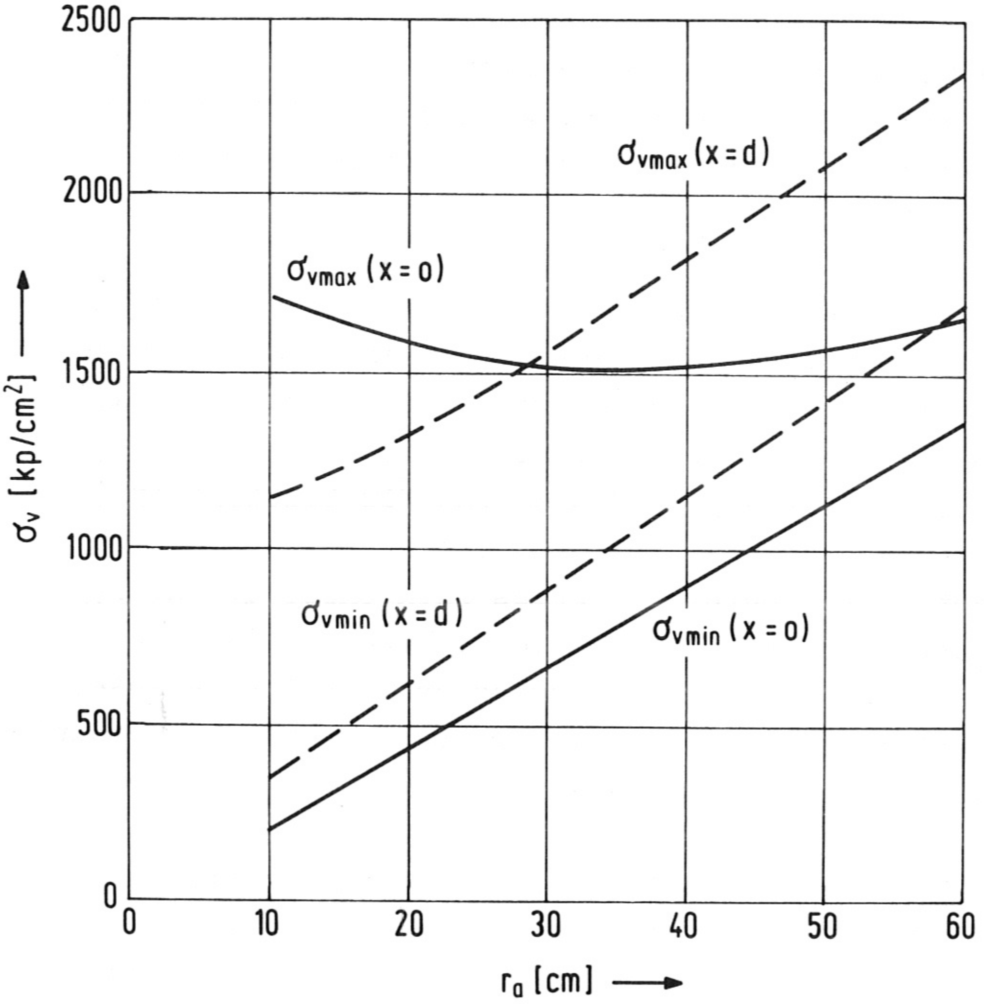

Fig. 30 Maximum and minimum reference stress σ_v at the hot (x=0) and cold (x=d) surface of the wall as a function of the cylinder radius r_a.

Fig. 31 shows the resulting behaviour of the reference strain variations $\Delta\varepsilon_v$, which is in qualitative agreement with the equivalent differences between the maximum and minimum stresses. The steeper decrease of the strain amplitudes at the hot surface $\Delta\varepsilon_v$ (x=0) as compared with those at the cold surface $\Delta\varepsilon_v$(x=d) causes the two curves to cross. This means that below a certain wall radius (in this case for RA = 40 cm)

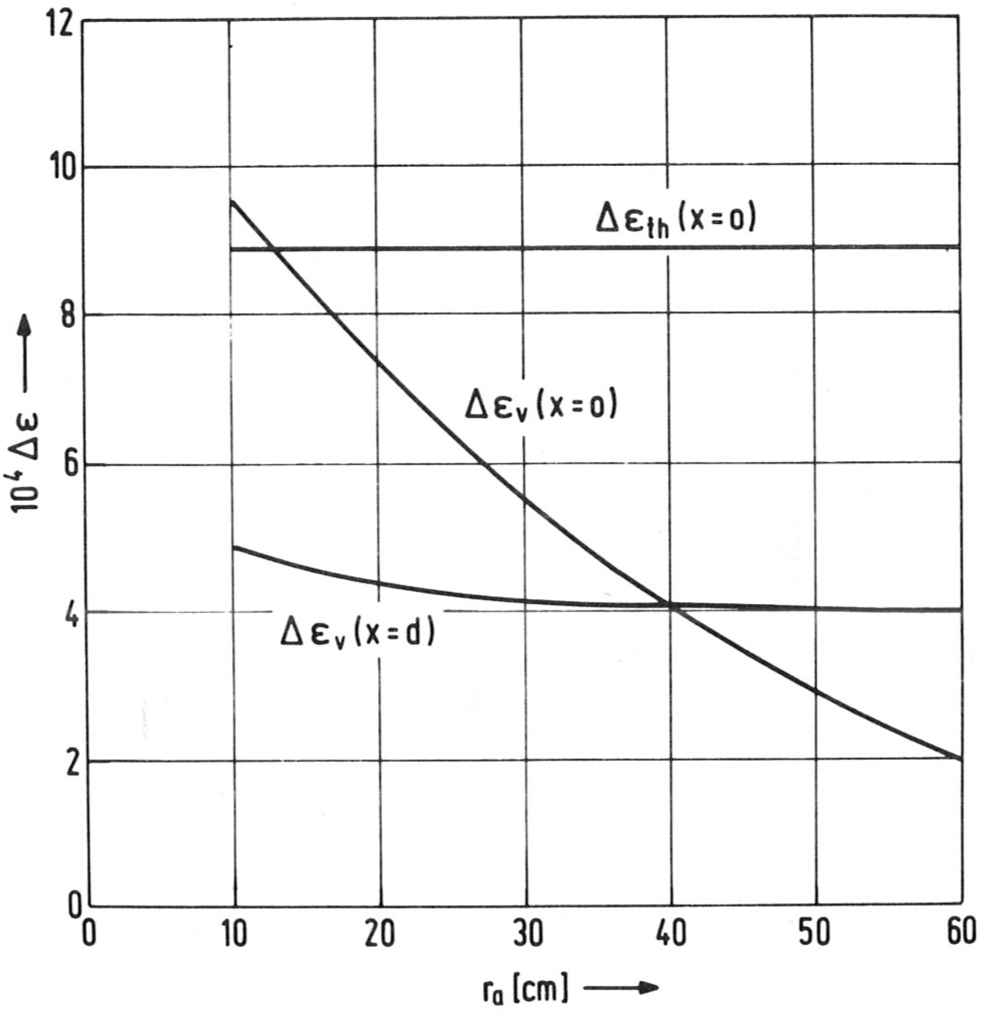

Fig. 31 Thermal strain variations $\Delta\varepsilon_{th}$ at the hot surface and reference strain variations $\Delta\varepsilon_v$ at the hot (x=0) and cold (x=d) surface of the wall as functions of the cylinder radius r_a.

the strain variations at the hot surface, above this radius, however, those at the cold surface are the life limiting ones.

The resulting dependence of the fatigue life upon the wall radius is visualized in Fig.32. As long as the hot surface is responsible for a possible fatigue failure a remarkable increase in the useful life can be expected from enlarging the wall radius. No further increase occurs if the critical surface turns to the cold side.

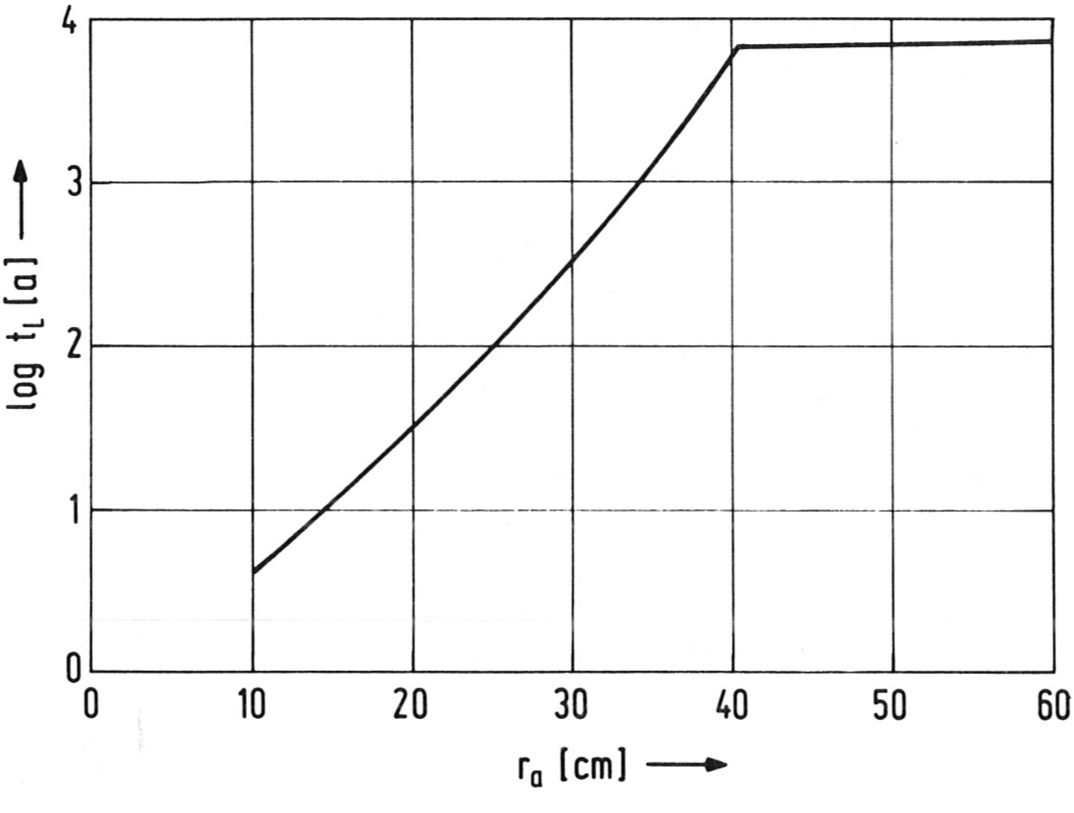

Fig. 32 Calculated fatigue life t_L [a] as a function of the cylinder radius r_a.

6.6. The influence of pressure load

A further parameter in our calculations is the pressure load of the wall, which was fixed in the reference case at PIN = 30 bar. The variation of this quantity was extended over a range from 5 to 60 bar. The results are summarized in Figs. 33 to 35.

As in the case of the variation of the wall radius, a change in the pressure load has no effect on the temperature and thermal strain fluctuations. The remaining quantities of interest, i.e. the maximum and minimum reference stresses,

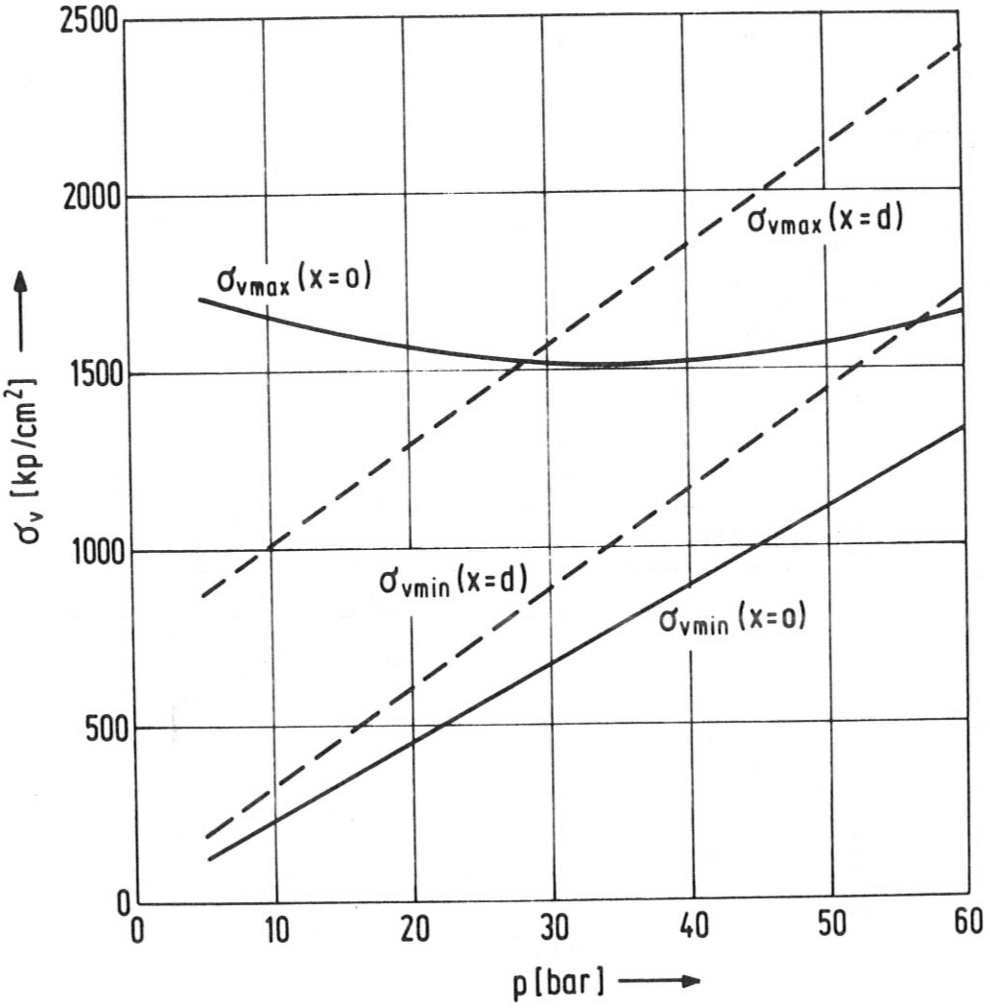

Fig. 33 Maximum and minimum reference stress σ_v at the hot (x=0) and cold (x=d) surface of the wall as a function of the internal pressure p.

the reference strain variations and the fatigue life, show, in principle, the same behaviour with increasing pressure as could be demonstrated for the case of varying the wall radius. This can easily be seen by comparing the equivalent diagrams.

In fact, this agreement is not surprising because in either case the variations in the different quantities are ultimately

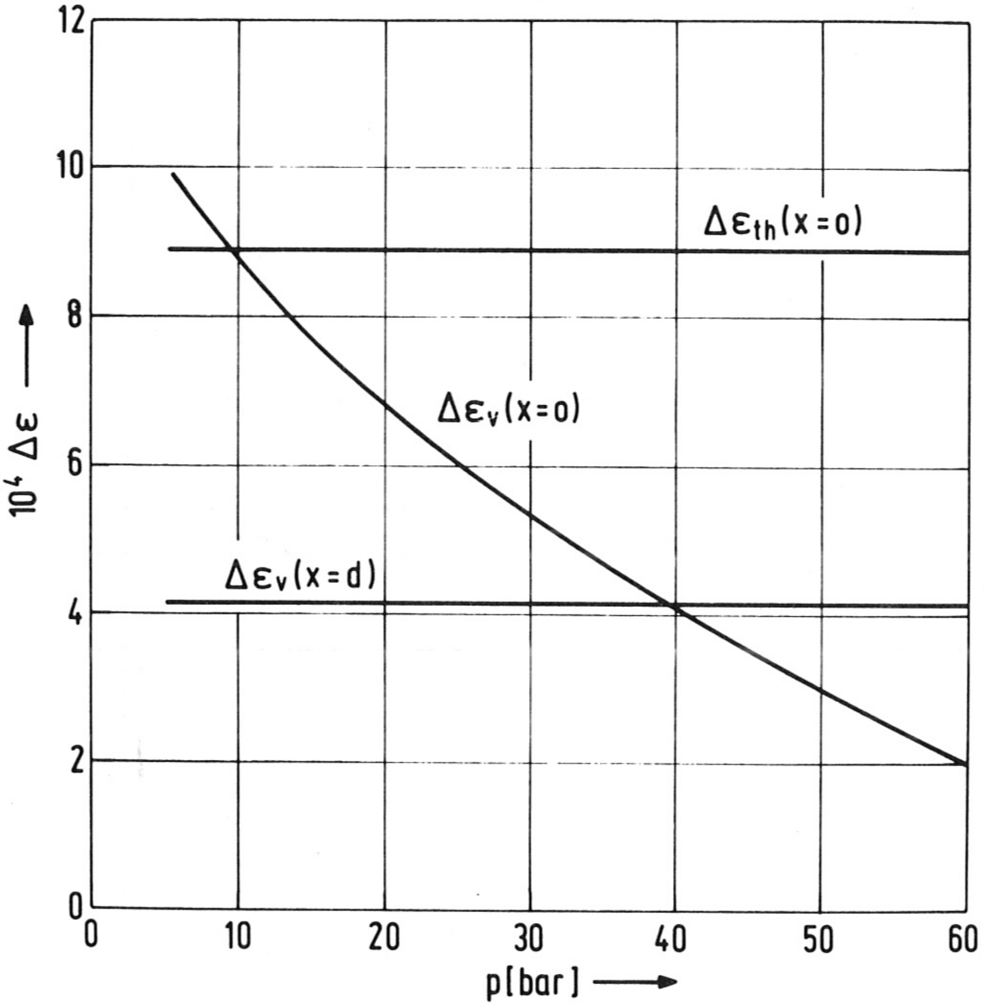

Fig. 34 Thermal strain variations $\Delta\varepsilon_{th}$ at the hot surface and reference strain variations $\Delta\varepsilon_v$ at the hot (x=0) and cold (x=d) surface of the wall as functions of the internal pressure p.

due to the variation of mechanical stresses and, as far as the hot surface of the wall is concerned, to their interaction with the thermal stress. Thus, Figs. 33 to 35 need not be considered further; they are interpreted in detail like Figs. 30 to 32.

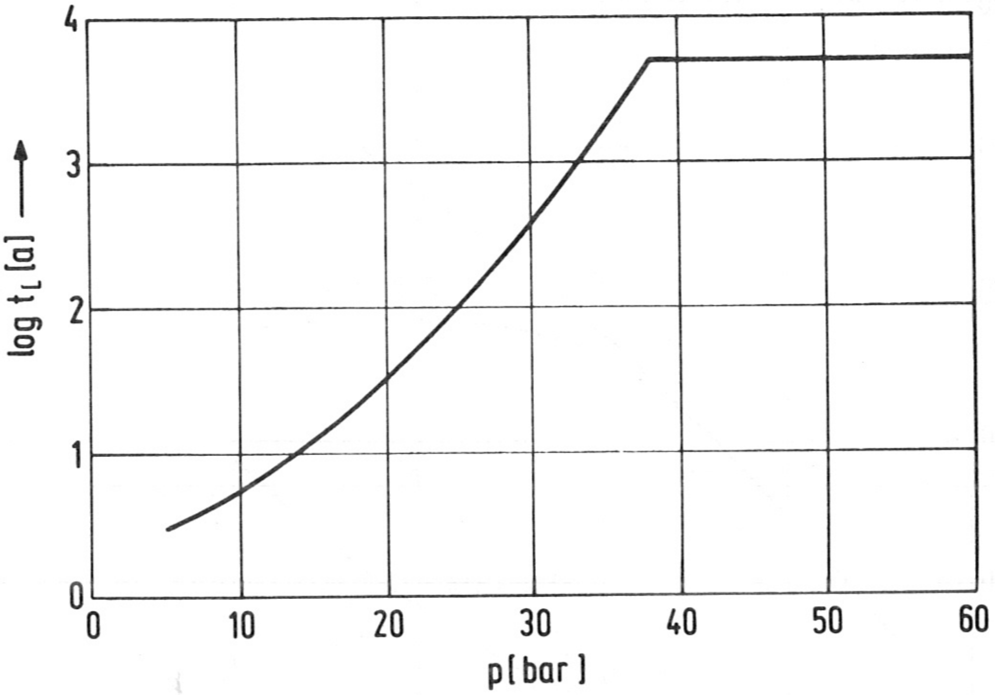

Fig. 35 Calculated fatigue life t_L [a] as a function of the internal pressure p.

6.7. The influence of wall thickness

Varying the wall thickness d in the course of parameter studies causes changes in a number of basic quantities entering the stress and strain evaluations. The combined effects of the different mechanisms for which these quantities are responsible lead to rather complicated dependences of the final results which need more extensive explanation than required for the studies previously reported.

Figure 36 shows the maximum and minimum temperature differences across the wall and the amplitude of the temperature fluctuations at the hot surface as dependent on the wall thickness d.

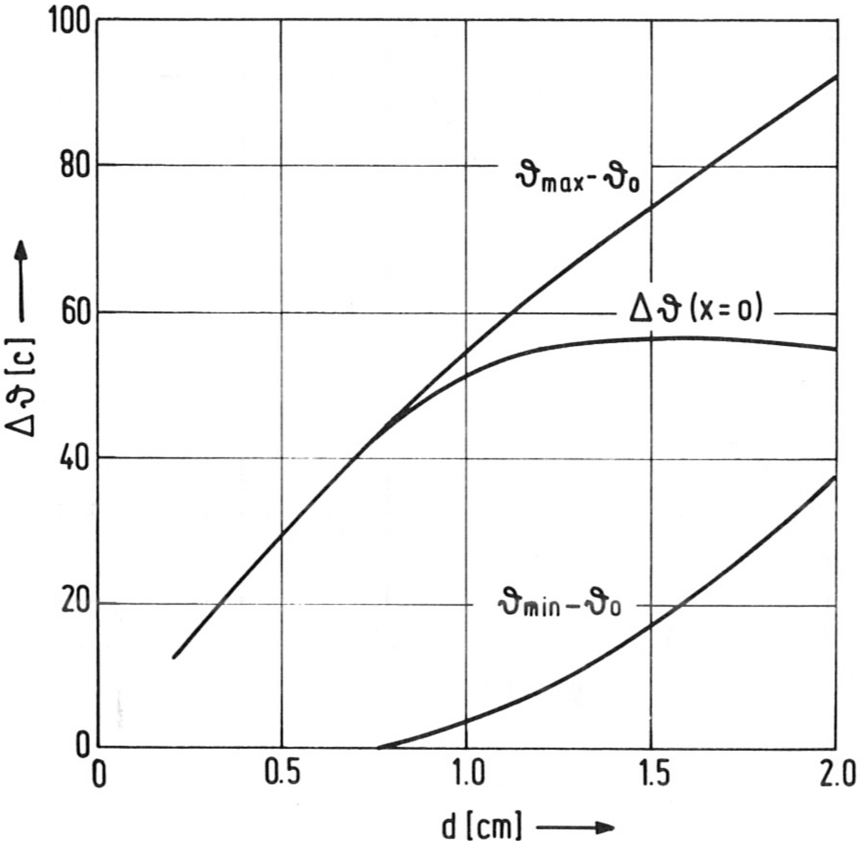

Fig. 36 Maximum and minimum temperature difference across the wall and amplitude $\Delta\vartheta$ of the plasma side wall temperature as functions of the wall thickness d.

As was to be expected, the maximum temperature difference $\vartheta_{max} - \vartheta_o$ which builds up during the burn phase increases nearly linearly with d. At larger values of d, however, a clear deviation from linearity can be detected. This deviation is the combined result of three effects. The first reason is the increase of the time constant τ_d with increasing wall thickness, which prevents the temperature profile from attaining the asymptotic shape defined by the equivalent steady-state temperature profile. The second reason is the slightly decreasing space-averaged nuclear power density in the wall with increasing wall thickness, which is a consequence of the continuous neutron flux attenuation in the wall. The third reason is the temperature dependence of the thermal conductivity of the wall material, which works in the same direction. It seems probable that the first of these effects is the most significant one. The time constant τ_d is also responsible for the behaviour of the minimum temperature difference $\vartheta_{min} - \vartheta_o$. The shorter the time constant the larger is the temperature drop during the down phase. At small wall thicknesses τ_d is so small that the temperature is able to decrease just to the minimum value ϑ_o. Not before τ_d reaches about one-fifth to one-fourth of the down time $\Delta\tau$ can an increase of the minimum temperature above ϑ_o be observed. As a consequence of these two effects, the amplitude of the temperature fluctuations $\Delta\vartheta$ shows the typical behaviour depicted in Fig. 36. After an increase corresponding to that of the maximum temperature difference $\vartheta_{max} - \vartheta_o$ it turns to a nearly constant value at larger wall thicknesses. The slight decrease at the end of the parameter range considered may again be due to the effects of decreasing power density and increasing thermal conductivity.

In Fig. 37 the reference stresses σ_v are plotted as a function of the wall thickness d. In principle, all curves shown exhibit a similar behaviour, reflecting the well-known interaction between mechanical and thermal stresses. With increasing wall thickness the mechanical stresses decrease and the thermal stresses increase with the result that a minimum total stress occurs at an optimum value of d. As can be concluded from this figure, the optima of the maximum reference stresses for the two wall surfaces considered do not, however, coincide. Additionally, the stress variations at both surfaces differ appreciably.

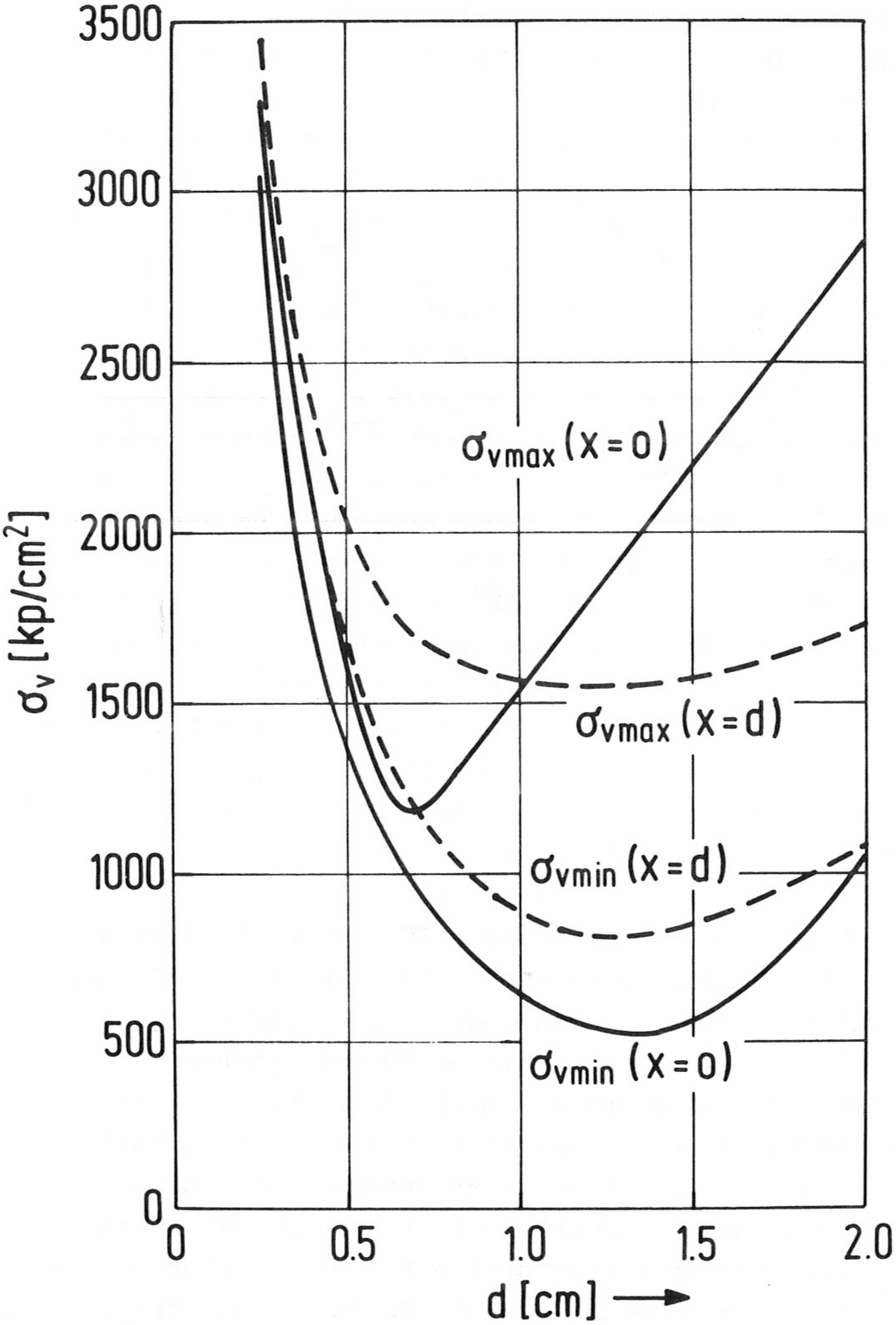

Fig. 37 Maximum and minimum reference stress σ_v at the hot (x=0) and cold (x=d) surface of the wall as a function of the wall thickness d.

As a consequence, the reference strain variations shown in Fig. 38 together with the thermal strain variations also exhibit remarkable differences. It is especially worthwile to note that there may be a range of wall thicknesses in

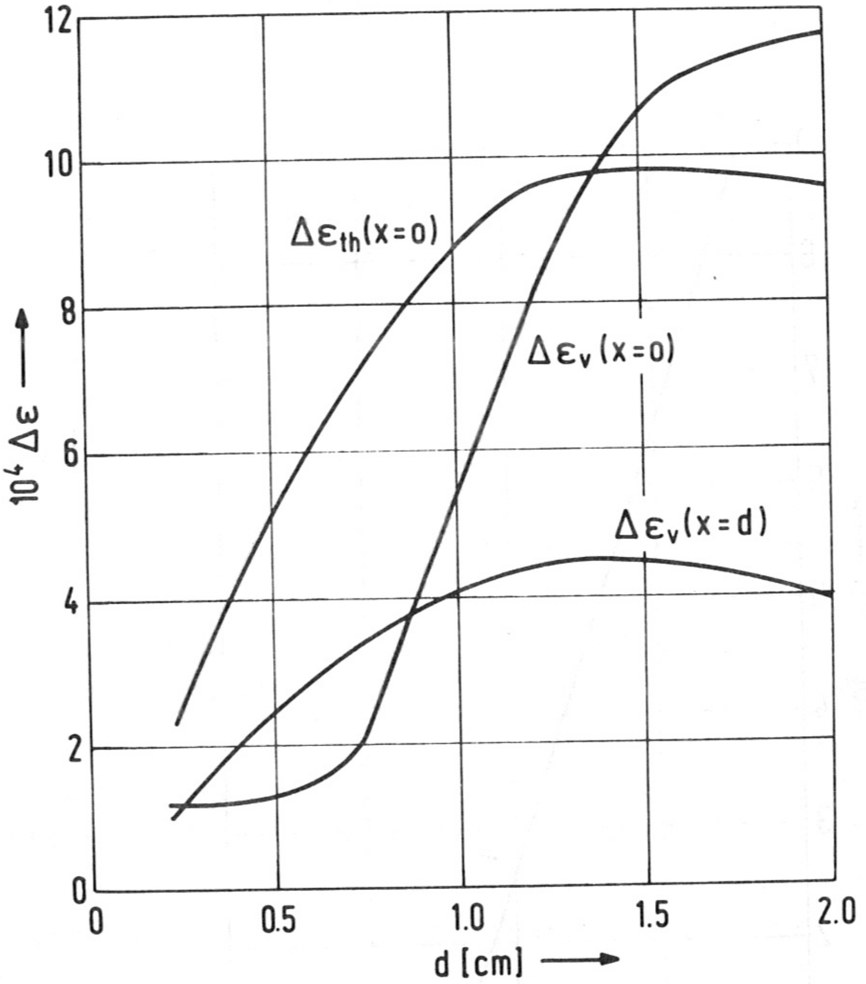

Fig. 38 Thermal strain variations $\Delta\varepsilon_{th}$ at the hot surface and reference strain variations $\Delta\varepsilon_v$ at the hot (x=0) and cold (x=d) surface of the wall as functions of the wall thickness d.

which the reference strain variations at the cold surface exceed those at the hot surface. There is another range in which the reference strain variations exceed even those of the thermal strain. Effects of such a nature cannot, in general, be predicted if too simple methods are applied for the stress-strain analysis.

Quoting the maximum reference strain variations against the fatigue property, values for the useful life yield the results shown in Fig. 39. It is interesting to note that in the range

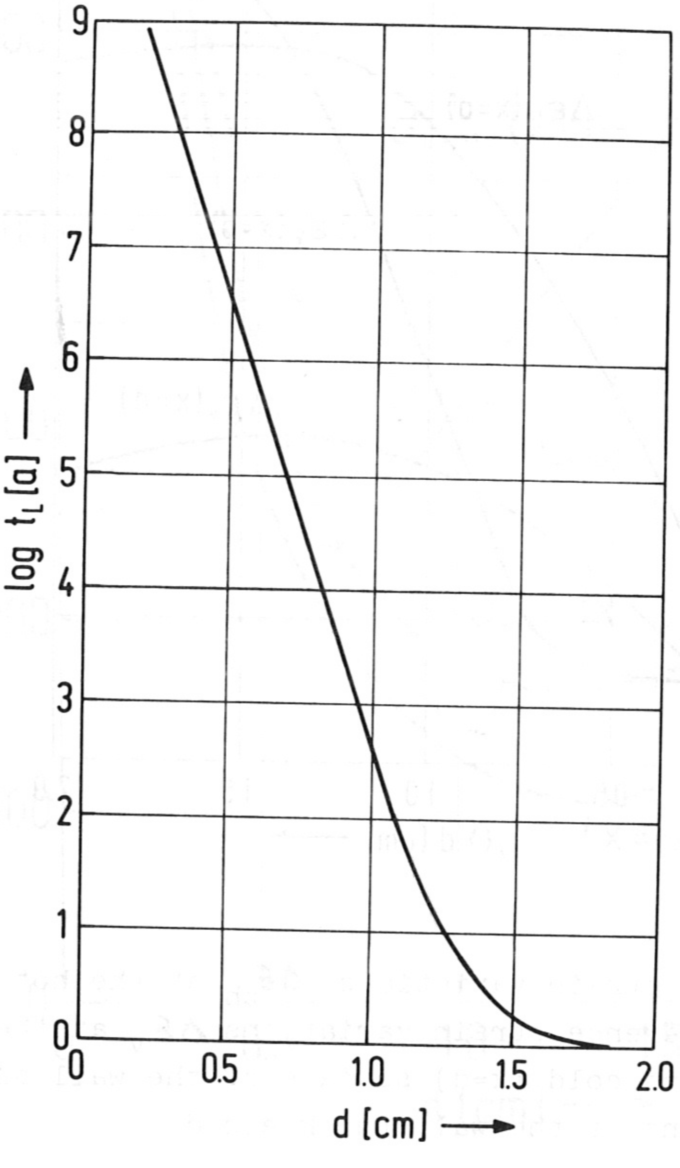

Fig. 39 Calculated fatigue life t_L [a] as a function of the wall thickness d.

of the wall thicknesses considered the useful life may vary by a couple of orders of magnitude, while the strain variations cover only about a single decade. For completeness, it must be repeated at this point that again a temperature dependence of the fatigue life properties has not been taken into account. Therefore, the same caution has to be exercised in interpreting the results of Fig. 39. Since the fatigue life has to be expected to decrease with increasing temperature and hence with increasing wall thickness, the real fatigue life variation with d should result in a curve either below that plotted in Fig. 39 and/or having a steeper slope.

6.8. The influence of wall loading

Regardless of our having used the modified pulse shapes at some few points of this study, we have preserved up to now the consistency between the plasma model, the nuclear response of the wall, and the stress-strain-analysis. In this Section we now break this premise at one point in that we vary the wall loading. We assume that there are combinations of plasma parameters which yield a different average power level but still preserve the same pulse shapes and burn times as specified for the reference case. Practically, we do this by changing the conversion factors FQT and FPT (see Section 4.1.) by the same factor. While in the reference case we have been concerned with a neutron wall loading of about 0.23 MW/m^2 and a total (including radiation) of about 0.27 MW/m^2, both averaged over a cycle duration of 84 seconds, we now intend to investigate a range which is equivalent to neutron wall loadings P_{Wn} between 0.1 and 1.0 MW/m^2. The results are presented in Figs. 40 to 43.

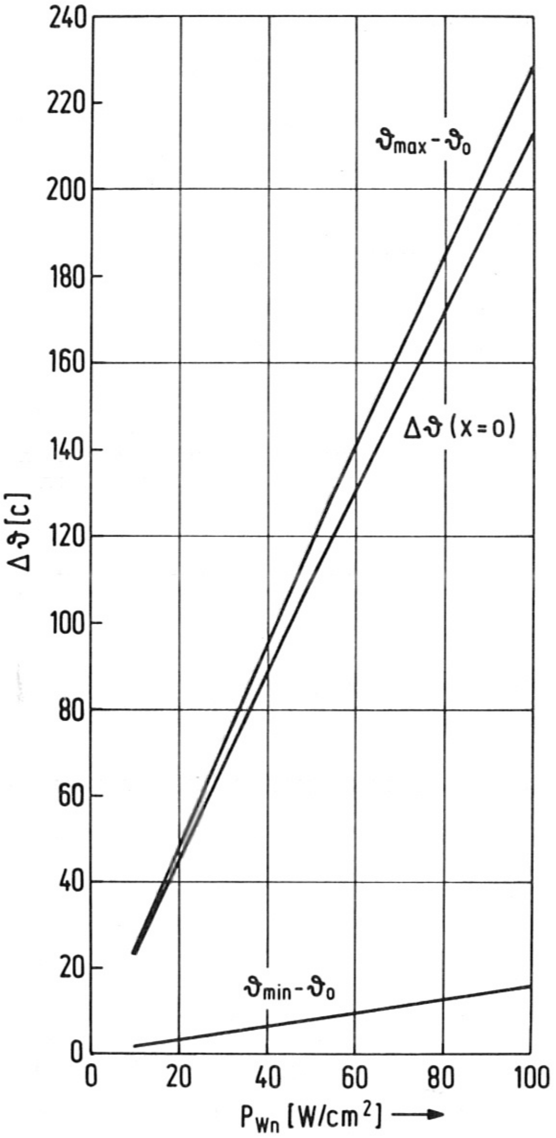

Fig. 40 Maximum and minimum temperature difference across the wall and amplitude $\Delta\hat{\vartheta}$ of the plasma side wall temperature as functions of the average neutron wall loading P_{Wn}.

The results shown do not need much interpretation. All quantities of interest, i.e. temperature differences and amplitudes (Fig.40), reference stresses (Fig. 41), and strain variations (Fig. 42)

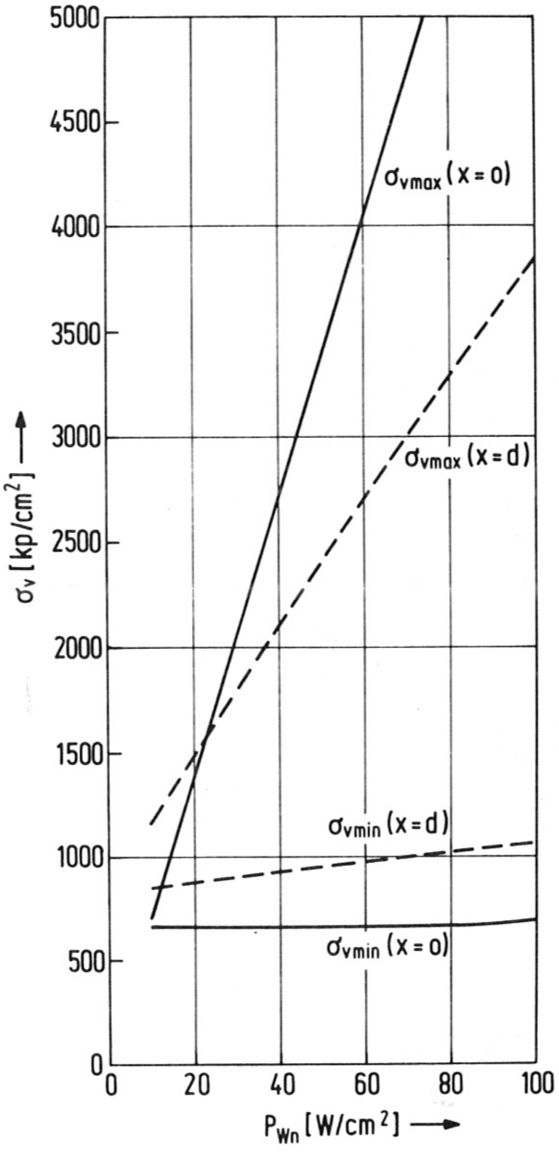

Fig. 41 Maximum and minimum reference stress σ_v at the hot (x=0) and cold (x=d) surface of the wall as functions of the average neutron wall loading P_{Wn}.

are subjected to a continuous increase with the wall loading. Except for very low values of P_{Wn} the reference strain variations at the hot surface $\Delta\varepsilon_v$(x=0) are those which limit the useful life. The fatigue life itself is presented in Fig. 43. As was the case for variations of the wall thickness d,

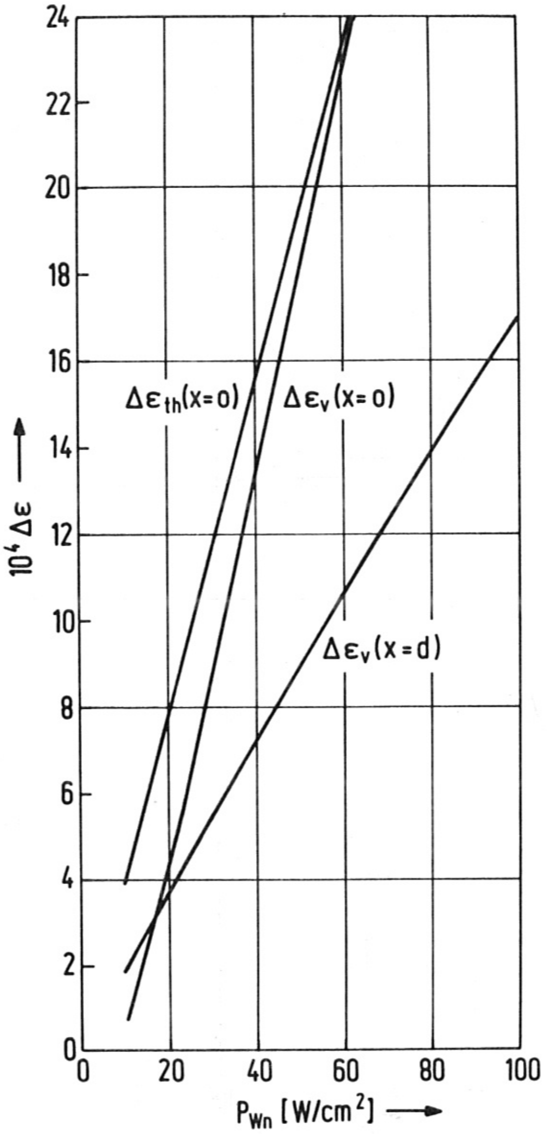

Fig. 42 Thermal strain variations $\Delta\varepsilon_{th}$ at the hot surface and reference strain variations $\Delta\varepsilon_v$ at the hot (x=0) and cold (x=d) surface of the wall as functions of the average neutron wall loading P_{Wn}.

the useful life here also covers a range of a couple of orders of magnitude down to lifetimes below 1 year above wall loadings of about 0.4 MW/m^2.

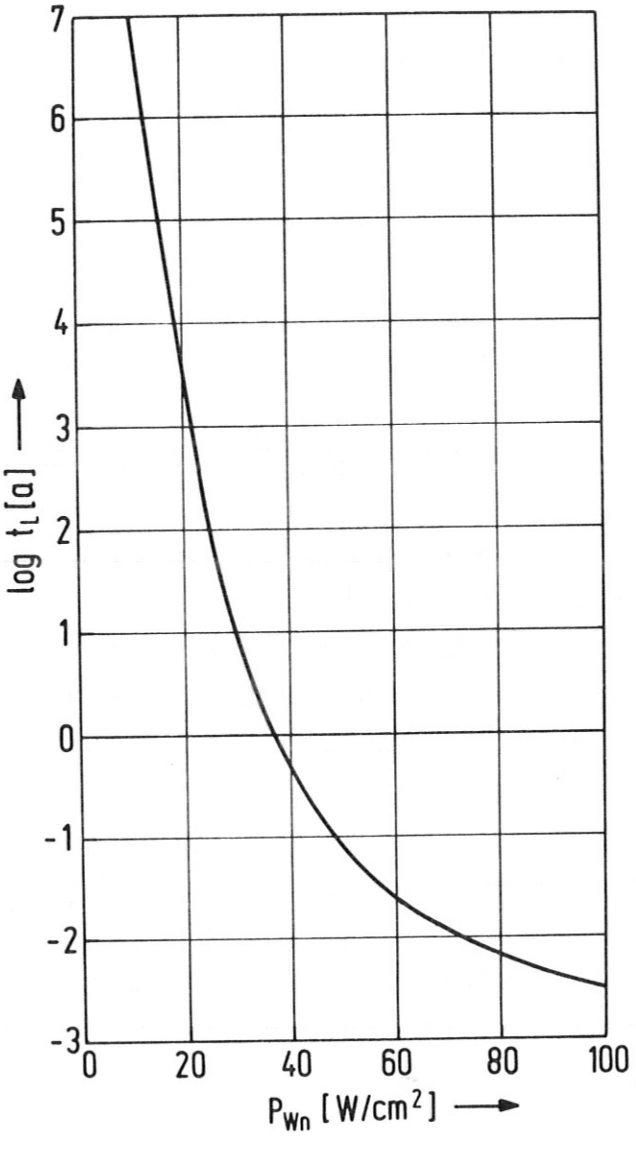

Fig. 43 Calculated fatigue life t_L [a] as a function of the average neutron wall loading P_{Wn}.

As was the case in the preceding section, again the actually existing temperature dependence of the fatigue life has not been taken into account. For this reason the same reservations have to be observed as outlined in Section 6.7.

6.9. The combined influence of wall thickness and wall loading

Based on the outcome of the previous parameter studies, a hierarchy can be established indicating the weight of influence of the single parameters upon the fatigue life. Having covered parameter ranges which seem reasonable from the present-day point of view, we can state that the influence of the down time between successive burn pulses is of minor importance. A similar tendency is expected for the influence of the temperature level although an increase in fatigue life with increasing temperature was calculated. Since, however, only the temperature dependence of the strain variations, and not that of the fatigue life properties, was taken into account, our results convey the mistaken impression of a tendency which actually does not exist, at least not to the extent resulting from the calculations. A significant influence upon the fatigue life follows from variations in the coolant pressure and in the gross geometry of the modules represented here by the outer radius of the cylinder.

By far the largest influences, however, have to be expected from the wall thickness and the wall loading. For this reason a further series of calculations was performed, from which the combined influence of the two parameters upon the fatigue life has been extracted.

Avoiding a presentation of all results, we concentrate here on the final results, which are shown in Fig. 44. Lines of equal fatigue life have been plotted in a coordinate system setup by the wall thickness d and the average neutron wall loading P_{Wn}. Although this picture is actually valid only for a down time $\Delta\tau = 30$ seconds, an internal pressure load of p = 30 bar, a cylinder radius of $r_a = 30$ cm, and a temperature of the cold surface of $\vartheta_o = 500$ C, it should be applicable to a wider range of all of these parameters because of the predominant influence of just the parameters varied.

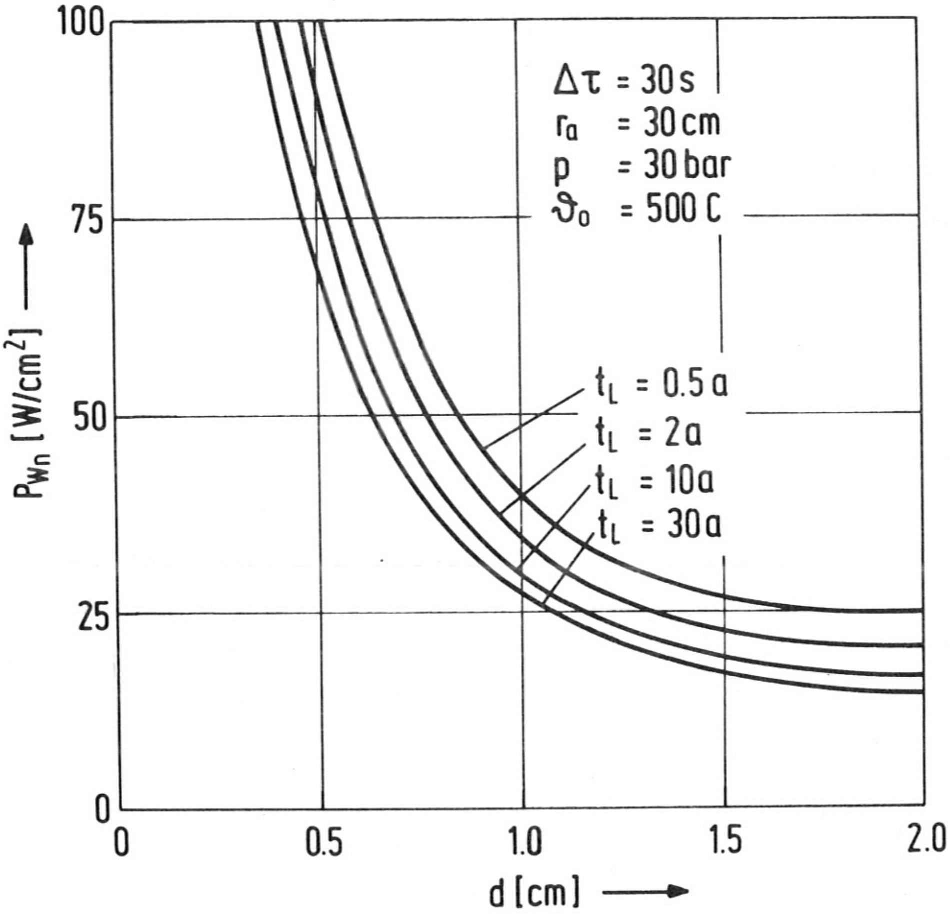

Fig. 44 Lines of constant fatigue life t_L [a] as dependent on wall thickness d and average neutron wall loading P_{Wn}.

As a surprising feature we learn from this picture that the possible parameter combinations of d and P_{Wn} leading to a reasonable, but finite fatigue life are settled within a narrow band. This region extends from low wall loadings of about 0.15 to 0.25 MW/m^2 at 2,0 cm wall thickness to 1 MW/m^2 at a thickness of about 0.35 to 0.55 cm. Wall loadings in the range above 1.0 MW/m^2 as proposed in current design studies for commercial fusion reactors necessitate - from the fatigue life point of view - very thin walls of the order of about 0.3 cm or less. In this range a variation of wall loading can affect the fatigue life rather strongly because of the steep slope of the curves in that range. If for any reasons thicker walls have to be used, the wall loading has to be dropped appreciably. The range of wall loadings envisaged for the experimental power reactors assumed at about 0.2 MW/m^2 offers greater flexibility of design.

7. Conclusions

On the basis of the results of our time dependent plasma simulation code /2/ the analysis of the mechanical performance of the fusion reactor first wall was extended to cover the problems of pulsed load conditions.

The basis of these considerations was the analytical treatment of the nonstationary heat conduction problem, which was solved for a number of different heat load conditions. Of the various solutions elaborated the one selected for further application was that based upon a Fourier solution for arbitrary space functions and periodic time functions of the internal heat sources which are due to nuclear heating. In parallel, a Fourier solution for arbitrary but periodic time functions of an external heat flux density was elaborated which represents the thermal load of the wall due to plasma radiation and heat conduction. Both solutions can be linearly superimposed to obtain the space and time dependent temperature response of the wall to any periodic plasma pulse sequence. The subsequent stress and strain analysis is performed in a quasi steady-state mode using the methods already described in the first part of this report.

Although the nonstationary analysis of the heat conduction problem was only performed for plane geometry, the results are also representative of cylindrical and spherical geometries as long as we think about realistic engineering designs of the blanket and first wall. A further simplification is the neglecting of the temperature dependence of some physical properties which determine the time constant of the wall. The error induced by this assumption is small compared with other errors, e.g. those occurring in the course of the numerical calculations.

A major source of error is introduced in the last step of the present analysis in which the resulting strain variations are quoted against the fatigue life properties of certain materials to achieve information about the useful life. Few data have been published about this material property. Hence we have been forced to apply a design curve which actually does not meet the requirements adequate to the depth of the analysis. It should, however, be no problem to switch to a more refined version of data representation if it becomes available.

To arrive at an operable state, the results of the analysis were programmed for the computer using essentially the already existing code and extending it to cover both the steady-state and the nonstationary case. Checking the program against the steady state and an analytical result revealed no significant and inexplicable differences. Thus we are convinced that a reliable instrument for parameter studies has been provided.

A number of parameter studies has been performed the results of which have been presented in this report. Starting from a reference case, we have varied the most essential independent parameters using a realistic plasma burn pulse. The purpose of these studies was to look for the trends in the final results which determine the fatigue life of the wall and to obtain some estimates about the fatigue life itself. The latter results have to be regarded with caution, however, for the reasons outlined above and mentioned at various places throughout this report.

In spite of these inaccuracies, which are unavoidable in the present state of knowledge about fatigue life properties, we have detected some basic tendencies which allow some insight into the weight by which the fatigue life is affected owing to the variation of some parameters. Minor significance should be attributed to the choice of down times between the burn pulses and to the temperature level at which the strain variations occur. A remarkable influence was found if mechanical stresses in the wall are changed either by variation of the pressure load or by that of the wall radius. The biggest, almost dramatic, influence has to be expected from variations of the wall thickness and for the wall loading. Looking at the combined effects of the two parameters shows that safe operation of the first wall may be assured at wall loadings below 0.15 MW/m^2 or at wall thicknesses below 0.3 cm. In the range above these values careful calculations are needed to arrive at a satisfactory engineering design of the first wall with respect to fatigue life.

Acknowledgements

The authors gratefully acknowledge the assistence of K. Borraß, who provided the necessary information on the plasma physics side. They are highly indebted to H. Gorenflo, whose programming experience made the program a flexible instrument, and who performed the many calculations necessary for concluding this study. They finally thank A. Nicol for reading the manuscript, Mrs. E. Kraus for typing it and Miss J. Pfister for the excellent preparation of the pictures.

References

/1/ W. Dänner: "The mechanical performance of the fusion reactor first wall. Part I: steady state analysis without irradiation effects", IPP 4/143 (1976)

/2/ K. Borraß: $q_t(t)$ aus plasmamodell S. 9
plasmamodel

/3/ H.S. Carslaw, J.C. Jaeger: "The conduction of heat in solids", Oxford at the Clarendon Press, second edition, 1959, p. 50

/4/ see /3/, p. 113

/5/ R.C.F. Bartels, R.V. Churchill: "Resolution of boundary problems by the use of a generalized convolution", Bull.Am.Math.Soc., 48, 276 (1942)

/6/ see /3/, p. 32

/7/ K. Ehrlich: private communication

/8/ C.A. Hampel (ed.): Rare metals handbook. Reinhold Publ. Corp., London, 1961

/9/ C.J. Smithells: Metals reference book, Vol. III. Butterworths, London, 1967

/10/ K.D. Cloß: Physikalische und mechanische Eigenschaften von Hüllmaterialien. PSB-Bericht Nr. 1001 (Phase IIa). KFZ Karlsruhe, 1968

/11/ taken from:
Argonne National Laboratory (ed.): Tokamak Experimental Power Reactor Conceptual Design (Vol. I)., Report ANL/CTR-76-3 (1976)

/12/ W. Dänner: Some nuclear characteristics of liquid lithium / stainless steel fusion reactor blankets (to be published).

/13/ R.T. Perry, H. Gorenflo, W. Dänner: INDRA: a program system for calculating the neutronics and photonics characteristics of a fusion reactor blanket. Report IPP 4/137 (1976)

/14/ H. Neuber: Technische Mechanik. 2. Teil: Elastostatik und Festigkeitslehre. Springer-Verlag Berlin, Heidelberg, New York (1971).